

論文 / 著書情報
Article / Book Information

題目(和文)	
Title(English)	A Study on Reliability and Scalability of Ferroelectric AlScN Films
著者(和文)	TSAI Sung-Lin
Author(English)	Sung-Lin Tsai
出典(和文)	学位:博士(工学), 学位授与機関:東京工業大学, 報告番号:甲第12383号, 授与年月日:2023年3月26日, 学位の種別:課程博士, 審査員:角嶋 邦之,筒井 一生,若林 整,渡辺 正裕,飯野 裕明,右田 真司
Citation(English)	Degree:Doctor (Engineering), Conferring organization: Tokyo Institute of Technology, Report number:甲第12383号, Conferred date:2023/3/26, Degree Type:Course doctor, Examiner:,,,,,
学位種別(和文)	博士論文
Type(English)	Doctoral Thesis

Doctoral Thesis

**A Study on Reliability and Scalability of
Ferroelectric AlScN Films**

A Dissertation Submitted to the Department of Electrical and
Electronic Engineering
School of Engineering, Tokyo Institute of Technology

January 2023

Sung Lin TSAI

Supervisor:

Associate Prof. Kuniyuki Kakushima

Abstract

Non-volatile memory has been an important part of internet-of-things (IoT) devices. Among the non-volatile memories, ferroelectric non-volatile memories are expected to show low power consumption owing to their electric field operation. Ferroelectric random-access-memory (FeRAM) with perovskite materials has been commercialized in the past. However, it has reached its limit in thickness scaling at a relatively thick region of 100 nm. Therefore, new materials have been required to overcome the thickness scaling, enabling high-density FeRAM. A new nitride-based ferroelectric material, $\text{Al}_{1-x}\text{Sc}_x\text{N}$, has been reported in 2019 with its high remanent polarization. Also, a recent study shows that $\text{Al}_{1-x}\text{Sc}_x\text{N}$ films exhibit ferroelectricity with a thickness down to 9 nm. As $\text{Al}_{1-x}\text{Sc}_x\text{N}$ films are quite new, there is no study detailed study to be used for memory applications; including reliability, switching cycle endurance, breakdown, and also change in the property by thickness scaling.

The purpose of the thesis is to understand the degradation and breakdown mechanism of AlScN films. And to propose a process for high-reliable films with thickness scaling capability.

The process used in this study is reactive sputtering with an AlSc alloy target. A gas mixture of Ar, N_2 , and/or O_2 was used to deposit the films. The wurtzite structure of AlScN has been confirmed with the grain size of $50\text{ nm}\times 20\text{ nm}$. Low-temperature deposited 50-nm-thick AlScN MIM capacitors also showed ferroelectricity with a remanent polarization of $80\text{ }\mu\text{C}/\text{cm}^2$ and a coercive field of $5.8\text{ MV}/\text{cm}$ on a CMOS-compatible metal electrode. The *CV* measurements also show poling-free behavior for AlScN MIM capacitors whose surface of AlScN films is N-face.

Reliability and breakdown mechanism evaluated by leakage current analysis upon different switching cycling. Continuous effective Schottky barrier height at AlScN/metal interface was extracted, and the local conduction path was hardly formed. The degradation is different from oxide-based ferroelectric films, where oxygen defect-mediated local conduction takes place. Moreover, AlScN films break down by Joule heat once the leakage current exceeds a certain level due to a reduction in the barrier height. The extracted model suggests the need for treatments at AlScN/metal interface.

Thickness scaling for AlScN films has revealed less oriented growth and elongation in the c-axis lattice. Remanent polarization was found to be reduced under switching at a constant electric field. This fact suggests the increase in the coercive field due to the strain in the AlScN film near the AlScN/metal interface.

Oxygen atoms incorporation to form AlScON films was found to be effective in reducing the coercive field. As the excess incorporation leads to the formation of AlScO₃ in the film, the content of oxygen atoms should be optimized. Under composition of Al_{0.7}Sc_{0.3}O_{0.2}N_{0.8}, the coercive field was reduced from 3.8 to 2.8 MV/cm. However, the increase in the coercive field upon thickness scaling is still observed. This fact indicates that stress cannot be relaxed by oxygen incorporation.

A concept of stacking of AlScON/AlScN is evaluated for the purpose to suppress the leakage current keeping the low coercive field. From different stacking sequences, it was found that the coercive field is determined by the bulk layer; the AlScON layer. With a stacked structure, ferroelectricity showed with a 6.7-nm-thick device under 5 V operation, which is promising for memory applications. Switching cycle endurance was slightly improved with the Al_{0.7}Sc_{0.3}N barrier layer, owing to the rigid interface with the low coercive field of the bulk Al_{0.7}Sc_{0.3}O_{0.2}N_{0.8} layer.

In conclusion, ferroelectricity was confirmed with the low-temperature process (RT), which means it is suitable for resin substrates for future memory applications. The wake-up effect is modeled by V_N formation to lower the E_c , and fatigue is explained by electron trapping. The breakdown is triggered by the excess reduction in effective Schottky barrier height at AlScN/metal interface. Strain near the bottom electrode increases the E_c , leading to a reduction in P_r under constant E-field operation. AlScON with optimum O atoms can reduce the E_c , at the cost of leakage current. $Al_{0.7}Sc_{0.3}O_{0.2}N_{0.8}$ on an $Al_{0.7}Sc_{0.3}N$ barrier layer enables the thickness scaling down to 12 nm, with <5 V operation. More research is needed for the barrier layer for thickness scaling.

Contents

Chapter 1.....	1
Introduction.....	1
1.1 Nowadays Memories	2
1.2 Ferroelectric PbZrTiO_x (PZT) films	4
1.3 Ferroelectric HfO₂ (Hf_{0.5}Zr_{0.5}O₂) films	4
1.4 Ferroelectric HfO₂ films for NVM devices	6
1.5 Reports of ferroelectric AlScN film	9
1.6 Ferroelectric AlScN films for NVM devices	16
1.7 Conclusion	18
1.8 Purpose of this thesis	19
1.9 Outline of this thesis	19
Reference	20
Chapter 2.....	25
Experimental Methods.....	25
2.1 Physical Characteristics of AlScN film	26
2.1.1 XRD (X-ray Diffractometer)	26
2.1.2 XRC (X-ray rocking curve)	27
2.1.3 XPS (X-ray Photoelectron Spectroscopy)	27
2.1.4 TEM (Transmission Electron Microscope)	28
2.2 Electrical Characteristics of AlScN film	28
2.2.1 JV measurement	28
2.2.2 CV measurement	29
2.2.3 PUND measurement	30
2.2.4 Fatigue measurement	31
References	31
Chapter 3.....	33
Low-temperature formation of ferroelectric AlScN films.....	33
3.1 Room-Temperature Deposited Ferroelectricity AlScN Film	34
3.2 Fabrication process of AlScN Capacitors with Different Deposition Temperature	35
3.3 Experiment results of AlScN Capacitors with Different Deposition Temperature	37
3.4 Summary of this chapter	47
References	48
ACKNOWLEDGMENTS	50
Chapter 4.....	51

4.1 The Breakdown Mechanism of AlScN Film after Cycling Test	52
4.2 Fabrication process of 400°C deposited AlScN Capacitors	54
4.3 Interface analysis method by analyzing leakage current	54
4.4 Experiment results of 400°C deposited AlScN Capacitors after cycling tests	56
4.5 Summary of this chapter	65
References	66
Chapter 5	68
Thickness Scaling in Ferroelectric AlScN Films	68
5.1 AlScN capacitors with Thickness Scaling	69
5.2 Fabrication process of AlScN capacitors with thickness Scaling	71
5.3 Experiment results of AlScN capacitors with thickness Scaling	72
5.4 Summary of this chapter	82
References	83
Chapter 6	85
Oxygen atoms incorporation for thickness scaling	85
6.1 Concepts of oxygen atoms incorporation in Al_{1-x}Sc_x(O)N Films	86
6.2 Fabrication process of ferroelectric capacitors	87
6.3 Experiment results of Al_{1-x}Sc_x(O)N Capacitors	88
6.4 Summary of this chapter	101
References	102
Chapter 7	103
AlScON/AlScN stacking for reliable ferroelectric films	103
7.1 Concepts of AlScON/AlScN stacking	104
7.2 Experiment results of AlScON/AlScN stacking Capacitors	106
7.3 Summary of this chapter	111
Chapter 8	112
Conclusions	112
List of Publications	115
List of Conferences	117
List of Award	119
Acknowledgements	120

Chapter 1

Introduction

1.1 Nowadays Memories

Nowadays higher volume memories with lower energy consumption memories are needed. DRAM has reached its limit in thickness due to its small signal. Besides, DRAM needs to refresh to keep the memories which lead to high energy consumption. Figure 1.1 showed the change of memories in progress [1.1]. NVM memories have been applied to IoT devices.

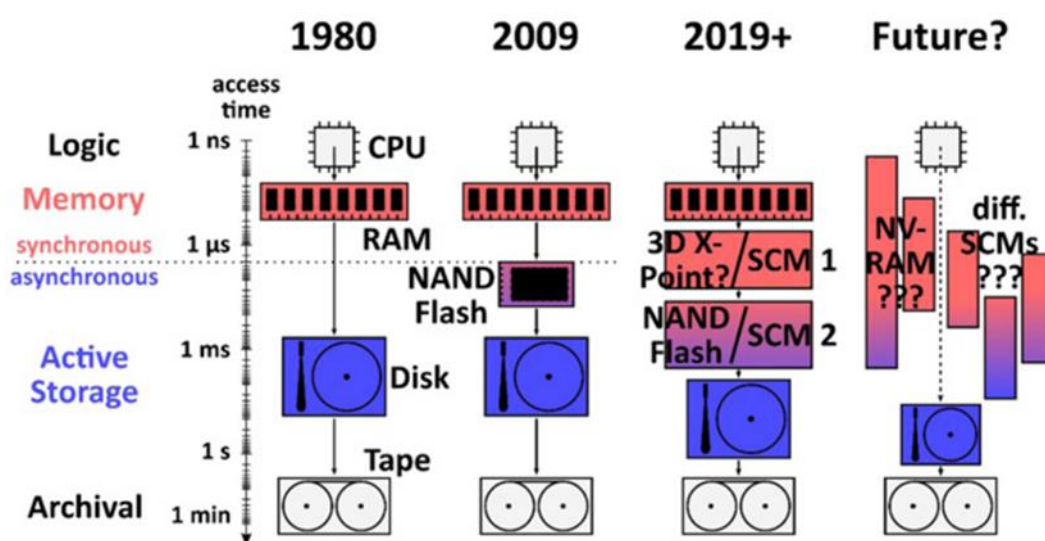


Figure 1.1 Changes of memories in progress [1.1].

Among the NVM, Ferroelectric NVM showed low power consumption with its electric field operation, which raises researchers' attention. Table 1.1 showed the comparison between non-volatile memories and DRAM [1.1]. Non-volatile memory FRAM shows low energy consumption.

Table 1.1 Comparison between FRAM and Other Memories [1.1]

Parameter/NVM	MRAM	FeRAM	FcFET	PCM	RRAM	NAND flash	NOR flash	DRAM
R/W speed	<10 ns	10 ns	100 ns	>100 ns	<10 ns	100 μ s	1 μ s to 1 s	~10 ns
Endurance	1×10^{15}	1×10^{15}	1×10^5	$>1 \times 10^8$	1×10^9	1×10^4	1×10^6	1×10^{16}
Retention	10 years	10 years	10 years	10 years	10 years	10 years	10 years	64 ms
Energy	2 pJ bit ⁻¹	50 fJ bit ⁻¹	<1 fJ bit ⁻¹	3 pJ bit ⁻¹	50 pJ bit ⁻¹	1 nJ bit ⁻¹	10 nJ bit ⁻¹	pJ bit ⁻¹
Cell size	$20F^2$	$6F^2$	$6-10F^2$	$5.5F^2$	$4F^2$	$4F^2$	$10F^2$	$6F^2$

Figure 1.2 showed the hysteresis loop and ferroelectric capacitor polarization conditions [1.2]. It shows a simple illustration of how ferroelectric materials store “1” or ”0” data with its polar. It stores the data with their polar so that it doesn’t need to refresh and waste energy.

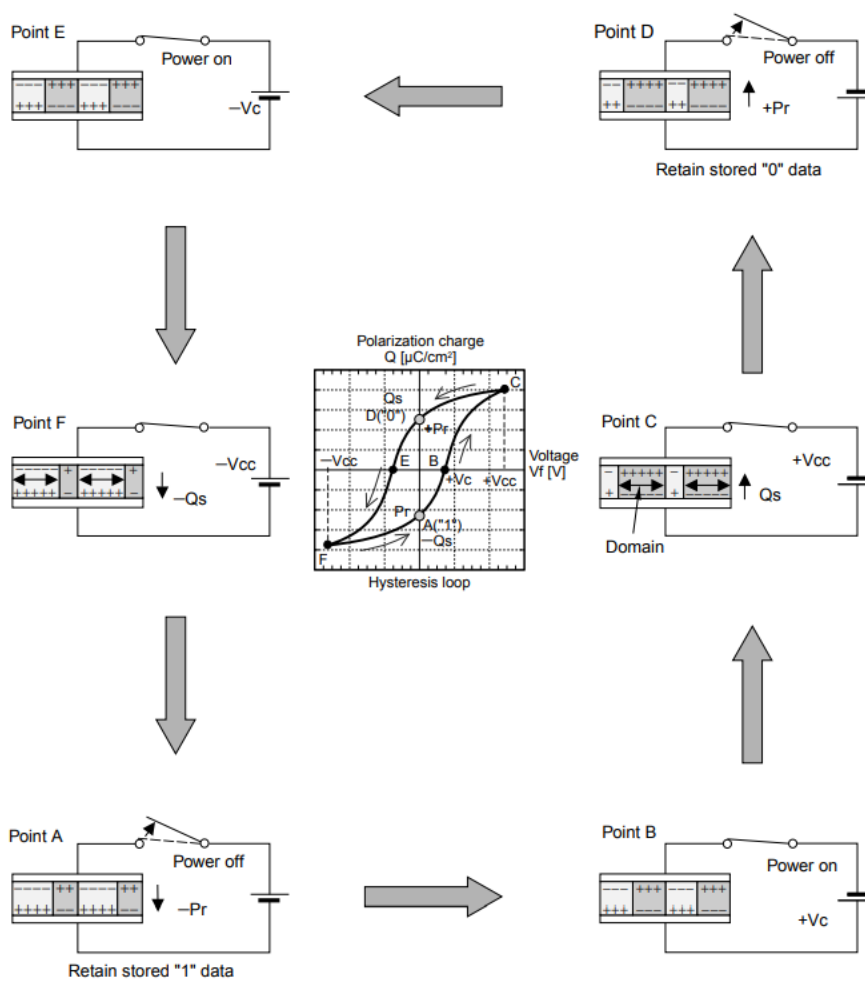


Figure 1.2 Hysteresis loop and ferroelectric capacitor polarization conditions [1.2]

1.2 Ferroelectric PbZrTiO_x (PZT) films

PbZrTiO_x (PZT) have been applied to ferroelectric RAM. Figure 1.3 showed schematics of the state-of-the-art perovskites-based FeRAM [1.3].

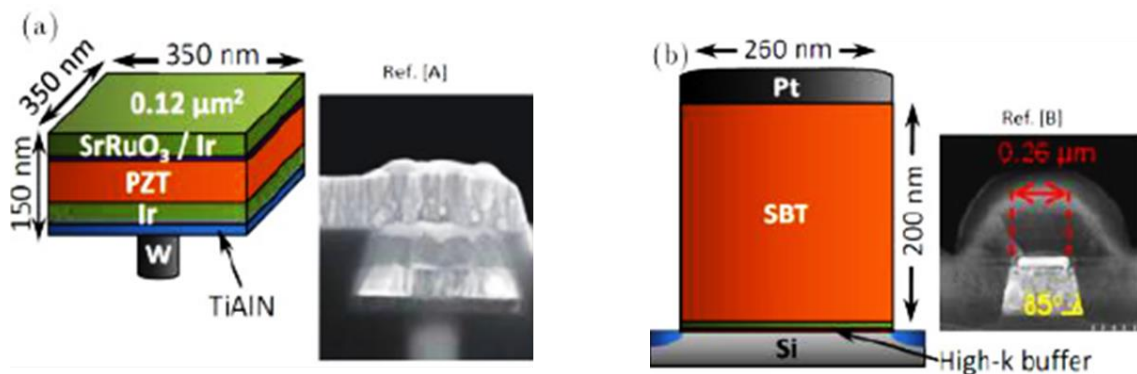


Figure 1.3 Schematics of the state-of-the-art perovskites-based FeRAM [1.3].

However, there is a thickness limit of 100nm for the PZT layer. If the PZT layer is thinner than 100nm, the film will lose ferroelectricity. So, a new ferroelectric material is needed for high-density RAM. There are four properties that new ferroelectric material required. 1. a thickness scaling about below 10nm. 2. high remanent polarization. 3. low operation voltage and 4. long endurance for memory.

1.3 Ferroelectric HfO₂ (Hf_{0.5}Zr_{0.5}O₂) films

In 2011, a new ferroelectric material, HfO₂ was reported. HfO₂ showed its advantage of compatibility with the CMOS process and with low-temperature process. HfO₂ also shows ferroelectricity down to 3nm which is good for scaling down the process of memory application. Figure 1.4 showed the *PE* curves of HfO₂ [1.4]. Figure 1.5 showed

the crystal structure of HfO_2 [1.5] and figure 1.6 showed the thickness scaling of HfO_2 [1.5].

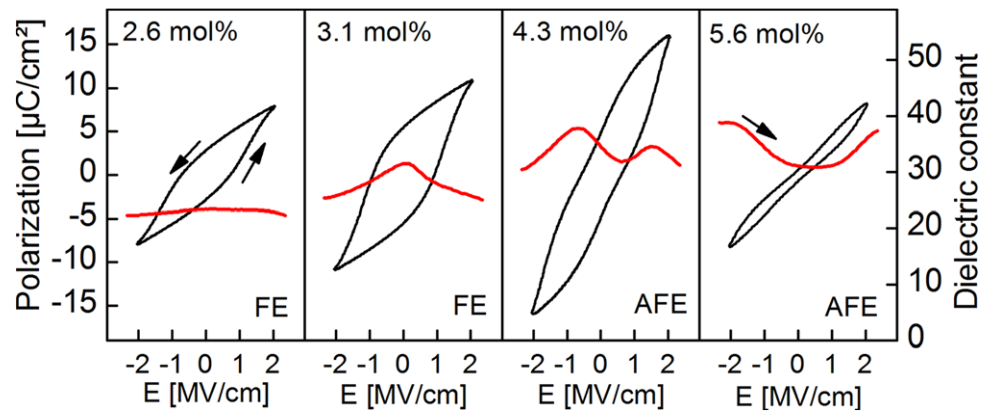


Figure 1.4 Typical PE curves of HfO_2 [1.4].

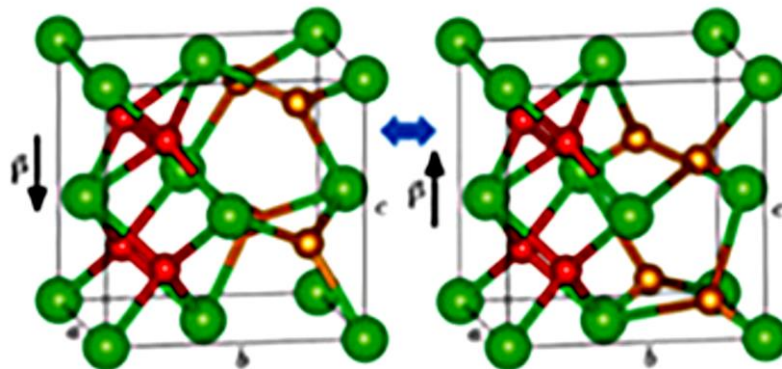


Figure 1.5 Switching of HfO_2 [1.5].

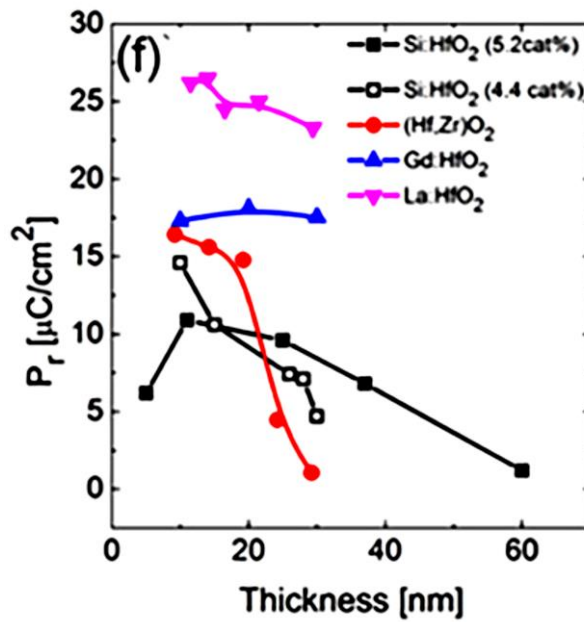


Figure 1.6 Thickness scaling of HfO₂ [1.5].

1.4 Ferroelectric HfO₂ films for NVM devices

There are already a few reports on Ferroelectric NVM devices with HfO₂. Figure 1.7-1.12 showed FeRAM, FeFET, and FTJ with HfO₂ film and its electrical characteristics [1.6-1.8]. Although HfO₂ show great potential for memory applications, HfO₂ has the wake-up effect and degradation issue which brings reliability problems for its unpredicted *P_r*. Figure 1.13 showed the wake-up effect and the degradation issues of HfO₂.

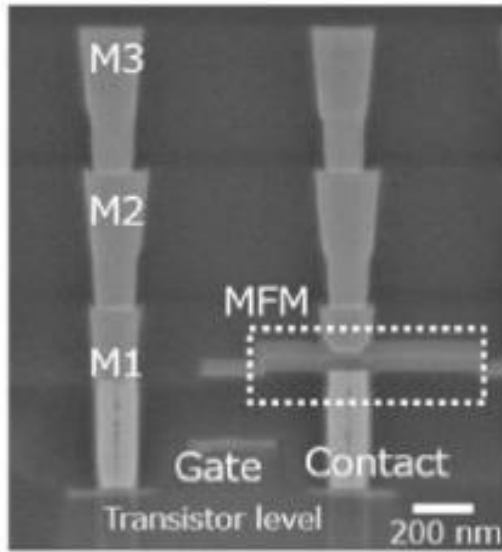


Figure 1.7 Ferroelectric HfO_2 films for FeRAM [1.6].

(b) Experiment

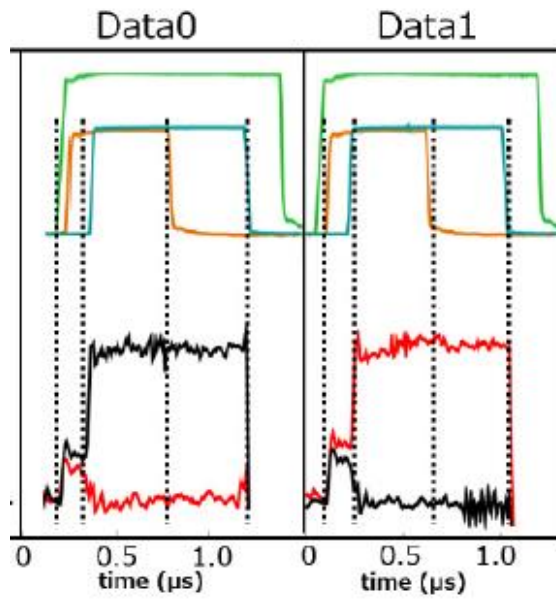


Figure 1.8 Electrical characteristics of ferroelectric HfO_2 FeRAM [1.6].

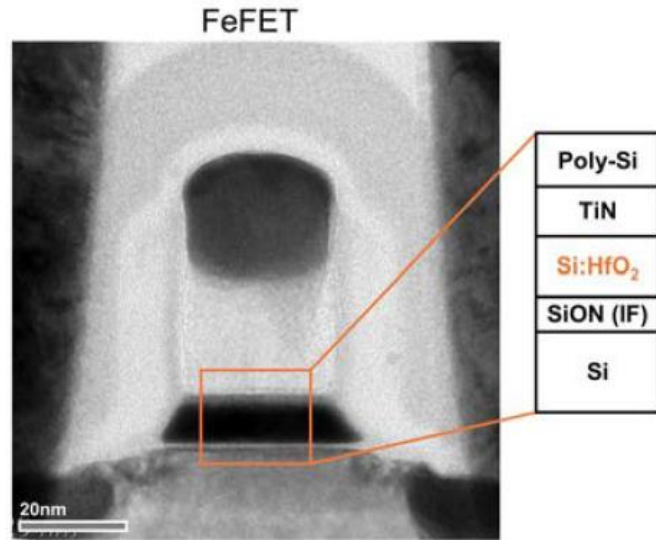


Figure 1.9 Ferroelectric HfO₂ films for FeFET [1.7].

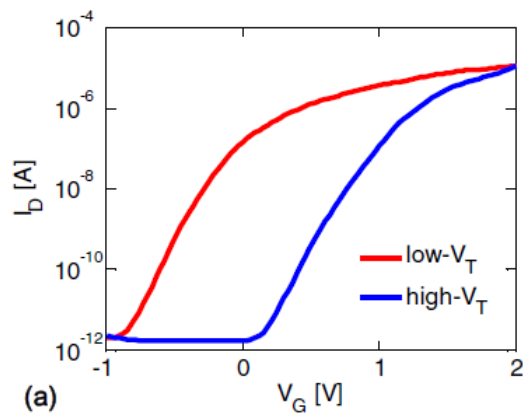


Figure 1.10 Electrical characteristics of ferroelectric HfO₂ FeFET [1.7].

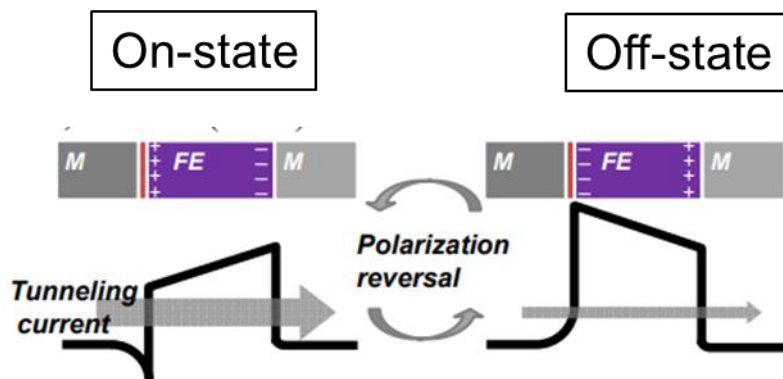


Figure 1.11 Ferroelectric HfO₂ films for FTJ [1.8].

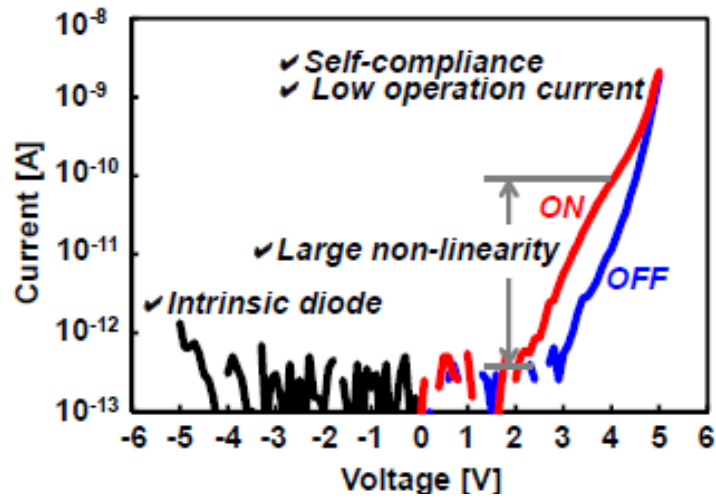


Figure 1.12 Electrical characteristics of ferroelectric HfO₂ FTJ [1.8].

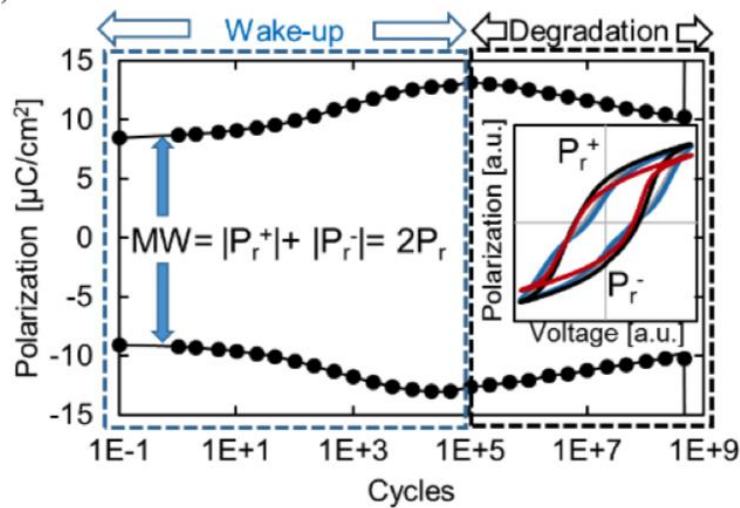


Figure 1.13 Typical endurance characteristics of the FeCap were recorded at 10 kHz read frequency and 100 kHz cycling at 3.3V [1.9].

1.5 Reports of ferroelectric AlScN film

There are several MEMS applications for AlScN layers before. The electrical characteristic of the AlScN layer has been discussed for different compositions of Sc [1.10~1.11]. In 2019, Fichtner's group found the ferroelectric behavior of the AlScN layer

for the first time [1.12]. The discovery of the ferroelectric behavior of the AlScN layer gives researchers new hope in doing new ferroelectric material research. There is a thickness limit of about 100nm for PZT and the content of Pb is bad for humans bodies [1.13~1.16]. Although a new ferroelectric material HfO₂ shows potential due to its thickness scaling to 3nm, it still has lots of issues to be solved [1.17~1.19]. The AlScN layer shows the potential to scale down the thickness due to its large remanent polarization of over 100 $\mu\text{C}/\text{cm}^2$ [1.12]. Figure 1.14 shows the high remanent polarization and box-profile *PE* curves of AlScN films with different compositions of Sc atoms.

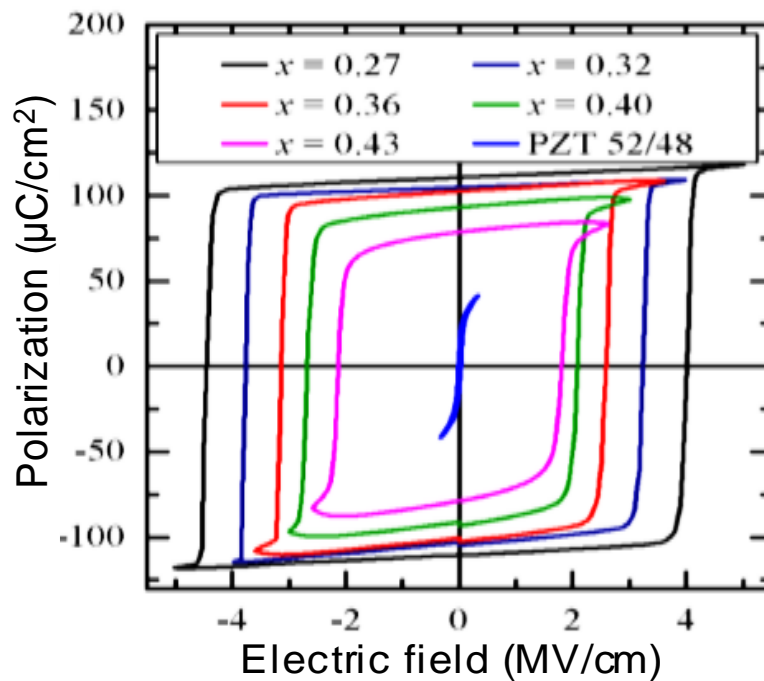


Figure 1.14 High remanent polarization and box-profile PE curves of AlScN films with different compositions of Sc atoms at 711Hz [1.12].

Figure 1.15 showed the different coercive fields of the AlScN layer under different measuring frequencies [1.20]. The reason is that the polar switched from nucleation and

become wider as switching which takes time for this process. The KAI model can explain this process.

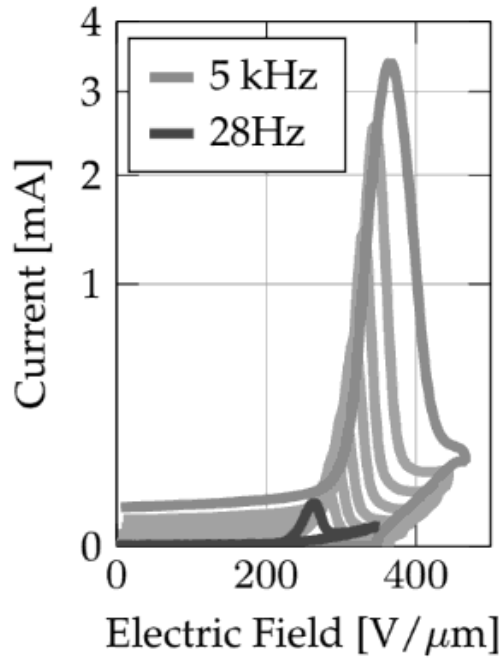


Figure 1.15 The measured current during P-E measurements at logarithmically scaled frequencies from between 28 to 5kHz. [1.20]

Figure 1.16 showed the switching mechanism of AlScN which is the movement of the N atom [1.12]. Figure 1.17 and figure 1.18 showed a variety in ferroelectricity of AlScN by changing the composition of Sc atoms [1.11].

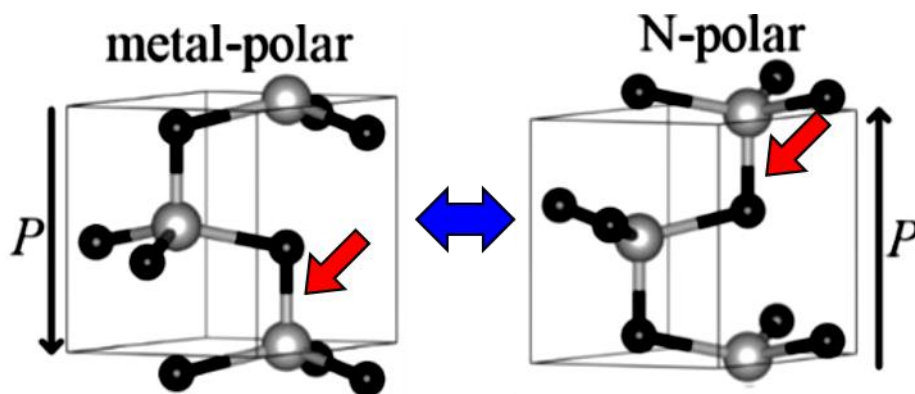


Figure 1.16 Switching mechanism of AlScN. [1.12]

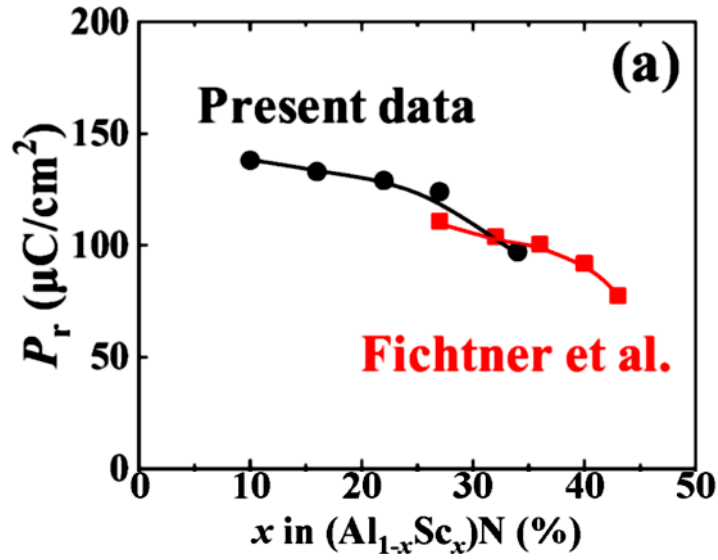


Figure 1.17 A variety in P_r of AlScN by changing the composition of Sc atoms [1.11].

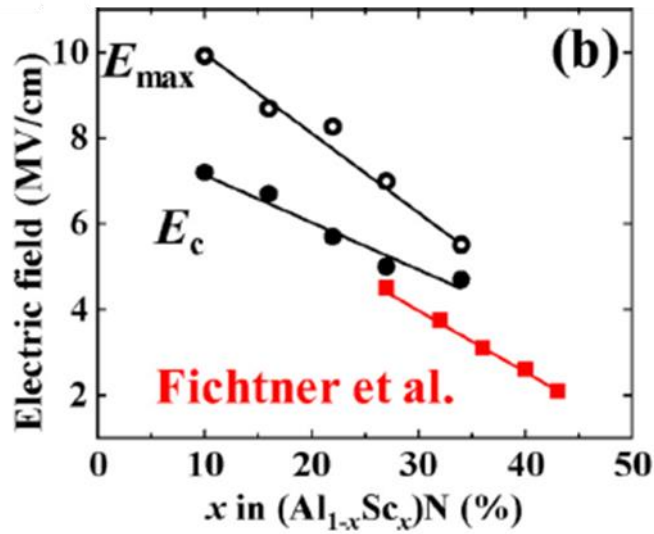


Figure 1.18 A variety in E_c of AlScN by changing the composition of Sc atoms [1.11].

Figure 1.19 shows a variety in the a-axis lattice constant and c-axis lattice constant of AlScN by changing the composition of Sc atoms [1.11]. Figure 1.20 shows the relation between the c/a ratio and E_c . The results show a lower c/a ratio with lower E_c . Figure 1.21 shows an illustration to explain how Sc-N bonding influences the a-axis and c-axis. The

bonding length of Sc-N is longer than Al-N. Thus, Sc atoms in AlScN distort the structure and induce long a-axis and shorter c-axis. Distortion in the wurtzite structure eases the movement of N atoms. Lower E_c with longer a-axis lattice and shorter c-axis lattice. Therefore, higher Sc content shows lower E_c . The ferroelectricity is also confirmed by PFM which showed in figure 1.22 [1.21].

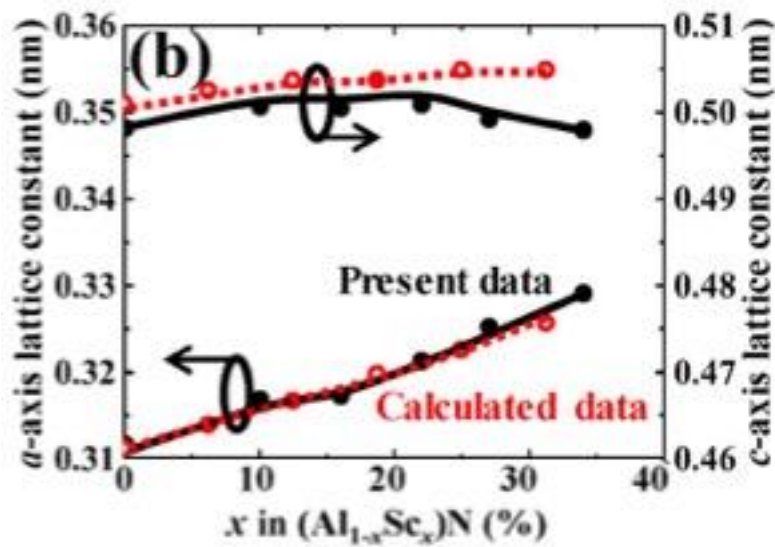


Figure 1.19 A variety in the a-axis lattice constant and the c-axis lattice constant of AlScN by changing the composition of Sc atoms [1.11].

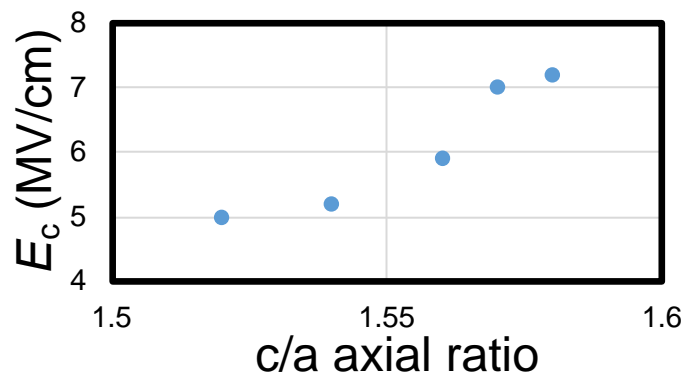


Figure 1.20 Relation between c/a ratio and E_c .

Bonding length Sc-N > Al-N

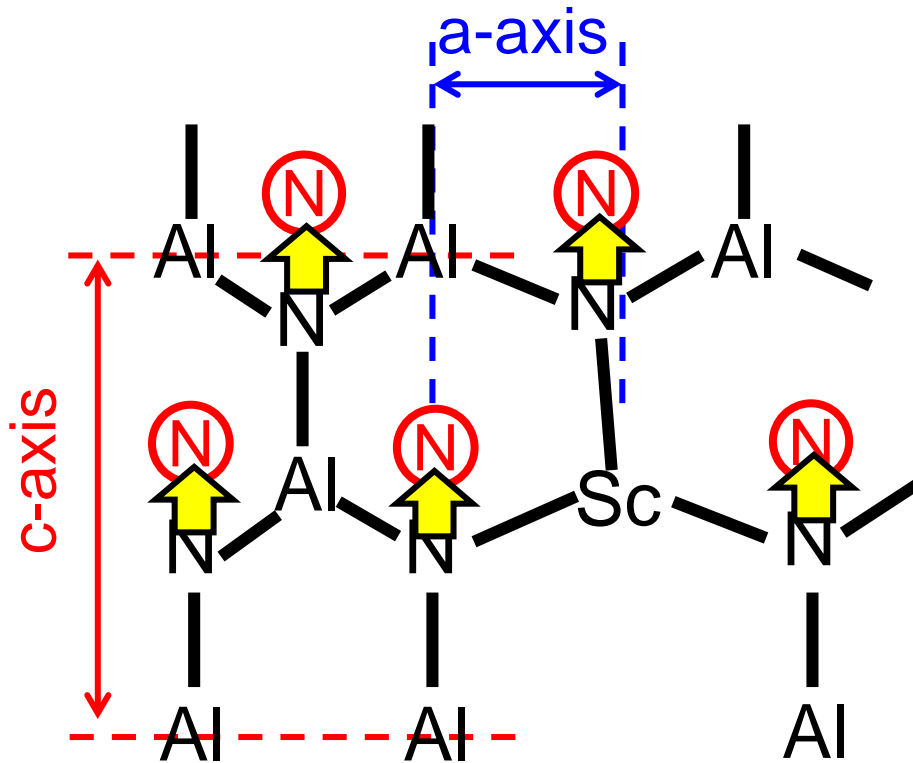


Figure 1.21 An illustration of the influences of how Sc-N bonding changes the a-axis and c-axis.

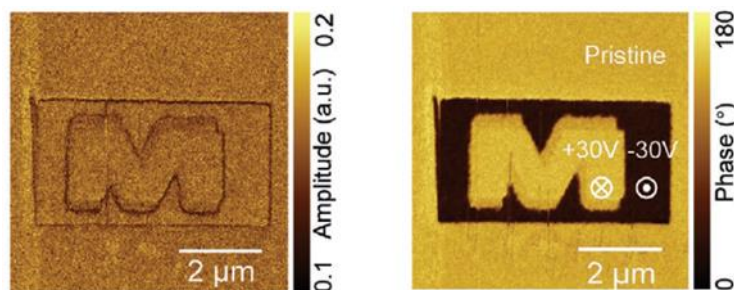


Figure 1.22 The ferroelectricity of AlScN is also confirmed by PFM [1.21].

The researcher study on the deposition at first. There are several kinds of deposition of AlScN layers have been studied such as RF sputter, DC sputtering, Co-sputtering, MOCVD, and ALD [1.22]. Then, the researcher study on the thickness scaling on different electrodes [1.23~1.26]. Next, the endurance for memory applications and the mobility for TFT have been evaluated for AlScN film [1.27~1.29]. The extremely large remanent polarization of AlScN also can apply to GaN HEMTs to shift its threshold voltage [1.30].

There are a few models to explain the switching in ferroelectric materials. A normally used model is Kolmogorov–Avrami–Ishibashi (KAI) model [1.31~1.32]. The polar switched from nucleation and become wider during the switching. AlScN follows the KAI model [1.33]. Figure 1.23(a) shows the switching illustrations of the KAI model [1.31]. Another normally used model is the nucleation-limited switching (NLS) model [1.34]. HfO₂ and PZT follow this model which the area is switched independently. Figure 1.23(b) shows the switching illustrations of the NLS model.

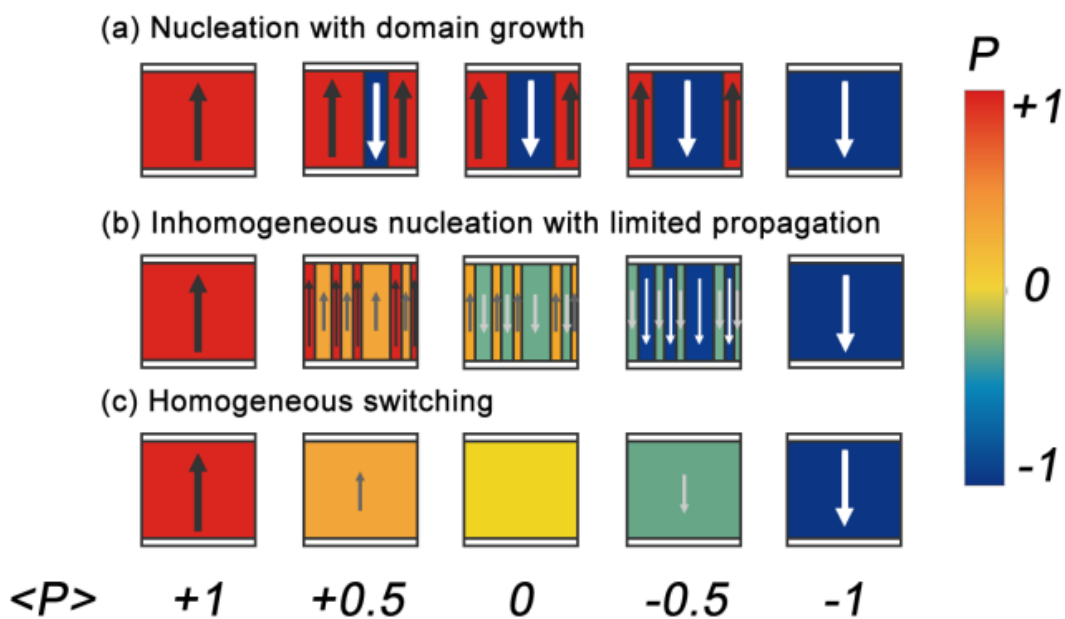


Figure 1.23 Different switching models of ferroelectric materials [1.31].

Table 1.2 compared ferroelectric properties between PZT HfO₂ and AlScN. AlScN has the largest remanent polarization and the wurtzite structure of AlScN make it easier to be deposited. However, the endurance test of AlScN has not been reported yet then [1.11].

Table 1.2 Comparisons of ferroelectric properties between PZT HfO₂ and AlScN.

Ferroelectric material	Bandgap (eV)	Remnant polarization ($\mu\text{C}/\text{cm}^2$)	Coercive field (MV/cm)	Ferroelectric phase	Thickness scaling	Endurance
PZT	~3.3	~20	0.1	meta-stable (perovskite)	100nm	10^{13}
HfO ₂	5.5	1~45	1~2	meta-stable (orthorhombic)	3nm	$\sim 10^{11}$
Al _{1-x} Sc _x N	3~4	~100	2~4	Stable (wurtzite)	9nm [*]	N/A

1.6 Ferroelectric AlScN films for NVM devices

A demonstration of the AlScN FTJ device has been reported in 2022 [1.21]. Figure 1.24 showed a demonstration of the AlScN ferroelectric tunnel junction. Single-crystalline Al_{0.82}Sc_{0.18}N (100nm) is deposited on a GaN layer. With a heterostructure of AlScN/ GaN, the Schottky barrier height change by switching the polarity of AlScN. Figure 1.25 showed that the on/off ratio over 200 and 10^4 switching cycles are reached.

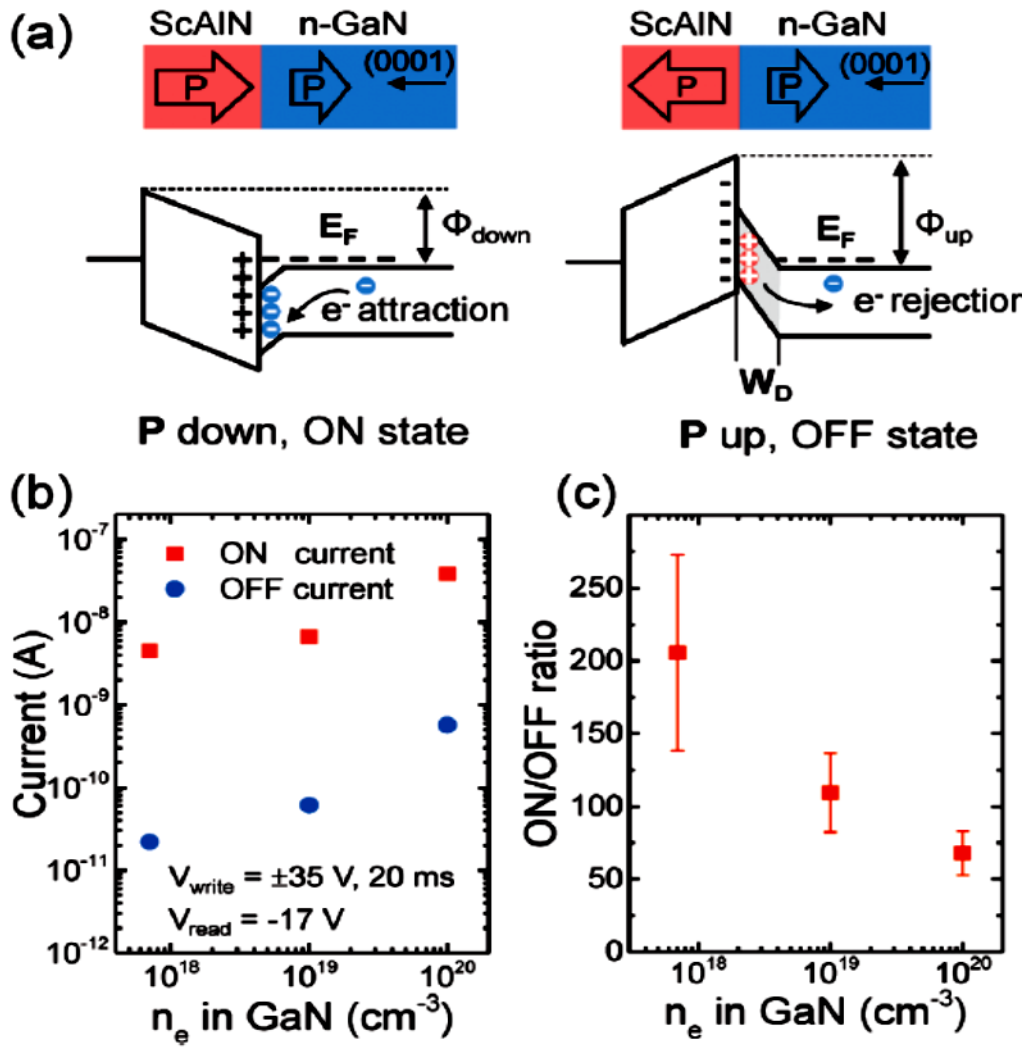


Figure 1.24 A demonstration of AlScN ferroelectric tunnel junction [1.21].

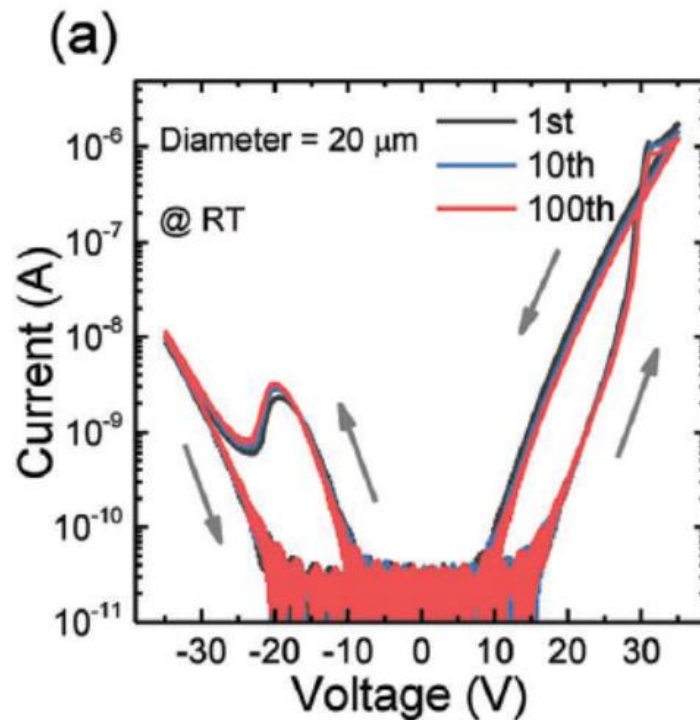


Figure 1.25 An on/off ratio over 200 AlScN FTJ [1.21].

1.7 Conclusion

In conclusion, topics for ferroelectric AlScN research reported so far include AlScN structure analysis (XRD) [1.11]; Sc composition dependence [1.12]; Thickness scaling [1.11]; Theoretical study on ferroelectric wurtzite structure [1.35]; Device demonstration (limited to epitaxial layers) [1.21].

And research which is required to be done includes Process temperature for back-end-of-line (BEOL) compatibility; Deposition process (CVD/ALD, etc.); Thickness scaling below 10 nm; Reliability: switching endurance and breakdown mechanism; Variability.

1.8 Purpose of this thesis

The purpose of this thesis is to understand the degradation and breakdown mechanism of ferroelectric AlScN films. And to propose a process for high-reliable ferroelectric films with thickness scalability.

1.9 Outline of this thesis

In chapter 1, an overview of DRAM and ferroelectric AlScN films are introduced. In chapter 2, the characterization methods used in this thesis are reviewed. The experiment results start from chapter 3 to chapter 6. In chapter 3, the low-temperature formation of ferroelectric AlScN films is discussed. Due to the typical edging effect found, the reliability and breakdown mechanism of ferroelectric AlScN films are explained in chapter 4. In chapter 5, the scalability of AlScN is evaluated. The V_N in AlScN gives difficulty in thickness scaling. The way of incorporating oxygen atoms to suppress V_N for the purpose of further thickness scaling will be explained in chapter 6. Concluding the four research, AlScON/AlScN stacking for reliable ferroelectric films is shown in chapter 7. In the end, I will conclude my research in chapter 8. Figure 1.26 shows the doctoral thesis structure.

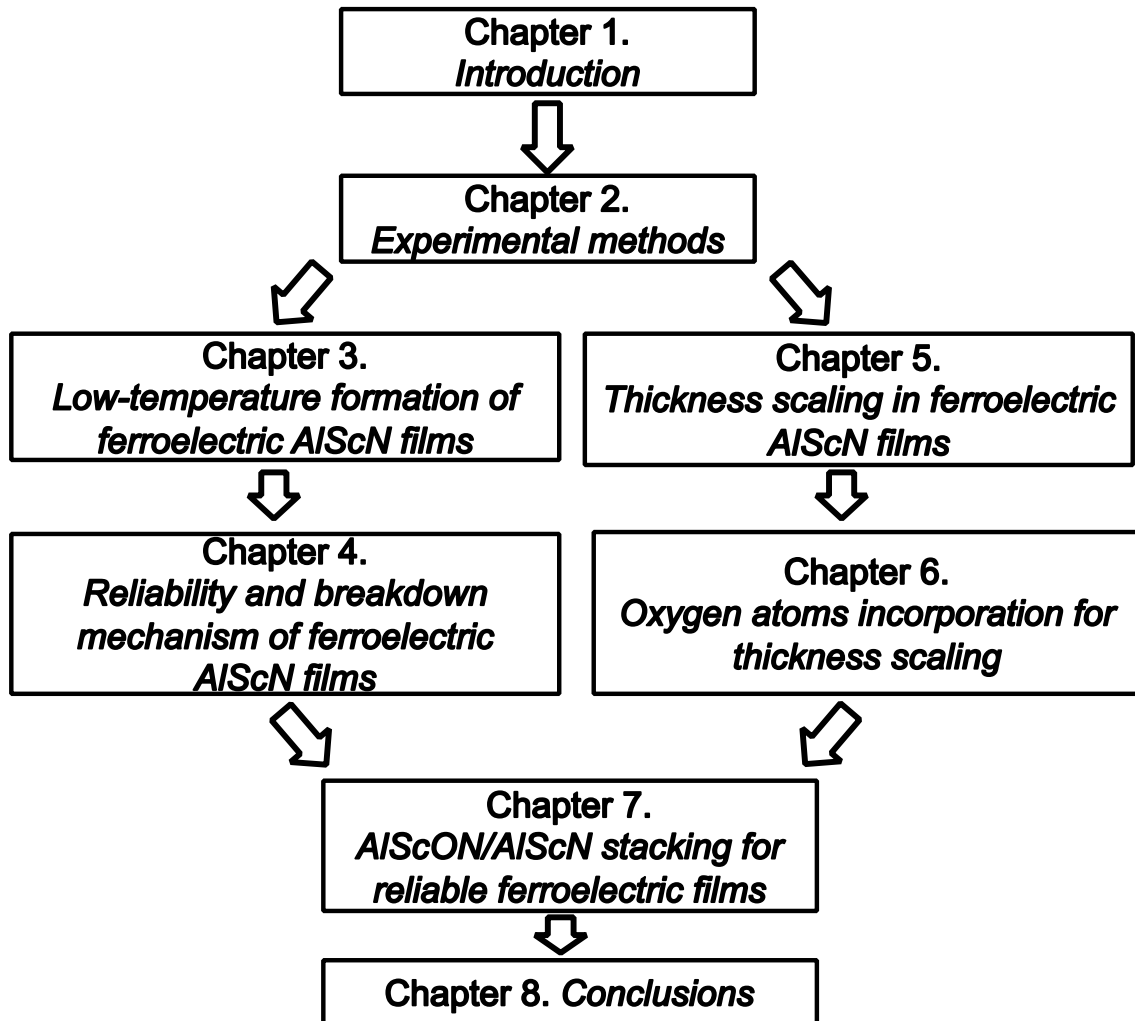


Figure 1.26 Doctoral thesis structure.

Reference

- [1.1] T Schenk, et al., Rep. Prog. Phys., 83, 086501 (2020)
- [1.2] FUJITSU, FUJITSU SEMICONDUCTOR MEMORY MANUAL FRAM Guide Book, <https://www.fujitsu.com/downloads/MICRO/fme/fram/fram-guide-book.pdf>, chap. 2, p.10
- [1.3] Z. Fan, et al, J. Adv. Dielec., 6, 1630003 (2016)
- [1.4] T. S. Boscke, Appl. Phys. Lett. 99, 102903 (2011)

- [1.5] T. Mikolajick, *J. Appl. Phys.*, 129, 100901 (2021)
- [1.6] J. Okuno, *et al.*, *VLSI Tech.* (2020)
- [1.7] M. Trentzsch, *et al.*, *IEDM* (2016)
- [1.8] S. Fujii, *et al.*, *VLSI Tech.* (2016)
- [1.9] Pešić, M., Künneth, C., Hoffmann, M. et al. A computational study of hafnia-based ferroelectric memories: from ab initio via physical modeling to circuit models of ferroelectric device. *J Comput Electron* 16, 1236–1256 (2017)
- [1.10] R. Deng, S. R. Evans, D. Gall, “Bandgap in $Al_{1-x}Sc_xN$ ”, *Appl. Phys. Lett.*, 102, 112103 (2013).
- [1.11] S. Yasuoka, *J. Appl. Phys.*, 128, 114103 (2020)
- [1.12] S. Fichtner, N. Wolff, F. Lofink, L. Kienle, and B. Wagner, “AlScN: A III-V semiconductor based Ferroelectric,” *J. Appl. Phys.* 125, 114103 (2019).
- [1.13] G. Liu and C.-W. Nan, “Thickness dependence of polarization in ferroelectric perovskite thin films,” *J. Phys. D: Appl. Phys.* 38, 584–589 (2005).
- [1.14] M. Fukunaga, M. Takesada, and A. Onodera, “Ferroelectricity in layered perovskites as a model of ultra-thin films,” *World J. Condens. Matter Phys.* 06, 224–243 (2016).
- [1.15] C.-P. Yeh, M. Lisker, B. Kalkofen, and E. P. Burte, “Fabrication and investigation of three-dimensional ferroelectric capacitors for the application of FeRAM,” *AIP Adv.* 6, 035128 (2016).
- [1.16] J. F. Ihlefeld, D. T. Harris, R. Keech, J. L. Jones, J.-P. Maria, and S. T. McKinstry, “Scaling effects in perovskite ferroelectrics: Fundamental limits and process-structure-property relations,” *J. Am. Ceram. Soc.* 99, 2537–2557 (2016)

- [1.17] T. S. Böscke, J. Müller, D. Bräuhaus, U. Schröder, and U. Böttger, “Ferroelectricity in hafnium oxide thin films,” *Appl. Phys. Lett.* 99, 102903 (2011).
- [1.18] H. K. Yoo, J. S. Kim, Z. Zhu, Y. S. Choi, A. Yoon, M. R. MacDonald, X. Lei, T. Y. Lee, D. Lee, S. C. Chae, J. Park, D. Hemker, J. G. Langan, Y. Nishi, and S. J. Hong, “Engineering of ferroelectric switching speed in Si doped HfO₂ for highspeed 1T-FERAM application,” in *IEEE International Electron Device Meeting (IEDM)* (2017), pp. 481–486
- [1.19] T. Ali, P. Polakowski, S. Riedel, T. Büttner, T. Kämpfe, M. Rudolph, B. Pätzold, K. Seidel, D. Lohr, R. Hoffmann, M. Czernohorsky, K. Kühnel, P. Steinke, J. Calvo, K. Zimmermann, and J. Müller, “High endurance ferroelectric hafnium oxide-based FeFET memory without retention penalty,” *IEEE Trans. Electron Devices* 65, 3769–3774 (2018).
- [1.20] Fichtner, Simon (2019). Development of high performance piezoelectric AlScN for microelectromechanical systems Towards a ferroelectric wurtzite structure. Germany: Books on Demand. Chapter 6, p.112
- [1.21] D. Wang, *Adv. Electron. Mater.*, 220005 (2022)
- [1.22] S.-L. Tsai, T. Hoshii, H. Wakabayashi, K. Tsutsui, T.-K. Chung, E. Y. Chang, and K. Kakushima, “Room-temperature deposition of a poling-free ferroelectric AlScN film by reactive sputtering,” *Appl. Phys. Lett.* 118, 082902 (2021).
- [1.23] S.-L. Tsai, T. Hoshii, H. Wakabayashi, K. Tsutsui, and K. Kakushima, “Thickness scaling on ferroelectric Al_{0.8}Sc_{0.2}N Films,” *Ext. Abstr. of the Int. Conf. on Solid State Devices and Materials*, 2020, p. A-1-05.
- [1.24] S. Tsai, T. Hoshii, H. Wakabayashi, K. Tsutsui, T. K. Chung, E. Y. Chang,

and K. Kakushima, *Jpn. J. Appl. Phys.* 60, SBBA05 (2021).

[1.25] R. Mizutani, *APEX*, 14, 1065501 (2021)

[1.26] Sung-Lin Tsai, Takuya Hoshii, Hitoshi Wakabayashi, Kazuo Tsutsui, Kuniyuki Kakushima, "Highly Oriented Growth of $\text{Al}_x\text{Sc}_{1-x}\text{N}$ Ferroelectric Film on W Bottom Electrodes", *ECS Transactions*, Vol.98, No.3, pp57-61, 2020.

[1.27] S. Tsai, T. Hoshii, H. Wakabayashi, K. Tsutsui, T. K. Chung, E. Y. Chang, and K. Kakushima, *Ext. Abstr. of the Int. Conf. on Advanced Metallization Conf.*, 2021, A21-22.

[1.28] Sung-Lin Tsai, Takuya Hoshii, Hitoshi Wakabayashi, Kazuo Tsutsui, Tien-Kan Chung, Edward Yi Chang, Kuniyuki Kakushima, "Field cycling behavior and breakdown mechanism of ferroelectric $\text{Al}_{0.78}\text{Sc}_{0.22}\text{N}$ films", *Japanese Journal of Applied Physics*, Vol. 61, SJ1005, 2022

[1.29] Junji Kataoka, Sung-Lin Tsai, Takuya Hoshii, Hitoshi Wakabayashi, Kazuo Tsutsui, Kuniyuki Kakushima, "N-type conduction of sputter-deposited polycrystalline $\text{Al}_{0.78}\text{Sc}_{0.22}\text{N}$ films by Si ion implantation", *Applied Physics Express*, Vol.14, 021002, 2021

[1.30] Chen Si-Meng, Tsai Sung-Lin, Mizutani Kazuto, HOSHII Takuya, WAKABAYASHI Hitoshi, TSUTSUI Kazuo, Chang Edward Yi, Kakushima Kuniyuki, "GaN high electron mobility transistors (HEMTs) with self-upward-polarized AlScN gate dielectrics toward enhancement-mode operation", *JJAP*, S1102745.R1, 2022

[1.31] B. Xu, V. Garcia, S. Fusil, M. Bibes, and L. Bellaiche, *Phys. Rev. B* 95, 104104 (2017).

[1.32] 石橋善弘著 Introduction to ferroelectrics 森北出版 2020.10 p.189

- [1.33] Simon Fichtner Development of High Performance Piezoelectric AlScN for Microelectromechanical Systems: Towards a Ferroelectric Wurtzite Structure BoD – Books on Demand, 2020 p.108
- [1.34] N. Gong, X. Sun, H. Jiang, et al., Appl. Phys. Lett. 112, 262903 (2018)
- [1.35] K. Furuta, et al. 2021 (Kyusyu Univ.)

Chapter 2

Experimental Methods

2.1 Physical Characteristics of AlScN film

XRD, XRC, XPS, and TEM are held to evaluate the structure and composition of AlScN films.

2.1.1 XRD (X-ray Diffractometer)

The crystallization can be revealed by XRD analysis [2.1]. The XRD measurements follow the Bragg condition. Identification is achieved by comparing the XRD pattern obtained from a given sample with an internationally recognized database. Figures 2.1 and 2.2 showed the illustrations of out-of-plane and in-plane XRD [2.2]. AlScN is wurtzite structure that is hexagonal. By calculating the equation of hexagonal structure from the XRD pattern and database, lattice parameters a and c can be realized.

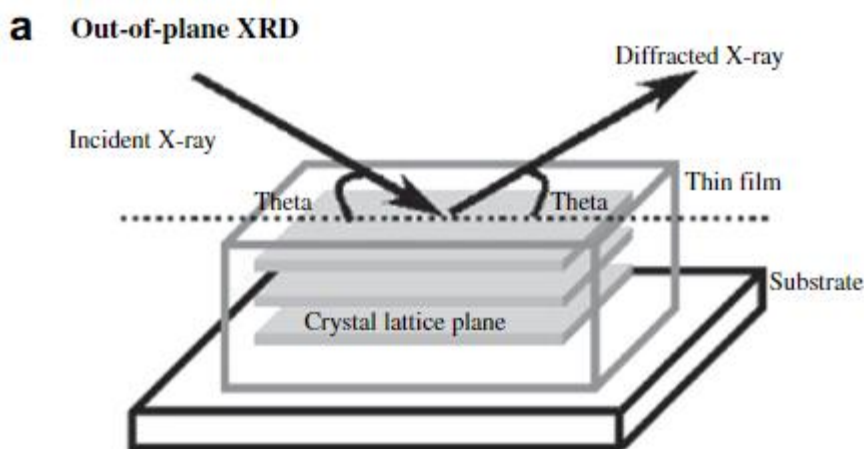


Figure 2.1 An illustration of out-of-plane XRD [2.2].

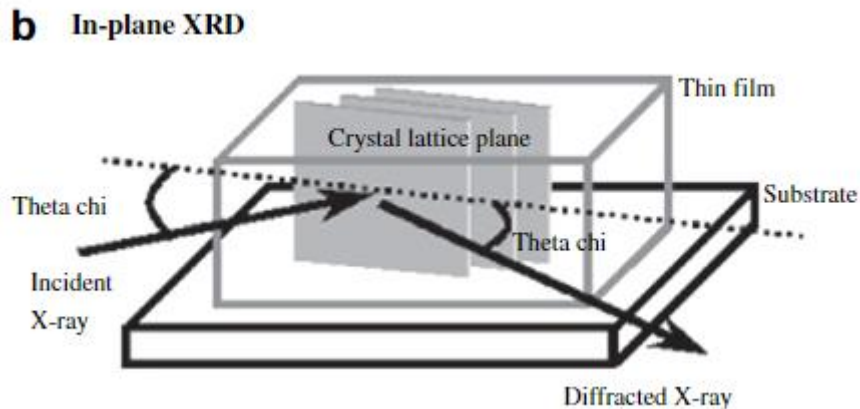


Figure 2.2 An illustration of in-plane XRD [2.2].

2.1.2 XRC (X-ray rocking curve)

Rocking curve measurements are doing θ scan at a fixed 2θ angle. The width of the peak is inversely proportional to the dislocation density in the film. The quality of the crystallization can be revealed by XRC analysis. Full-width-half-maximum shows how the quality of the crystallization of the material is [2.1].

2.1.3 XPS (X-ray Photoelectron Spectroscopy)

When an excitation source is incident on atoms or solid surfaces, electrons carrying characteristic kinetic energy can be ejected from the atoms or solid surfaces. We can identify the chemical state of surface atoms by the ejected electrons. Thus, it can show the composition of the material by XPS analysis [2.1].

2.1.4 TEM (Transmission Electron Microscope)

TEM images show the images of the cross-section. We can know spatial information in atomic resolution. Fast-Fourier-transforming (FFT) TEM images also show the crystallization and the grain size of the material. The results after FFT are close to the selected area diffraction (SAD) results [2.1].

2.2 Electrical Characteristics of AlScN film

JV, CV, PUND, and fatigue measurements are held to evaluate AlScN films.

2.2.1 JV measurement

By evaluating the JV measurement, the mechanism of the leakage current will be revealed. Figure 2.3 show the typical carrier conduction mechanism of the layer [2.3]. One of the groups apply the leakage current to a different conduction model and figured out that the mechanism of the leakage current of PZT is Poole-Frenkel conduction [2.4]. Another group figured out that the mechanism of the leakage current of AlScN is due to its low Schottky barrier height which leads to the Schottky emission conduction [2.5]. We can also obtain the optical dielectric constant, and Schottky barrier height by JV measurements under different temperatures.

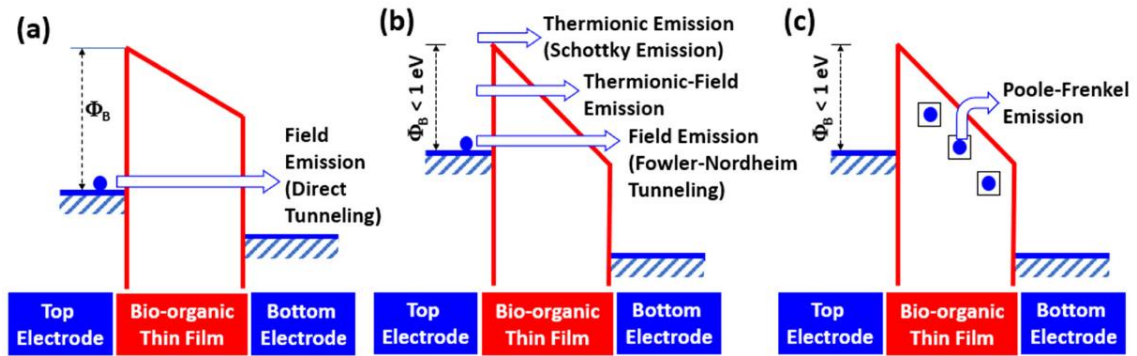


Figure 2.3 Illustrations of different carrier conduction mechanisms [2.3].

2.2.2 CV measurement

A typical CV measurement of ferroelectric material is a hysteresis loop. The appearance of peak capacitance represents the polar switching. The electrical field of the peak capacitance also represents the coercive field. However, the switching in AlScN is slow, so the applied voltage of peak capacitance is lower than the coercive field which is measured from PV measurements. Figure 2.4 shows the relations between PV and CV curves.

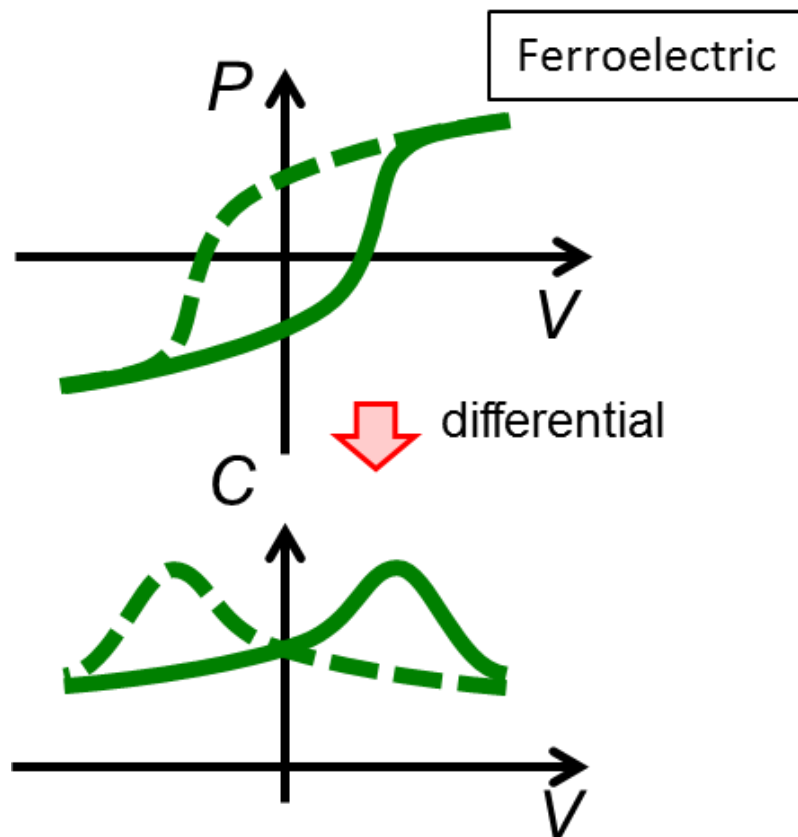


Figure 2.4 The relations between hysteresis PV and CV curves.

2.2.3 PUND measurement

Positive-Up-Negative-Down, as well as PUND measurements, are usually held for those high leakage current ferroelectric materials. The pulses of PUND measurements are like in figure 2.5 [2.6]. The first negative pulse is to preset the polar before measuring. The first positive pulse includes the switching signal and leakage current. The second positive pulse includes only leakage current. By comparing these two measurements, we can know the amount of the remanent polarization. So as the negative pulse measurements.

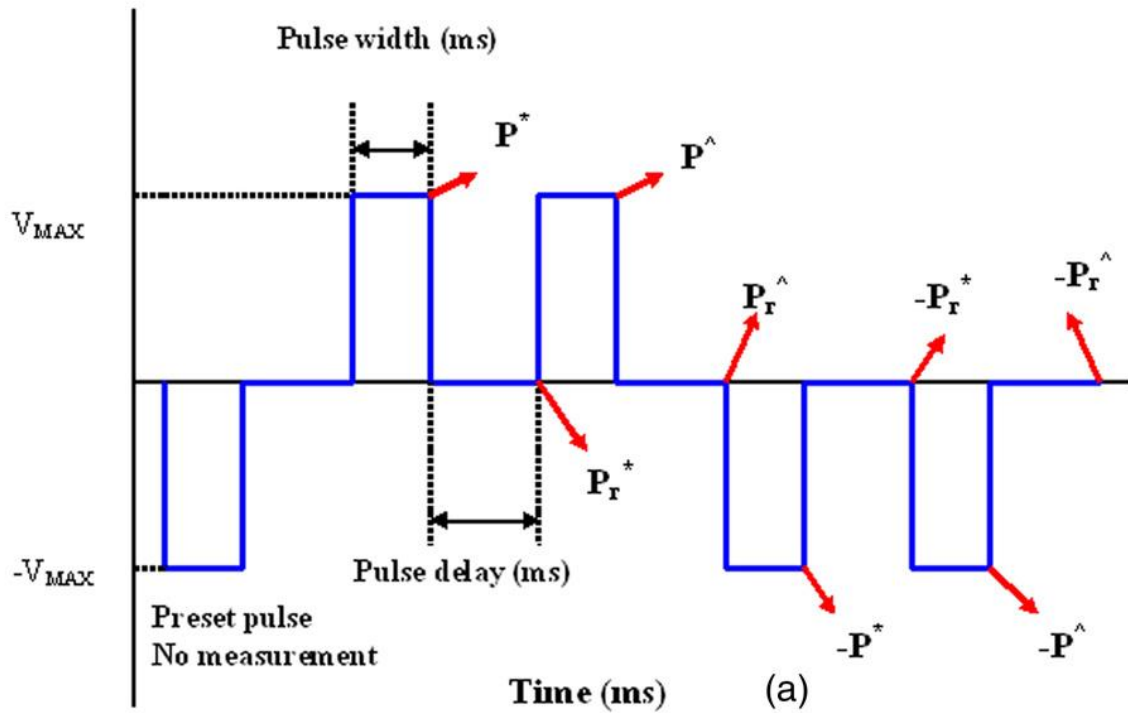


Figure 2.5 An illustration of PUND measurement [2.6].

2.2.4 Fatigue measurement

A switching cycle remains a positive pulse and a negative pulse. The fatigue measurement also called endurance tests is counting the switching cycles and holding the PUND measurements before the device breakdown.

References

[2.1] 半導體材料分析技術與見習 NM01 講義

[2.2] K. Kato, H. Omoto, A. Takamatsu, Vacuum, 84 (2010), p. 587

- [2.3] Cheong, Kuan Yew, Tayeb, Ilias Ait, Zhao, Feng and Abdullah, Jafri Malin. "Review on resistive switching mechanisms of bio-organic thin film for non-volatile memory application" *Nanotechnology Reviews*, vol. 10, no. 1, 2021, pp. 680-709.
- [2.4] P. Zubko, D.J. Jung, J.F. Scott Electrical characterization of $\text{PbZr}_{0.4}\text{Ti}_{0.6}\text{O}_3$ capacitors, *J. Appl. Phys.*, 100, 114113 (2006)
- [2.5] J. Katoaka, S.-L. Tsai, T. Hoshii, H. Wakabayashi, K. Tsutsui, and K. Kakushima, "A possible origin of the large leakage current in ferroelectric $\text{Al}_{1-x}\text{Sc}_x\text{N}$," *Jpn. J. Appl. Phys.* 60, 03907 (2021).
- [2.6] S Satapathy, P K Gupta, and K B R Varma, "Enhancement of nonvolatile polarization and pyroelectric sensitivity in lithium tantalate (LT)/poly (vinylidene fluoride) (PVDF) nanocomposite," *J. Phys. D: Appl. Phys.*, 42, 055402 (2009)

Chapter 3

Low-temperature formation of ferroelectric AlScN films

3.1 Room-Temperature Deposited Ferroelectricity AlScN

Film

Non-volatile memories have been used for IoT devices. PZT and HfO₂ have been used for FRAM [3.1~3.4]. However, both these materials have their issues to be solved. PZT has a scaling issue and obtains harmful material Pb [3.5~3.8]. Although HfO₂ has the potential to become a new ferroelectric material for FRAM, it has the wake-up effect and degradation issues [3.9~3.11]. A new ferroelectric material AlScN has been found in 2019 [3.12]. The remanent polarization which is over 100 $\mu\text{C}/\text{cm}^2$ is extremely large compared to HfO₂.

It is important to keep the temperature of deposition low for the whole fabrication process. PZT layer used to need extremely high-temperature annealing for crystallization. HfO₂ also needs high temperature or long deposition time for crystallization. In this chapter, room-temperature deposited AlScN film is evaluated [3.13]. Table 3.1 shows reported ferroelectric AlScN films which are deposited at rather high temperatures, the thicknesses are too thick for NVM applications, or even CMOS unfriendly metal electrodes.

Table 3.1 Reported ferroelectric AlScN films [3.12, 3.14, 3.15].

Reference	Deposition	Temperature (°C)	Crystal	Thickness (nm)	Electrodes
S. Fichtner, J. Appl. Phys., 125, 114103 (2019)	Sputter	400°C	poly-crystalline	600	Pt
S. Yasuoka, J. Cera. Soc. Jpn, 130, 436 (2022)	Sputter	400°C	Poly-crystalline	12~130	Pt
P. Wang, Appl. Phys. Lett., 119, 082101 (2021)	MBE	600°C~900°C	epitaxy	100	Si:GaN

The purpose of this chapter is to analyze the capability of low-temperature deposition with a thickness of 50 nm.

3.2 Fabrication process of AlScN Capacitors with Different Deposition Temperatures

First, the n⁺Si wafer was cleaned with H₂SO₄+H₂O₂ for 10 minutes for the purpose of oxidating organic particles. It is also cleaned by 1% BHF for 1 minute to remove SiO₂. Then, bottom electrodes TiN were deposited by radiofrequency (RF) reactive sputtering in Ar 4 sccm, N₂ 6 sccm ambient at 0.2 pa chamber pressure. The 50 nm thick AlScN film was deposited by DC reactive sputtering from an Al_{0.57}Sc_{0.43} target in Ar 5 sccm, N₂ 10 sccm ambient at 0.7 pa chamber pressure. Top electrodes TiN were deposited by RF reactive sputtering in Ar and N₂ ambient. The deposition process was held at room temperature (RT) and 400 °C separately. The power of sputtering was 300W and the target to substrate distance was 100mm. The base pressure of the chamber is about 10⁻⁶ Pa. The TiN top electrode was patterned by wet etching in a mixed solution of NH₄OH, H₂O₂, and H₂O. The fabrication process flow and the schematic illustration of the fabricated metal-insulator-metal (MIM) capacitors are shown in figures 3.1 and 3.2, respectively. The details of the deposition conditions of AlScN thin films and TiN electrodes are shown in figures 3.3 and 3.4, respectively.

- n⁺Si substrate cleaning
 - Sputter-deposited TiN (10nm) for bottom electrode @ (RT&400°C)
 - ★ ● Sputter-deposited Al_{0.78}Sc_{0.22}N (50nm) @ (RT&400°C)
 - Sputter-deposited TiN (40nm) for top electrode @ (RT&400°C)
 - Photolithography
 - Etching by wet etching
 - Backside Al deposition
- ↓

Figure 3.1 Fabrication process flow of AlScN MIM capacitor.



Figure 3.2 A schematic illustration of the fabricated AlScN MIM capacitor.

- ★ AlScN deposition conditions
- Target : Al_{0.57}Sc_{0.43}
 - DC sputter 300W @ (RT&400°C)
 - Ar : 5 sccm, N₂: 10 sccm @ 0.7Pa
 - T/S=100mm

Figure 3.3 The details of deposition conditions of AlScN thin films.

TiN deposition conditions

- Target : Ti
- RF sputter 300W @ (RT&400°C)
- Ar : 4 sccm, N₂: 6 sccm @ 0.2Pa
- T/S=100mm

Figure 3.4 The details of deposition conditions of TiN electrodes.

3.3 Experiment results of AlScN Capacitors with Different Deposition Temperatures

Figure 3.5 showed out-of-plane and in-plane XRD of room-temperature and 400 °C deposited samples. The out-of-plane XRD revealed the (002) plane at 35.5 °. The in-plane XRD revealed (100) plane at 31°. Both of the patterns showed the wurtzite structure for room-temperature and 400 °C deposited samples.

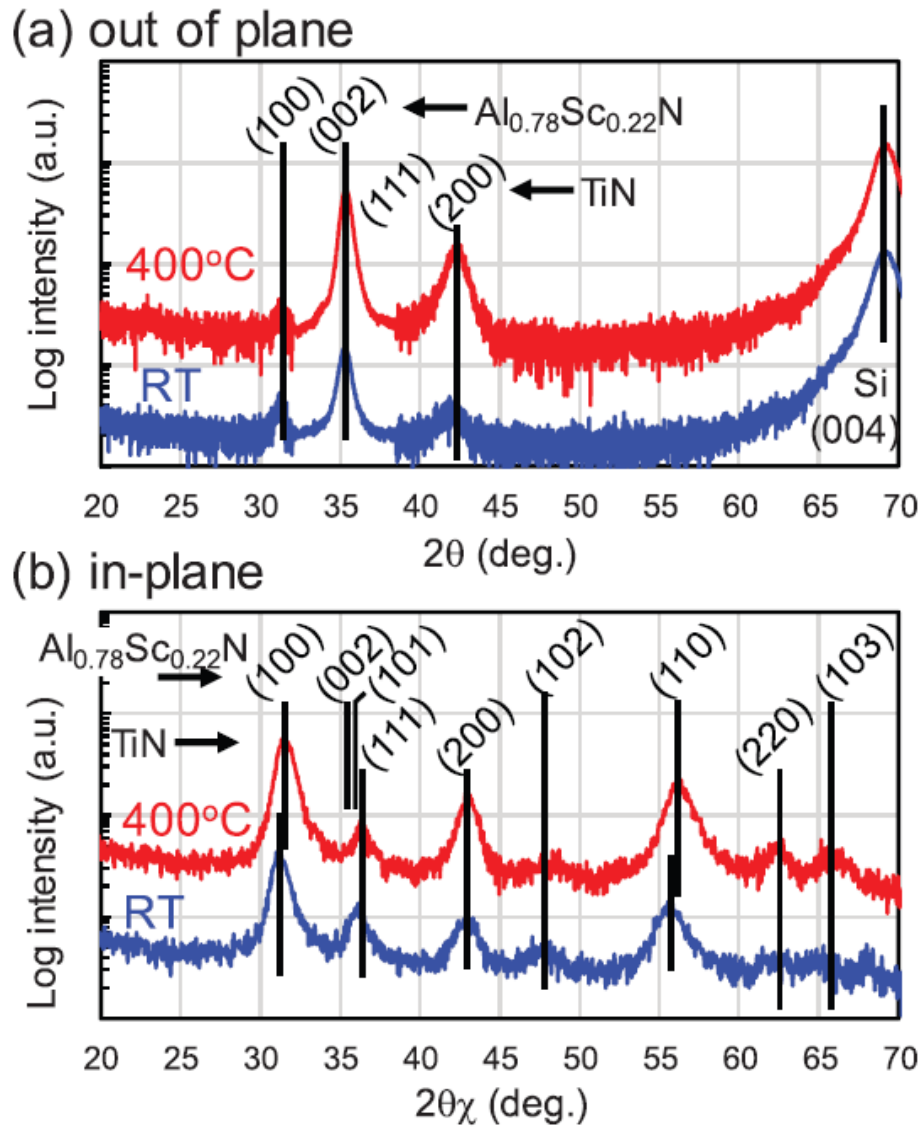


Figure 3.5 (a) Out-of-plane and (b) in-plane XRD results with different deposition temperatures.

Figure 3.6 showed the rocking curves of (002) plane of room-temperature and 400 °C deposited samples. The lower FWHM of 400 °C deposited samples revealed the better crystallization is.

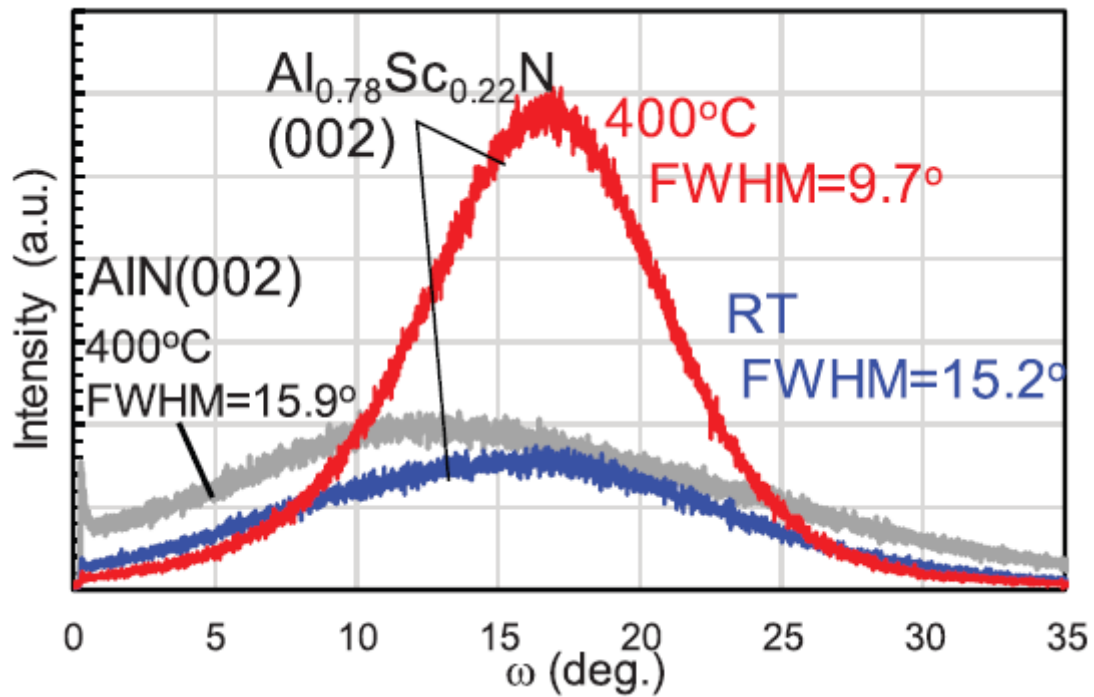


Figure 3.6 (c) Rocking curve results with different deposition temperature

Figure 3.7 showed the TEM images which showed the cross-section of room-temperature and 400 °C deposited samples. Both dark field images showed the columnar growth of the AlScN layer. The grain size of 50nm times 20nm is confirmed. It is hard to tell the difference between AlScN from the TEM images. By fast Fourier transforming the TEM images, better oriental growth is also obtained by 400 °C deposited samples.

Figure 3.8(a) showed the random growth of room temperature deposited TiN and figure 3.8(c) showed the oriented growth of 400 °C deposited TiN. Regardless of the growth of TiN, both AlScN showed oriented growth.

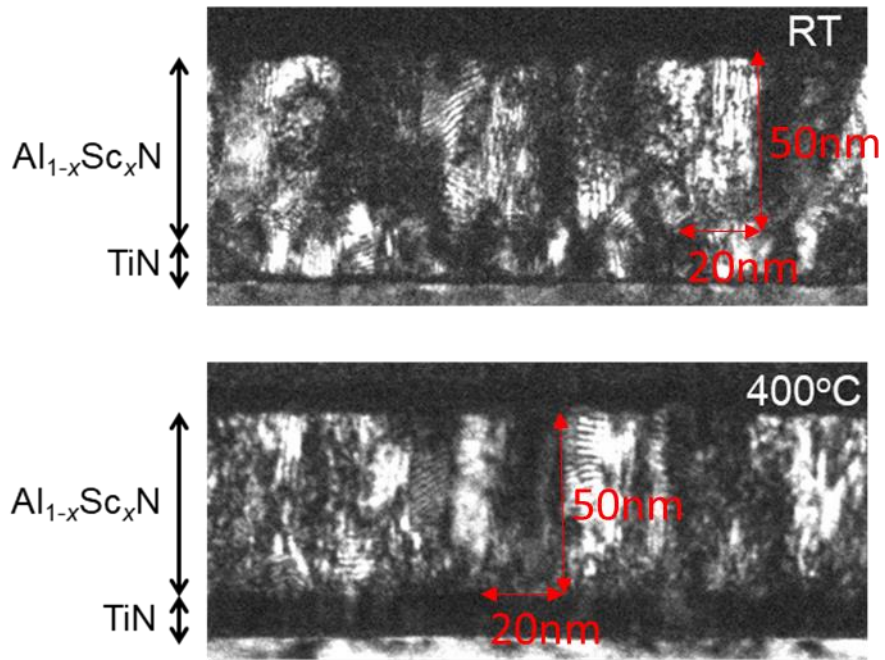


Figure 3.7 TEM image of 400 °C -deposited sample.

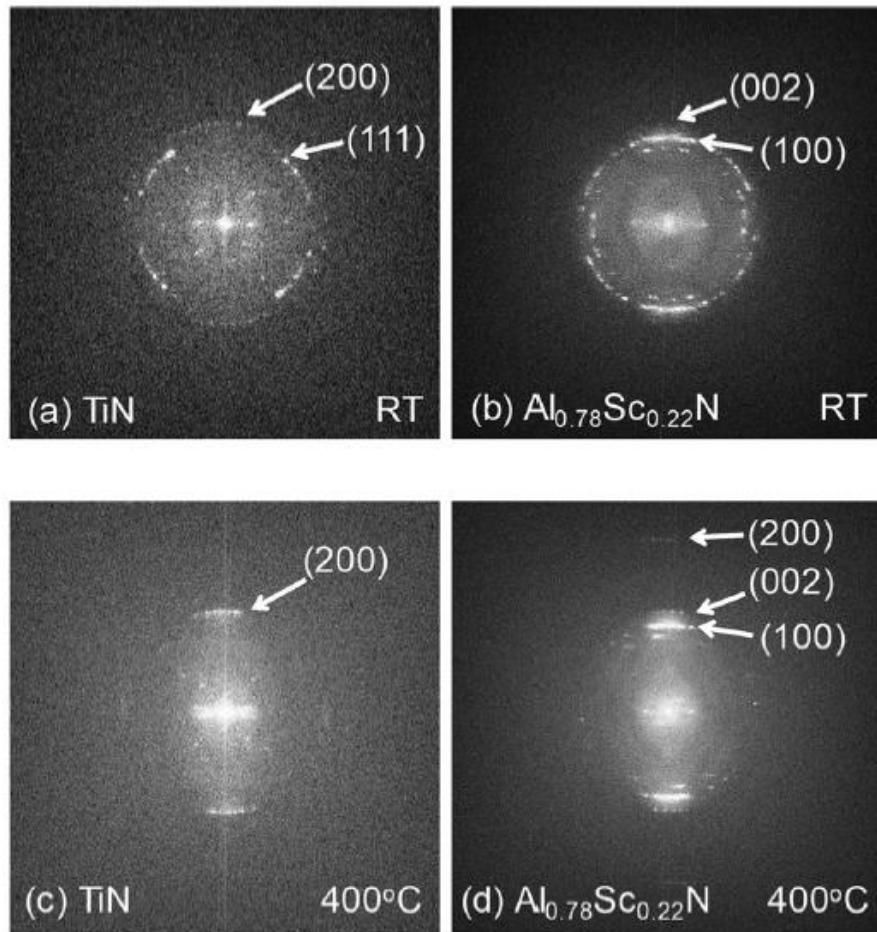


Figure 3.8 Fast Fourier transformed TEM images of room-temperature and 400°C deposited TiN and AlScN.

Figure 3.9 show the JV measurement of room-temperature and 400 °C deposited samples. A lower leakage current is shown for 400 °C deposited sample. A higher breakdown field is also shown for 400 °C deposited samples. The reason may be the better crystallization for 400 °C deposited sample.

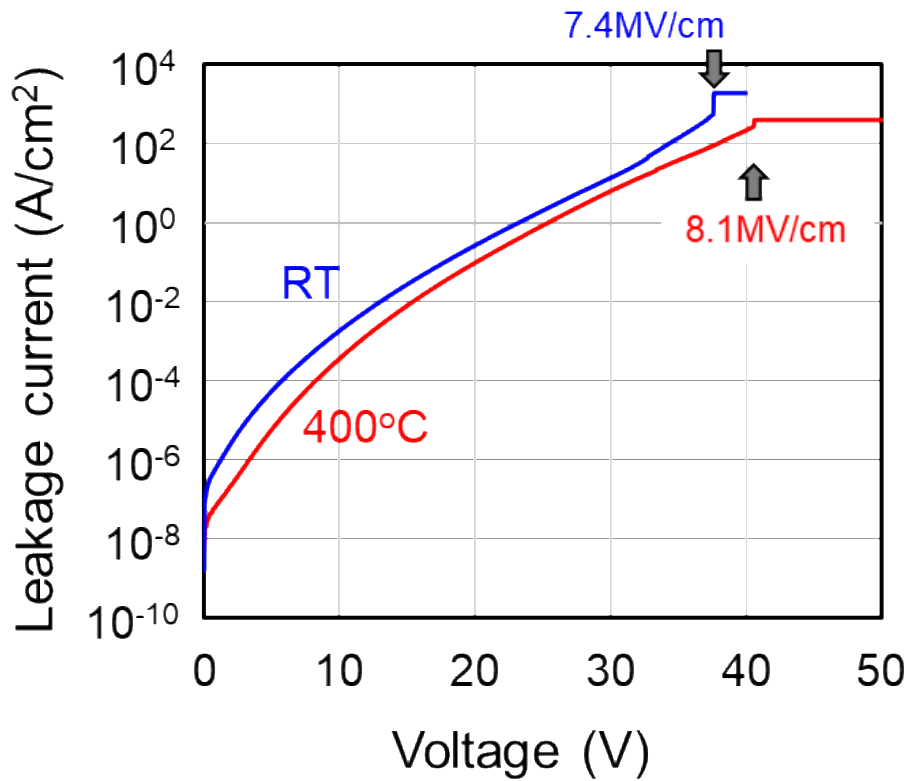


Figure 3.9 *JV* curves of AlScN MIM capacitor with different deposition temperatures for TiN button electrodes.

Figure 3.10 showed the CV measurement of room-temperature and 400 °C deposited samples. Both samples showed butterfly-like hysteresis loops. The peak capacitance occurred at -15V and 12V for 400 °C deposited sample. The reason is that if we apply a positive voltage, the polar of AlScN will switch to the polar as the same as which it deposited. Thus, it is harder to change the polar by applying a negative voltage and it is easier to change the polar by applying a positive voltage. The steeper the capacitance change also indicates the larger polar switching for 400 °C deposited samples.

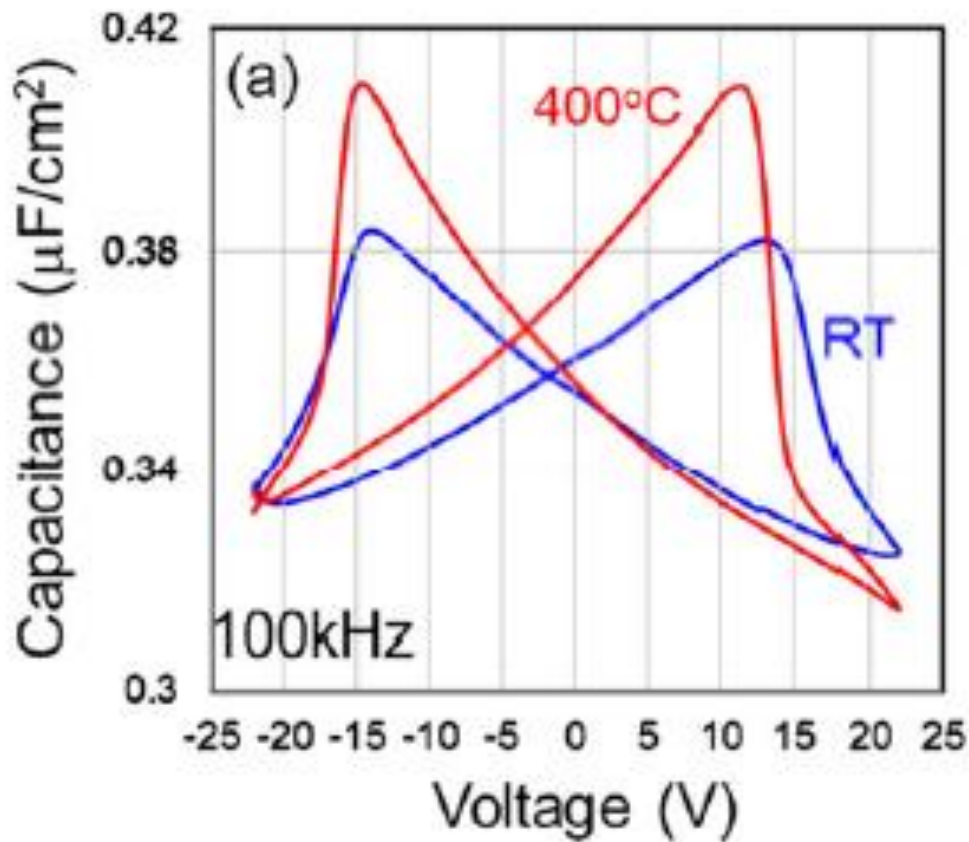


Figure 3.10 CV curves of AlScN MIM capacitor with different deposition temperatures for TiN button electrodes.

Figure 3.11 showed the triangle-PUND measurement of room-temperature and 400 °C deposited samples. The noise by leakage current becomes minor by these measurements. The remanent polarization of 80 $\mu\text{C}/\text{cm}^2$ was enhanced to 110 $\mu\text{C}/\text{cm}^2$ by the 400 °C deposited samples. The coercive field is about 5.6MV/cm for each sample at 10kHz. The coercive field may not be accurate here since there exists an easy switching domain and hard switching domain in AlScN. More details will be discussed in chapter 4.

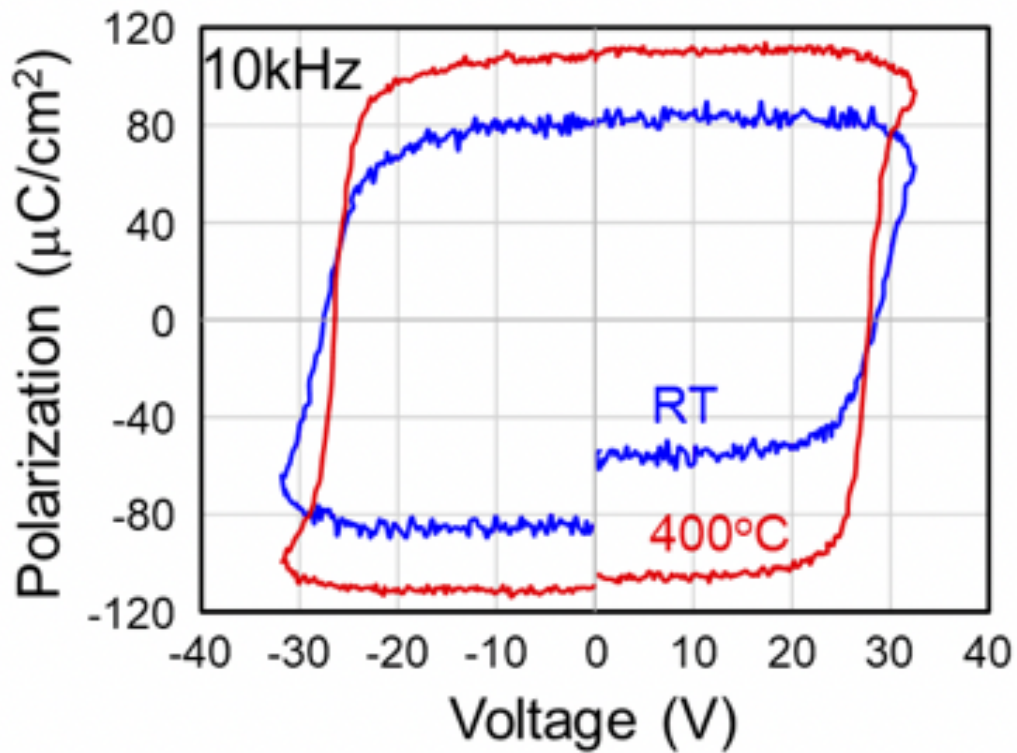


Figure 3.11 *PV* curves of AlScN MIM capacitor with different deposition temperatures for TiN button electrodes by tri-PUND measurements.

Figure 3.12 showed the current measurements during the PUND measurements. The current with switching signals is higher than the non-switching signals. By calculating these two signals the remanent polarization is $77 \mu\text{C}/\text{cm}^2$ for room-temperature deposited samples and $177 \mu\text{C}/\text{cm}^2$ for 400°C deposited samples. The higher values of remanent polarization for 400°C deposited samples may due to better crystallization.

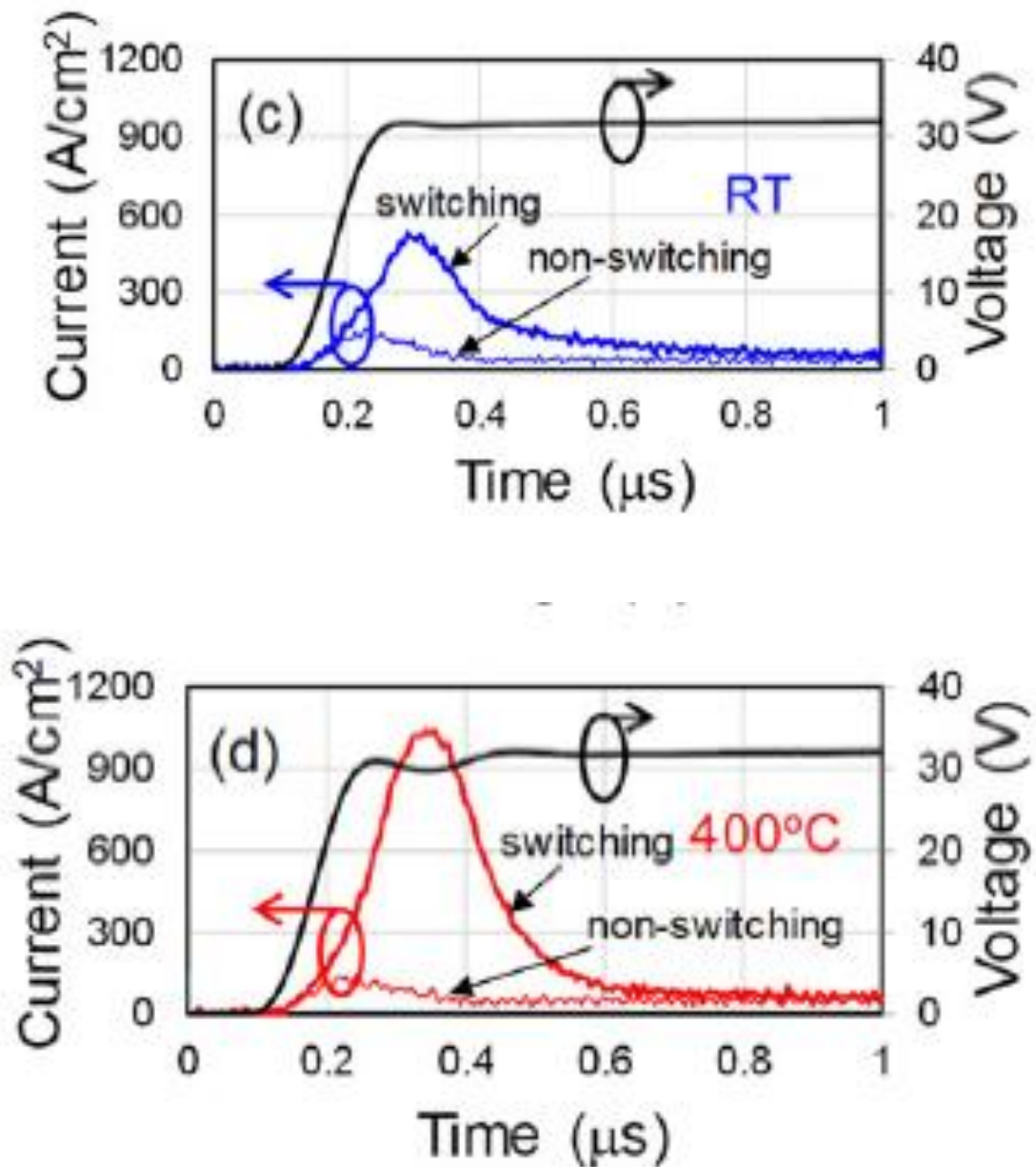


Figure 3.12 Current measurements during the PUND measurements with different deposition temperatures MIM capacitors.

Figure 3.13 shows the benchmark of low-temperature deposited and 400 °C deposited samples. Obtained P_r and E_c are consistent with the literature. The feasibility of room-temperature formed AlScN was demonstrated.

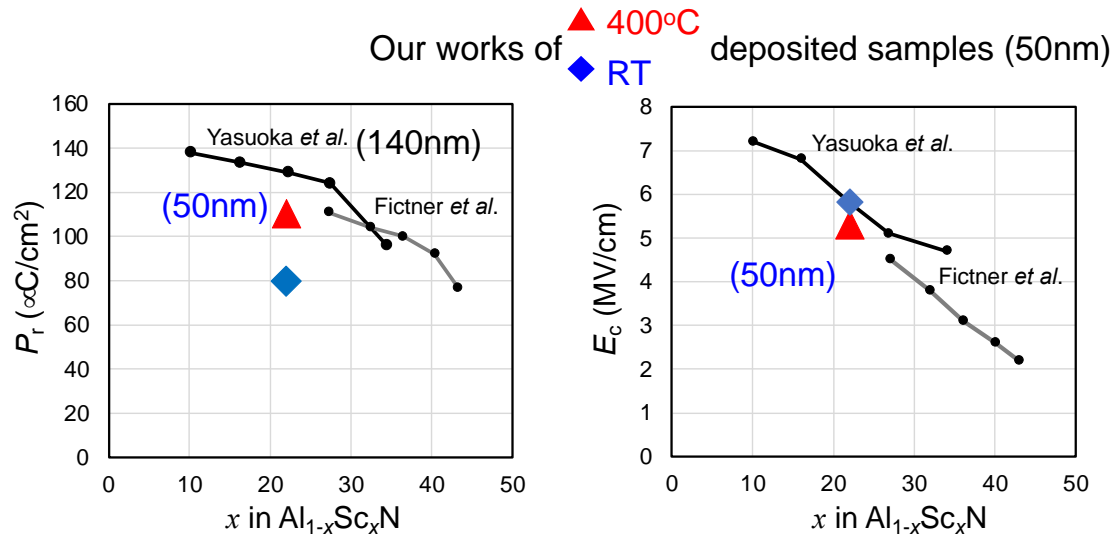


Figure 3.13 Benchmark of low temperature deposited and 400°C deposited samples.

Figure 3.14 showed the poling-free behavior for room-temperature deposited AlScN films and 400 °C deposited AlScN films. For the process of applying positive voltage first, AlScN film will stay in the same state as it was deposited. Then, switching at the first time when we apply a negative voltage. On the contrary, for the process of applying a negative voltage first, AlScN film will switch to the opposite polar simultaneously. This phenomenon showed the as-deposited polar and become an advantage of no need to poling for showing ferroelectricity.

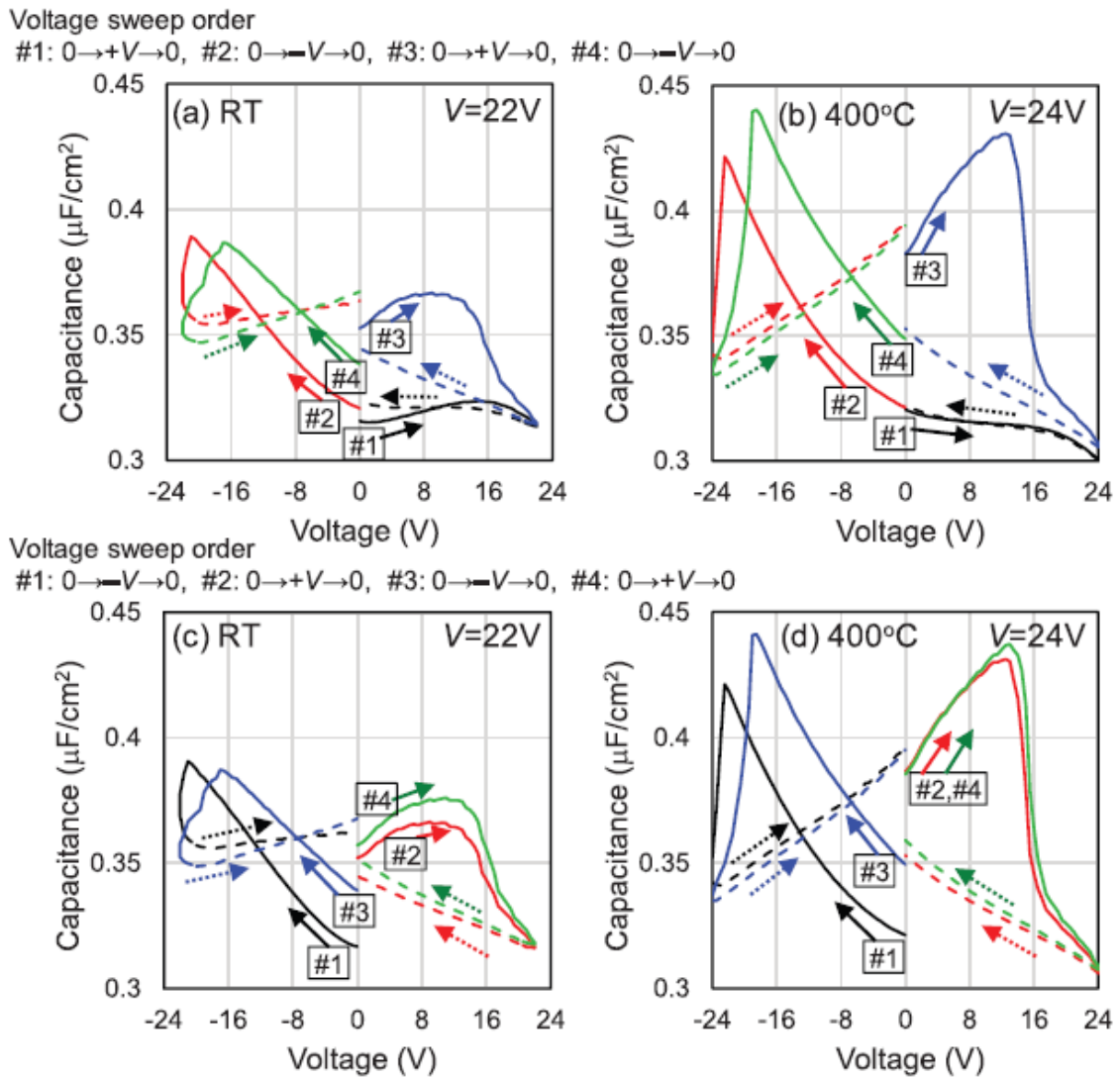


Figure 3.14 The poling-free measurements with different deposition temperature MIM capacitors.

3.4 Summary of this chapter

The purpose of this chapter is to demonstrate low-temperature formation with a thickness of 50 nm.

Room-temperature and 400 °C deposited AlScN MIM capacitors have been fabricated. The crystallizations were analyzed by XRD, XRC, and TEM. Both samples

showed c-axis oriented growth wurtzite-type crystallization and grain size of 50 nm*20 nm. XPS analysis showed the composition of ASN thin film is $\text{Al}_{0.78}\text{Sc}_{0.22}\text{N}$. *JV*, *CV*, *PV*, *PUND*, and fatigue measurements were held to analyze the electrical properties of room-temperature and 400 °C deposited AlScN MIM capacitors. Ferroelectricity was observed with a thickness of 50 nm. Ferroelectric hysteresis was also observed with a low-temperature process (RT). A high breakdown field of 8.1 MV/cm is observed for 400°C deposited sample. The *CV* measurements also show poling-free behavior for both AlScN MIM capacitors which the surface is initially N-face.

References

- [3.1] J. F. Scott and C. A. P. Araujo, "Ferroelectric memories," *Science* 246, 1400–1405 (1989).
- [3.2] B. H. Park, B. S. Kang, S. D. Bu, T. W. Noh, J. Lee, and W. J., "Lanthanum substituted bismuth titanate for use in non-volatile memories," *Nature* 401, 682–684 (1999).
- [3.3] P. K. Larsen, R. Cuppens, and G. A. C. M. Spierings, "Ferroelectric memories," *Ferroelectrics* 128, 265–292 (1992).
- [3.4] Y. Arimoto and H. Ishiwara, "Current status of ferroelectric random-access memory," *MRS Bull.* 29, 823–828 (2004).
- [3.5] G. Liu and C.-W. Nan, "Thickness dependence of polarization in ferroelectric perovskite thin films," *J. Phys. D: Appl. Phys.* 38, 584–589 (2005).

- [3.6] M. Fukunaga, M. Takesada, and A. Onodera, "Ferroelectricity in layered perovskites as a model of ultra-thin films," *World J. Condens. Matter Phys.* 06, 224–243 (2016).
- [3.7] C.-P. Yeh, M. Lisker, B. Kalkofen, and E. P. Burte, "Fabrication and investigation of three-dimensional ferroelectric capacitors for the application of FeRAM," *AIP Adv.* 6, 035128 (2016).
- [3.8] J. F. Ihlefeld, D. T. Harris, R. Keech, J. L. Jones, J.-P. Maria, and S. T. McKinstry, "Scaling effects in perovskite ferroelectrics: Fundamental limits and process structure property relations," *J. Am. Ceram. Soc.* 99, 2537–2557 (2016)
- [3.9] T. S. Böscke, J. Müller, D. Bräuhaus, U. Schröder, and U. Böttger, "Ferroelectricity in hafnium oxide thin films," *Appl. Phys. Lett.* 99, 102903 (2011).
- [3.10] H. K. Yoo, J. S. Kim, Z. Zhu, Y. S. Choi, A. Yoon, M. R. MacDonald, X. Lei, T. Y. Lee, D. Lee, S. C. Chae, J. Park, D. Hemker, J. G. Langan, Y. Nishi, and S. J. Hong, "Engineering of ferroelectric switching speed in Si doped HfO₂ for highspeed 1T-FERAM application," in *IEEE International Electron Device Meeting (IEDM)* (2017), pp. 481–486
- [3.11] T. Ali, P. Polakowski, S. Riedel, T. Büttner, T. Kämpfe, M. Rudolph, B. Pätzold, K. Seidel, D. Löhner, R. Hoffmann, M. Czernohorsky, K. Kühnel, P. Steinke, J. Calvo, K. Zimmermann, and J. Müller, "High endurance ferroelectric hafnium Oxide based FeFET memory without retention penalty," *IEEE Trans. Electron Devices* 65, 3769–3774 (2018).
- [3.12] S. Fichtner, N. Wolff, F. Lofink, L. Kienle, and B. Wagner, "AlScN: A III-V semiconductor based Ferroelectric," *J. Appl. Phys.* 125, 114103 (2019).

[3.13] S.-L. Tsai, T. Hoshii, H. Wakabayashi, K. Tsutsui, T.-K. Cung, E. Y. Chang, and K. Kakushima, “Room-temperature deposition of a poling-free ferroelectric AlScN film by reactive sputtering,” *Appl. Phys. Lett.* 118, 082902 (2021).

[3.14] S. Yasuoka, R. Mizutani, R. Ota, T. Shiraishi, T. Shimizu, S. Yasui, Y. Ehara, K. Nishida, M. Uehara, H. Yamada, M. Akiyama, Y. Imai, O. Sakata, H. Funakubo, “Enhancement of crystal anisotropy and ferroelectricity by decreasing thickness in (Al,Sc)N films,” *J. Cera. Soc. Jpn*, 130, 436 (2022)

[3.14] P. Wang, D. Wang, B. Wang, S. Mohanty, S. Diez, Y. Wu, Y. Sun, E. Ahmadi, and Z. Mia, “N-polar ScAlN and HEMTs grown by molecular beam epitaxy,” *Appl. Phys. Lett.*, 119, 082101 (2021)

ACKNOWLEDGMENTS

The authors would like to thank Prof. Nohira with Tokyo City University for the XPS measurements.

Chapter 4

Reliability and breakdown mechanism of ferroelectric AlScN films upon switching cycles

4.1 The Breakdown Mechanism of AlScN Film after Cycling

Test

The performance of ferroelectric FET is dominated by the characteristic of ferroelectric materials. HfO₂ is used to be used for the ferroelectric devices with the advantages of being compatible with the traditional CMOS fabrication processes and showing ferroelectric characteristics in a thickness of less than 10nm [4.1]. Ferroelectric FET arrays and nonvolatile memories are also demonstrated [4.2~4.5]. However, there are still some issues for HfO₂ to be solved.

One of the issues is the switching cycle. A typical endurance cycle for ferroelectric HfO₂ capacitor where a switching cycle of ten to the ninth is achieved [4.6, 4.7]. Although the switching cycle can be improved to some extent with the capping process or other element incorporation, the switching cycle needs to be improved. During the cycles, oxygen vacancies are formed and turned into a chain of oxygen vacancies which leads to a local current path between the electrodes [4.8~4.10]. Once the current path has low resistance, the excess Joule heat at the local conduction path will break the device. Besides, there are also wake-up effect and degradation issue which need to be solved.

A new ferroelectric material AlScN is found in 2019 [4.11]. AlScN shows an extremely large remanent polarization of about 100 $\mu\text{C}/\text{cm}^2$. A box profile in the PE curve of AlScN makes it attractive for memory devices. The large polarization originates from the wurtzite structure of the AlScN. The switching mechanism is explained by the movement of the nitrogen atoms. By controlling the content of Sc from 10% to 40%, the coercive field and bandgap could be adjusted which gives flexibility to memory design [4.12~4.15].

Figure 4.1 shows the typical aging effect observed in ferroelectric films. Wake-up: P_r increases at the early stage of switching cycles. Fatigue: P_r decreases with switching cycles by electron trapping. Breakdown: Dielectric breakdown after certain switching cycles.

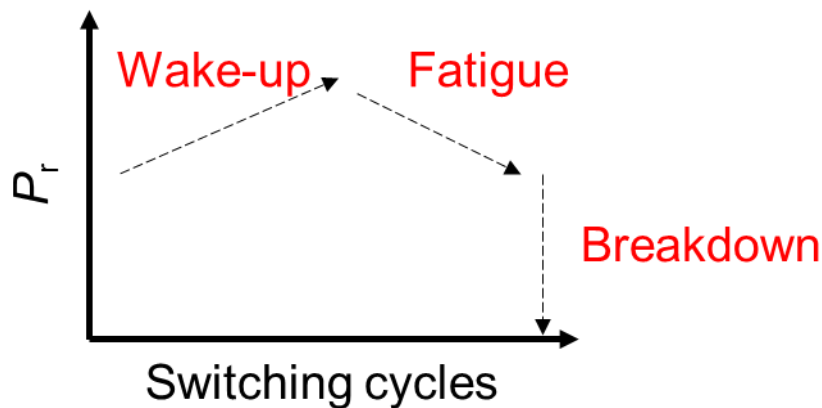


Figure 4.1 Typical aging effect observed in ferroelectric films.

In this chapter, the breakdown mechanism is evaluated by the leakage current measurement up to ten to the fifth cycles [4.16]. The purpose of this chapter is to create a model for the aging and breakdown of AlScN films. Figure 4.2 showed a model which separates AlScN films into two parts. The following experiments are about the interface change and bulk change of AlScN films.

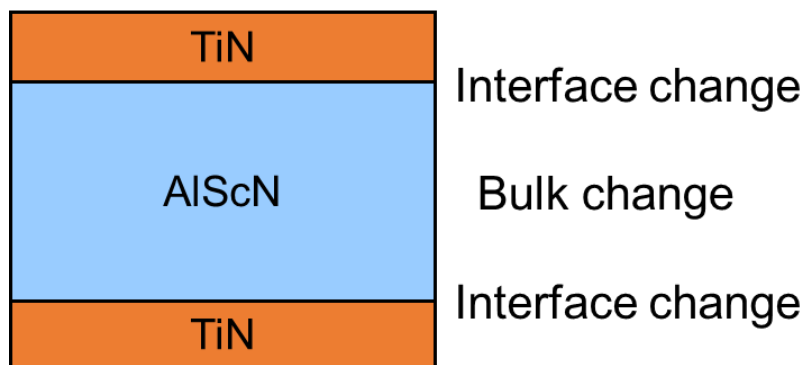


Figure 4.2 A model for the aging and breakdown of AlScN films.

4.2 Fabrication process of 400°C deposited AlScN Capacitors

A 50nm-thick ferroelectric AlScN film and both top and bottom TiN electrodes were deposited in the same chamber by reactive sputtering to become a sandwich structure. The top electrode was patterned by wet etching with the etchant ($\text{NH}_4\text{OH}:\text{H}_2\text{O}_2:\text{H}_2\text{O} = 1:5:5$) to form capacitors. The characteristic has already been researched in chapter 3. The remanent polarization is over $100 \mu\text{C}/\text{cm}^2$, and the coercive field is about 5.3 MV/cm. The breakdown field is about 8.1 MV/cm. A columnar structure is also confirmed by TEM and X-ray rocking curves.

4.3 Interface analysis method by analyzing leakage current

Figure 4.3 showed the interface analysis method which is held by analyzing leakage current [4.17]. The leakage current of the capacitor followed the Schottky emission model under different measuring temperatures.

Figure 4.4 showed the extracted Schottky barrier height and the extracted Richardson's constant from analysis. The extracted Schottky barrier height changed from 0.46eV to 0.36eV after the first switching. The extracted Richardson's constant was ten to the minus 7th, which is too small considering the electron mass of the AlScN layer.

The reason for the low extracted Schottky barrier height and low Richardson constant has been proposed which nitrogen vacancies occur at AlScN/ metal interface and shift the apparent Schottky barrier height. The nitrogen vacancies occur at the interface bending down the band and forming a tunneling barrier. Figure 4.5 showed the illustration. With a simple tunneling barrier, the transmission probability can be expressed with the equation in figure 4.6 [4.18].

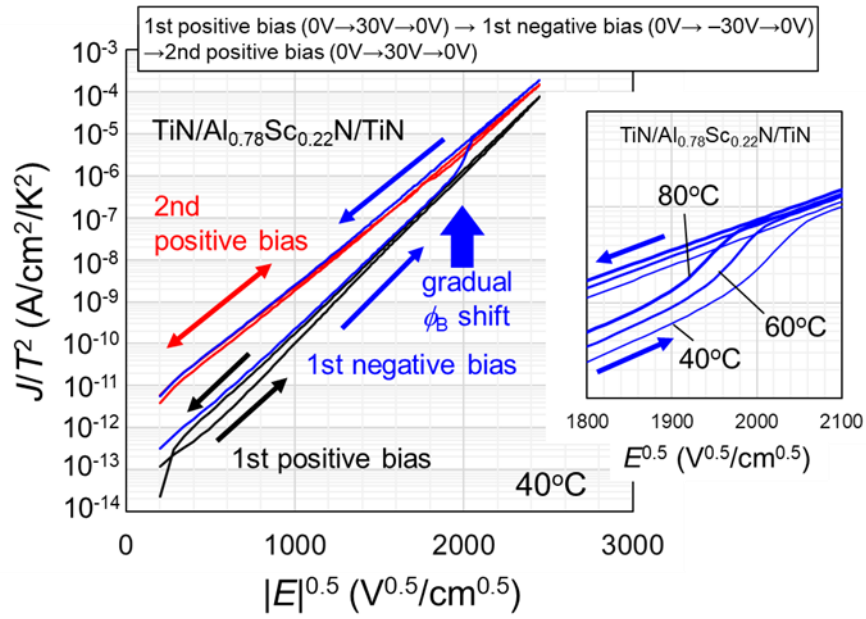


Figure 4.3 Interface analysis method is held by analyzing leakage current [4.17].

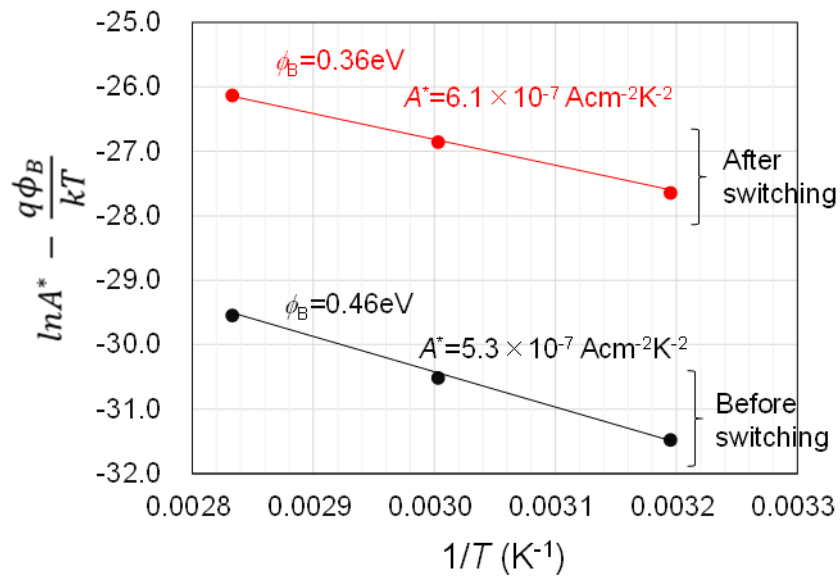


Figure 4.4 The extracted Schottky barrier height and the extracted Richardson's constant from analyzing [4.17].

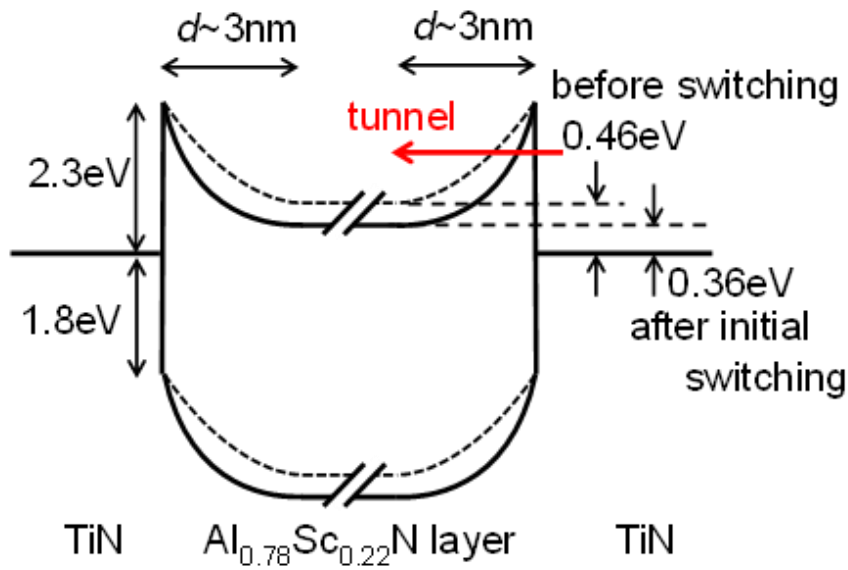


Figure 4.5 An illustration of which the nitrogen vacancies occur at the interface bending down the band and forming a tunneling barrier [4.17].

$$\ln\left(\frac{J}{T^2}\right) = \sqrt{\frac{q}{4\pi\epsilon_0\epsilon_i}} \frac{q}{kT} \sqrt{E} \left[\ln(A^*T_t) \right] - \frac{q\phi_{Bn}^{app}}{kT}$$

$$\ln(T_t) \approx -2d\sqrt{\frac{2m^*q\Delta\phi_{Bn}}{\hbar^2}}$$

assuming a rectangular tunnel barrier

m^* : effective electron mass \hbar : reduced Planks constant
 T_t : tunneling probability $\Delta\phi_{Bn}$: difference of ϕ_{Bn} and ϕ_{Bn}^{app}
 d : tunneling distance

J : current density
 k : Boltzman constant
 E : electric field in insulator
 ϵ_i : optical dielectric constant
 ϵ_0 : permittivity of free space
 A^* : effective Richardson constant
 T : absolute temperature
 q : elementary charge
 ϕ_{Bn}^{app} : apparent Schottky barrier height

T. J. Vink, J. Appl. Phys., 71, 4399 (1992)

Figure 4.6 The equations of the Schottky emission model and transmission probability [4.18].

4.4 Experiment results of 400°C deposited AlScN Capacitors after cycling tests

Figure 4.7 shows the C-V curves of different switching cycles from 0V to -28V. Switching was ended with positive bias; then CV measurement to a negative voltage. The device after 1 and 100 switching cycles showed little difference with a peak at -22V. With the switching cycles coming to 1000 times, the peak at -22V decreased, and the peak at -16V appeared. The reason that the capacitance of the device with 100000 switching cycles increase at -22V is the growing leakage current. The dissipation factor was more than 4 during the measurements at -22V. We already knew that the polar turned to what it was as deposition when we apply a positive voltage in chapter 3 of the poling-free experiments. The peak capacitance changed slightly when we apply the positive voltage indicating that a gradual transformation in the AlScN film upon switching reversal is happening only when the film is switched from an upward to a downward direction. The CV curves upon switching cycles showed a positive shift in the crossover capacitance between the forward and reverse sweepings indicating the presence of the imprint effect (electron trapping).

Thus, we think that the nitrogen vacancies may occur during the switching, facilitating the movement of N atoms to reduce the coercive field. One can understand that the transformation is completed during the C-V measurement for the fresh sample as the time for the measurement is long.

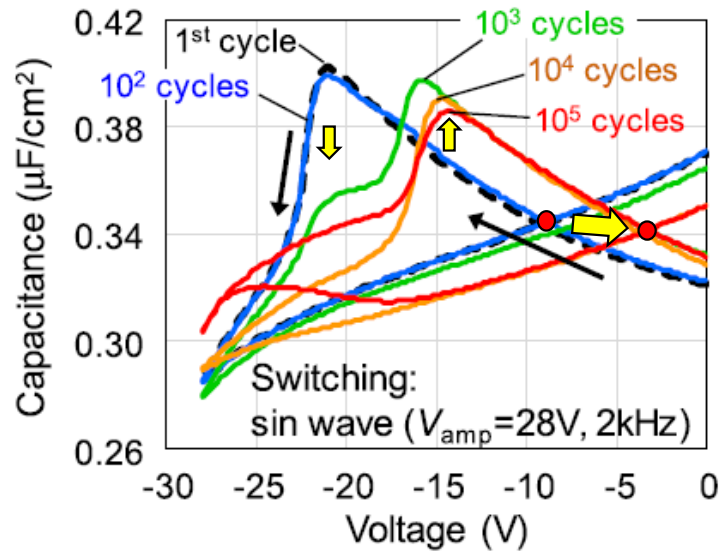


Figure 4.7 C-V curves of different switching cycles from 0V to -28V.

Figure 4.8 showed the remanent polarization upon switching cycles which showed a slight increase and then, decrease severely for lower applying voltage. The reason for increasing P_r might be the movements of E_c and the fatigue effect might be electron trapping.

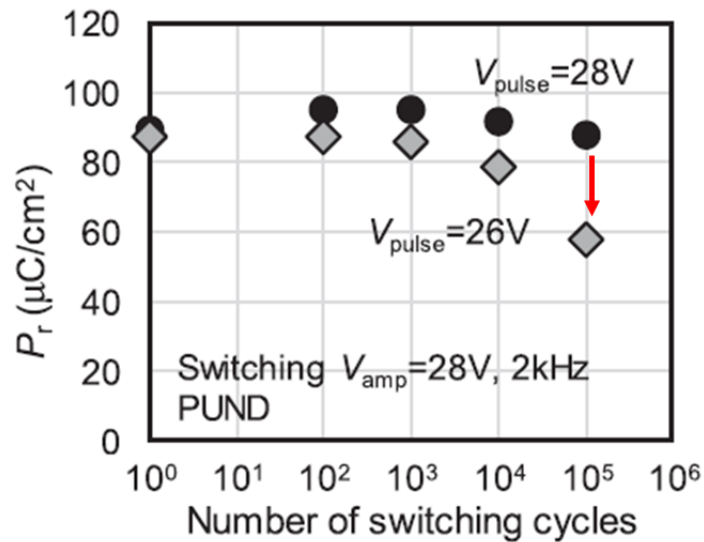


Figure 4.8 Remanent polarization upon switching cycles under different applied voltage.

The nitrogen vacancies have been researched which exist in the as-deposited state [4.17]. This research analyzed the leakage current to see what happened in the AlScN film during switching. We use the same method to see what happened before the device breakdown. Figure 4.9 shows the Schottky plot of the capacitors with different switching cycles. The leakage current was measured after the cycling test with a sin wave of 5.6MV/cm at 10kHz, up to ten to the fifth cycles. The leakage current also followed the Schottky emission model after the cycling test. The current increased first and then showed a reduction up to ten to the fifth cycle. The increase in leakage current is the formation of V_N , and the decrease in leakage current is due to the increasing tunneling distance.

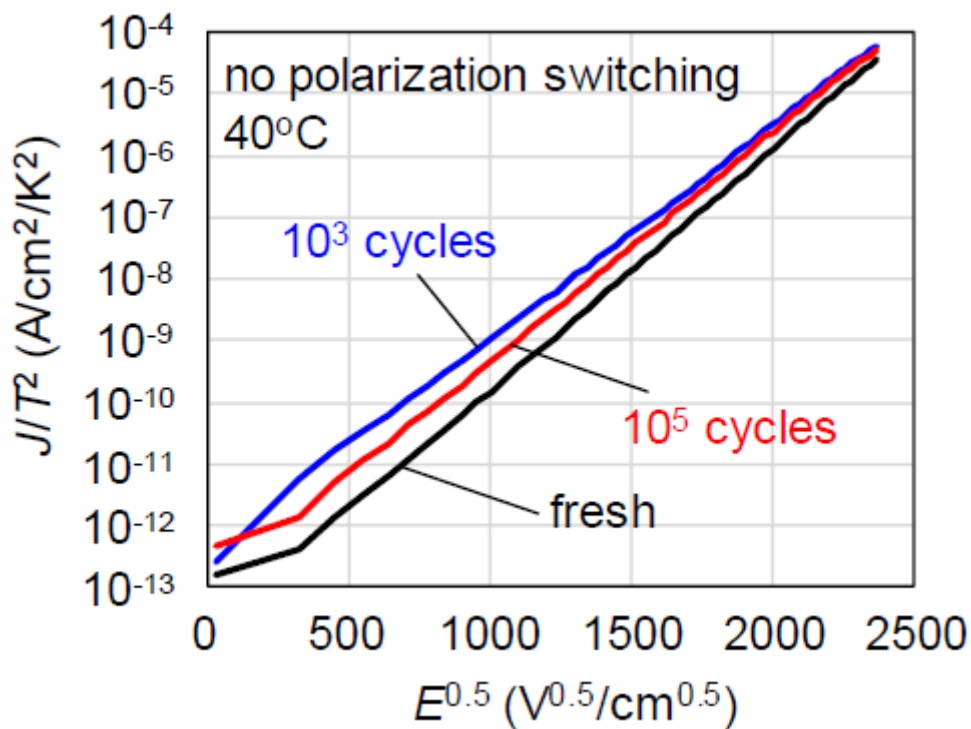


Figure 4.9 Schottky plot of the devices at fresh, and after switching cycle of 10^3 and 10^5 times.

The tunneling barrier exists as the appearance of nitrogen vacancies. The Schottky emission model with a tunneling barrier at the $\text{Al}_{0.78}\text{Sc}_{0.22}\text{N}$ /metal interface can be expressed as follows,

$$\ln\left(\frac{J}{T^2}\right) = \sqrt{\frac{q}{4\pi\epsilon_0\epsilon_i}} \frac{q}{kT} \sqrt{E} + \ln(A^*T_t) - \frac{q\phi_{\text{Bn,app}}}{kT}, \quad [4.18] \quad (1)$$

where E , T , q , k , ϵ_0 , ϵ_i , A^* , and $\phi_{\text{Bn,app}}$ are the electric field, absolute temperature, elementary charge, Boltzmann constant, vacuum permittivity, optical dielectric constant, effective Richardson constant, and apparent Schottky barrier height to electron, respectively. By introducing a rectangular shape tunneling barrier the tunneling probability (T_t), can be expressed as

$$\ln(T_t) = -2d\sqrt{\frac{2m^*q(\phi_{\text{Bn}} - \phi_{\text{Bn,app}})}{\hbar^2}}, \quad [4.18] \quad (2)$$

where m^* , \hbar , ϕ_{Bn} , d is the effective electron mass, reduced Planck constant, Schottky barrier height for an electron at $\text{Al}_{0.78}\text{Sc}_{0.22}\text{N}$ /metal interface and tunneling distance respectively.

Figure 4.10 shows the extracted optical dielectric constant under cycling tests. The optical dielectric constants were extracted from the slope of the Schottky plot, and it increased up to 1 thousand cycles and decreases back with further cycling tests. The increase can be explained by nitrogen-vacancy formation, and the reduction can be explained by the rearrangement of atoms near the interface. The optical dielectric constants are obtained at high frequencies. The electron transit time at the metal interface is shorter than the dielectric relaxation [4.19]. Thus, the optical dielectric constant is lower than the dielectric constant of AlScN .

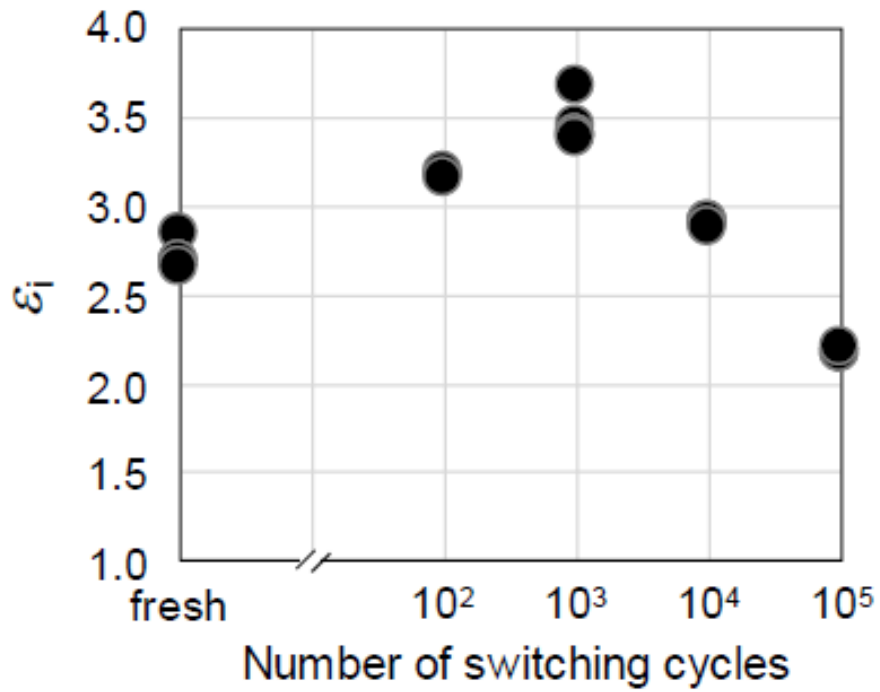


Figure 4.10 The extracted optical dielectric constant under cycling tests.

Figure 4.11 shows the extraction of the capacitors under cycling tests. The extracted Schottky barrier height shows a continuous reduction from 0.59eV to 0.27eV with switching cycles.

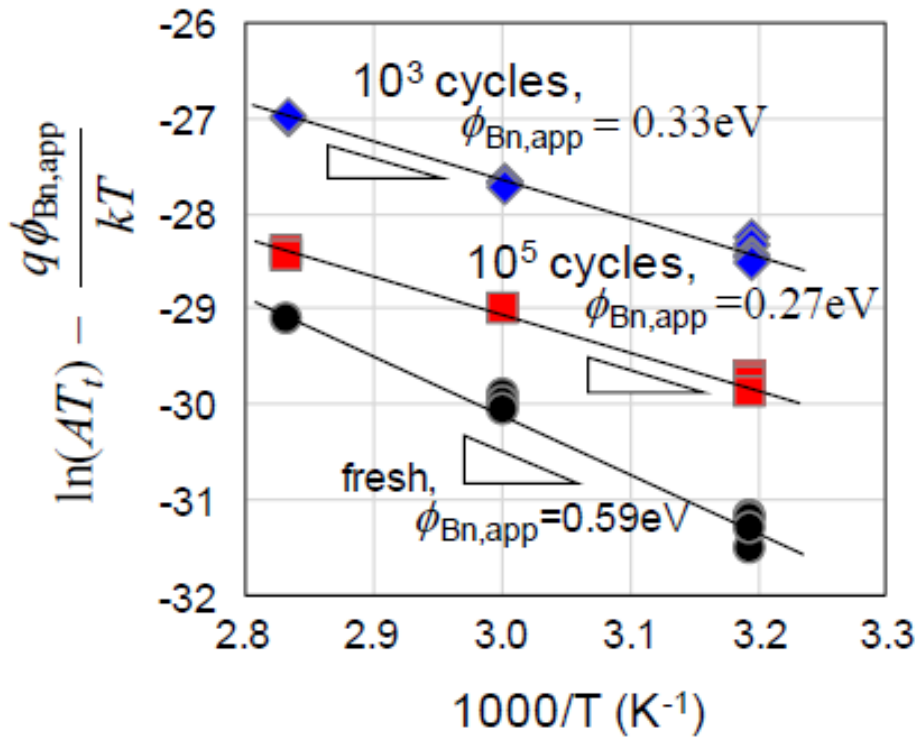


Figure 4.11 The Arrhenius plots of the capacitors under cycling tests.

The apparent Schottky barrier height is concluded in figure 4.12(a) which is continuously reduced with switching. The apparent Richardson constant can be extracted from the intercept of figure 4.11 and the results are shown in figure 4.12(a) which shows a linear relationship with cycles. The tunneling distance from the model was shown in figure 4.12 (c) and it increased from 4 nm to 6 nm with ten to the fifth switching cycle which means the downward bending in the interface of AlScN film becomes steeper with the switching cycles.

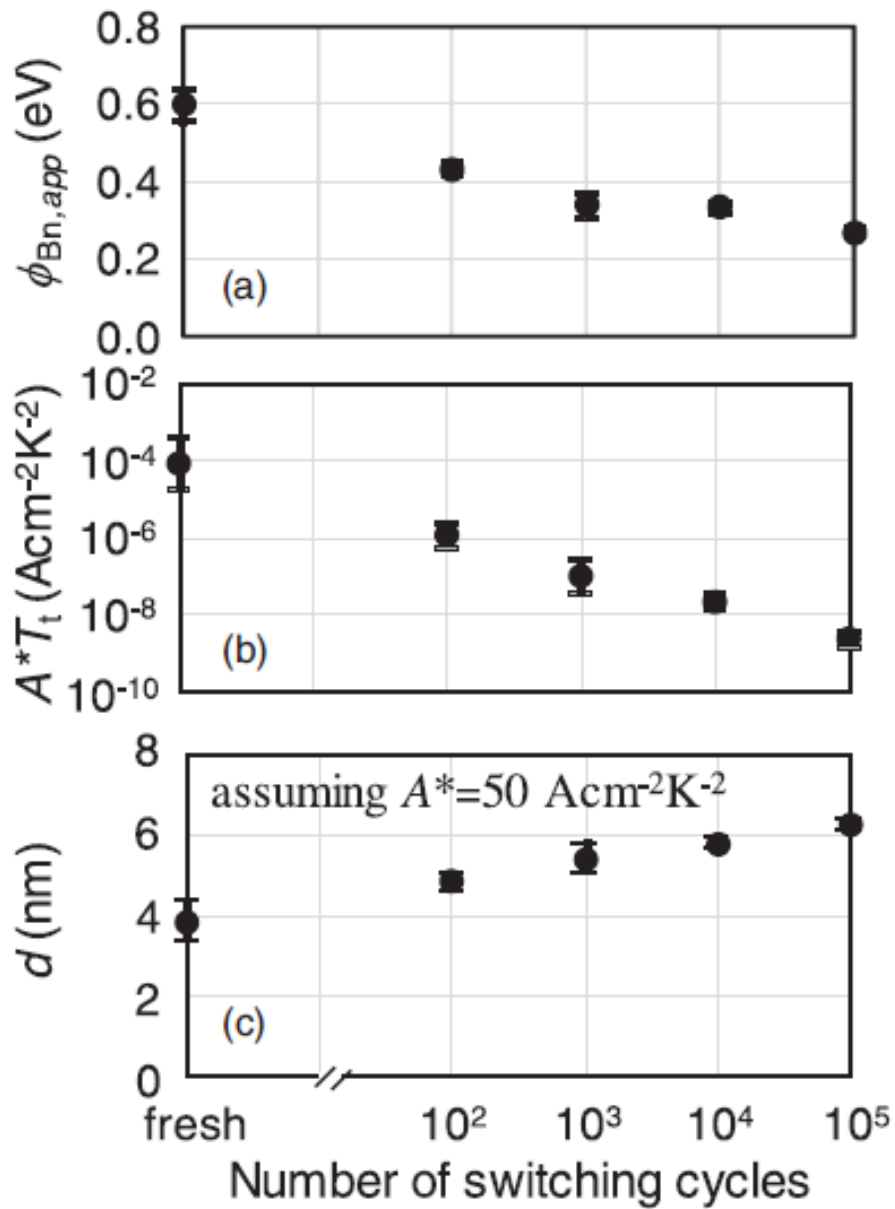


Figure 4.12 The extraction of the capacitors under cycling tests.

Based on the above results, figure 4.13 shows the physical phenomenon of the AlScN film with the switching cycles increased. Nitrogen vacancies exist in the interface in the beginning and are further increased during the switching. The nitrogen vacancies bend down the conduction band and increase the tunnel barrier. With the increase of the tunnel barrier, the apparent Schottky barrier height also decreases which leads to a higher

leakage current. Once the leakage current is over range and the device breakdown by excess Joule heat. Also, V_N are formed in the bulk AlScN which decrease E_c . And increase P_r

However, with more V_N occurring, the electron trapping in V_N reduce P_r .

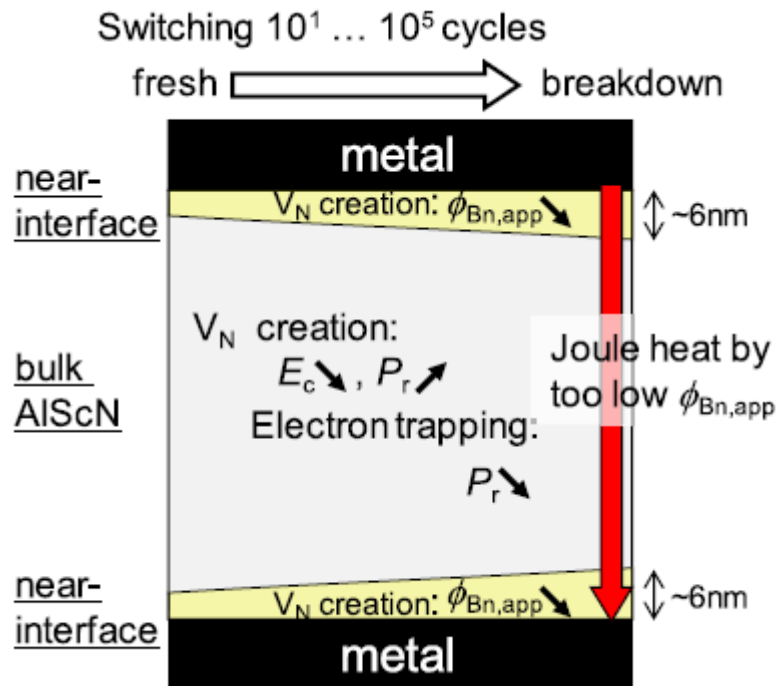


Figure 4.13 The illustration model of increasing nitrogen vacancies after the cycling test.

Table 4.1 and figure 4.14 show the comparison of the breakdown mechanism between different ferroelectric materials. The oxygen vacancy chain will form a conductive filament for oxide-based ferroelectric materials. The device breakdown due to the Joule heat at the bridged filament. On the other hand, the nitrogen-vacancy is created near the AlScN/metal interface to shift the effective Schottky barrier height. The

device breakdown due to the Joule heat by excess leakage current due to the small Schottky barrier height.

Table 4.1 Breakdown mechanism of different ferroelectric materials.

Material	Increase in leakage current along with switching cycles	Breakdown mechanism
PZT	V_O creation to form conductive filament (local conduction)	Joule heat by excess conduction at bridged filament
HfO ₂		
ASN	V_N creation near the ASN/metal interface to shift the f_{Bn}	Joule heat by excess leakage current

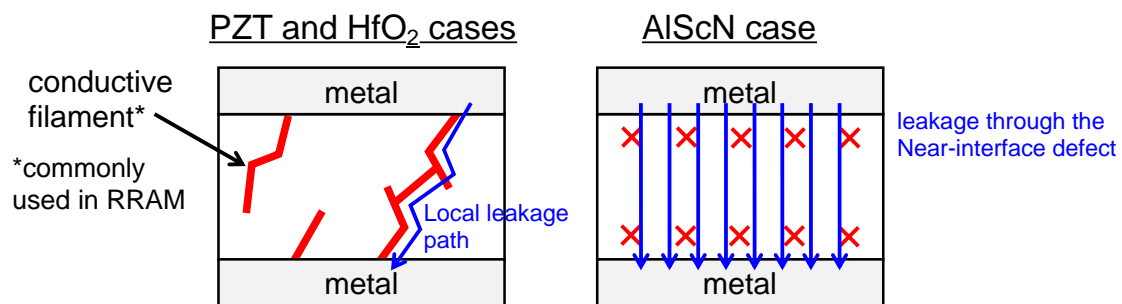


Figure 4.14 Breakdown mechanism of different ferroelectric materials.

4.5 Summary of this chapter

The purpose of this chapter is to create a model for the aging and breakdown of AlScN films upon switching cycles.

In conclusion, the near interface changes of AlScN and metal upon ferroelectric switching cycles are monitored by leakage current analysis. All the leakage currents before and after switching cycles followed the Schottky emission model, indicating that the local conduction path was hardly formed. Ferroelectric switching induces a band

bending at the interface to create a tunneling barrier, which eventually reduces the apparent Schottky barrier height. The apparent Schottky barrier height is reduced continuously with the switching cycle from 0.59eV to 0.27eV after 10^5 cycles. The breakdown of ferroelectric AlScN film triggered by the Joule heat due to excessive leakage current by reduced Schottky barrier height.

References

- [4.1] M. H. Park, T. Schenk, and U. Schroeder, *Ferroelectricity in Doped Hafnium Oxide: Materials, Properties and Devices* (Elsevier, Amsterdam, 2019), p. 49.
- [4.2] D. Reis, M. Niemier, and X. S. Hu, *Proc. Int. Symp. on Low Power Electronics and Design*, 2018, Vol. 24, p. 1.
- [4.3] K. Florent et al., “Vertical Ferroelectric HfO₂ FET based on 3-D NAND Architecture: Towards Dense Low-Power Memory,” *IEDM*, 2018, p. 43.
- [4.4] J. Okuno et al., *IEEE Symp. on VLSI Technology*, 2020, p. 1.
- [4.5] P. Polakowski, S. Riedel, W. Weinreich, M. Rudolf, J. Sundqvist, K. Seidel, and J. Muller, *IEEE 6th Int. Memory Workshop*, 2014, p. 1.
- [4.6] S. Li, *Adv. Electron. Mater.* 6, 2000264 (2020).
- [4.7] X. Tian, S. Shibayama, T. Nishimura, T. Yajima, S. Migita, and A. Toriumi, *Appl. Phys. Lett.* 112, 102902 (2018).
- [4.8] A. S. Sokolov, *Appl. Surf. Sci.* 434, 822 (2018).
- [4.9] B. Magyari-Köpe and Y. Nishi (ed.) *Advances in Nonvolatile Memory and Storage Technology* (Woodhead Publishing, Sawston, 2019).

- [4.10] C. Liu, Q. Wang, W. Yang, T. Cao, L. Chen, M. Li, F. Liu, D. K. Loke, J. Kang, and Y. Zhu, IEDM, 2021, p. 166.
- [4.11] S. Fichtner, N. Wolff, F. Lofink, L. Kienle, and B. Wagner, J. Appl. Phys. 125, 114103 (2019).
- [4.12] S. Yasuoka, J. Appl. Phys. 128, 114103 (2020).
- [4.13] R. Deng, S. R. Evans, and D. Gall, Appl. Phys. Lett. 102, 112103 (2013).
- [4.14] T. Mikolajick, S. Slesazeck, H. Mulaosmanovic, M. H. Park, S. Fichtner, P. D. Lomenzo, M. Hoffmann, and U. Schroeder, J. Appl. Phys. 129, 100901 (2021).
- [4.15] X. Liu, J. Zheng, D. Wang, P. Musavigharavi, E. A. Stach, R. Olsson III, and D. Jariwala, Appl. Phys. Lett. 118, 202901 (2021).
- [4.16] Sung-Lin Tsai, Takuya Hoshii, Hitoshi Wakabayashi, Kazuo Tsutsui, Tien-Kan Chung, Edward Yi Chang, Kuniyuki Kakushima, "Field cycling behavior and breakdown mechanism of ferroelectric $\text{Al}_{0.78}\text{Sc}_{0.22}\text{N}$ films," Japanese Journal of Applied Physics, Vol. 61, SJ1005, 2022
- [4.17] J. Kataoka, S. Tsai, T. Hoshii, H. Wakabayashi, K. Tsutsui, and K. Kakushima, Jpn. J. Appl. Phys. 60, 030907 (2021).
- [4.18] T. J. Vink, K. J. B. M. Nieuwesteeg, and G. Oversluizen, J. Appl. Phys. 71, 4399 (1992).
- [4.19] H. W. Chen, F. C. Chiu, C. H. Liu, S. Y. Chen, H. S. Huang, P. C. Juan, and H. L. Hwang, Appl. Surf. Sci. 254, 6112 (2008).

Chapter 5

Thickness Scaling in Ferroelectric AlScN Films

5.1 AlScN capacitors with Thickness Scaling

Thickness scaling is important for memory applications. The thickness scaling of DRAM faced the limit of the signal. The signal is too small to detect. Ferroelectric memory also faces the same problem. PZT reached its limit of about 100 nm thick. PZT will lose its ferroelectricity under this thickness [5.1~5.4]. A new ferroelectric material HfO₂ has been researched for the next generation of ferroelectric memory. HfO₂ keeps its ferroelectricity even under 10 nm thick [5.5, 5.6]. However, HfO₂ still has several issues to be solved such as the wake-up effect and degradation issues. Another new ferroelectric material, AlScN, was found in 2019 [5.7]. The remanent polarization is extremely large about 100 $\mu\text{C}/\text{cm}^2$ which is large enough to be expected for thin memory applications. The wurtzite-type structure for AlScN also made it to be stable to deposit [5.8].

Although there is plenty of advantages to applying AlScN, there are only a few reports of thickness scaling. Figure 5.1 showed thickness scaling on remanent polarization for AlScN films. Well-saturated remanent polarization was shown at room temperature measurement for 20-nm-thick AlScN films and was shown at high temperature (150°C) measurement for 12-nm-thick AlScN films [5.9]. Also, P_r is reported to decrease along with thickness scaling. Figure 5.2 showed thickness scaling on XRD for AlScN films [5.10]. The XRD along with thickness scaling was also reported. 002 peak of AlScN disappears when scaling to 23 nm.

The purpose of this chapter is to create a model to explain the change in P_r upon thickness scaling [5.11, 5.12].

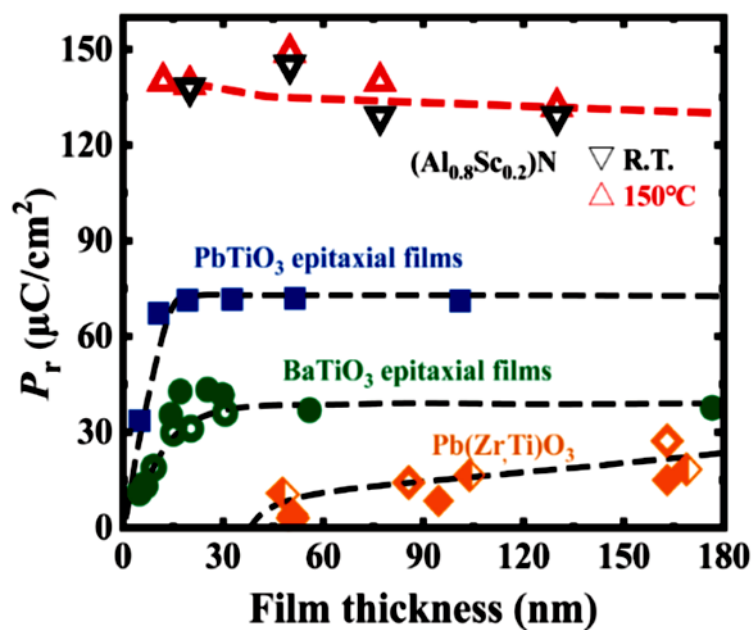


Figure 5.1 Thickness scaling on remanent polarization for AlScN films [5.9].

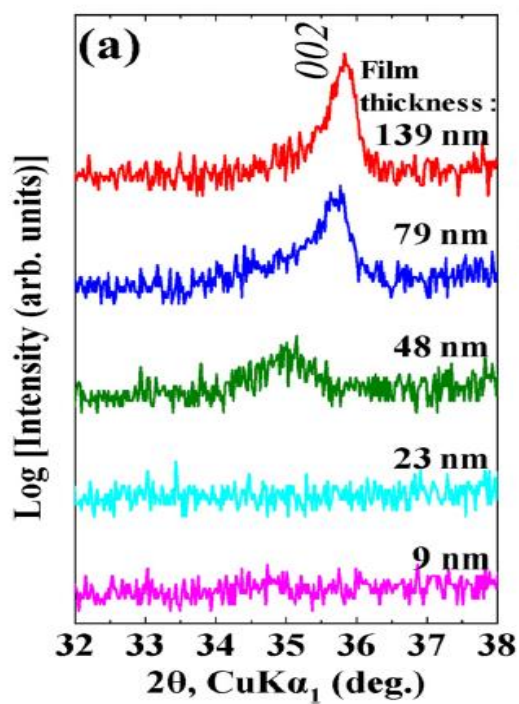


Figure 5.2 Thickness scaling on XRD for AlScN films [5.10].

5.2 Fabrication process of AlScN capacitors with thickness

Scaling

The fabrication process is almost the same as the device in chapters 3 and 4. First, a TiN bottom electrode was sputter-deposited on a chemical-cleaned n⁺Si. Then, an Al_{0.8}Sc_{0.2}N film was DC sputter-deposited from an Al_{0.57}Sc_{0.43} target with Ar and N₂ mixture in the same chamber with different thicknesses ranging from 20 to 50 nm. Another TiN layer was deposited onto the Al_{0.8}Sc_{0.2}N film. All the deposition process temperature was kept constant at 400°C. The top TiN layer was patterned by wet etching to form electrodes.

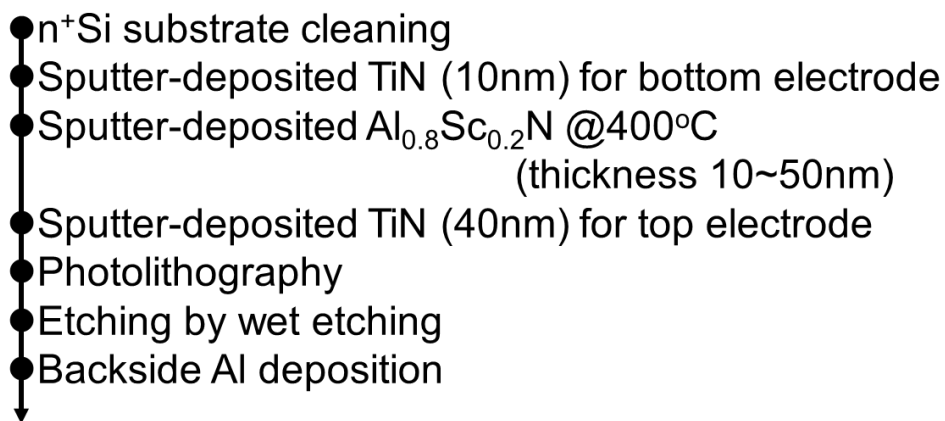


Figure 5.3 Fabrication process flow of AlScN MIM capacitor.

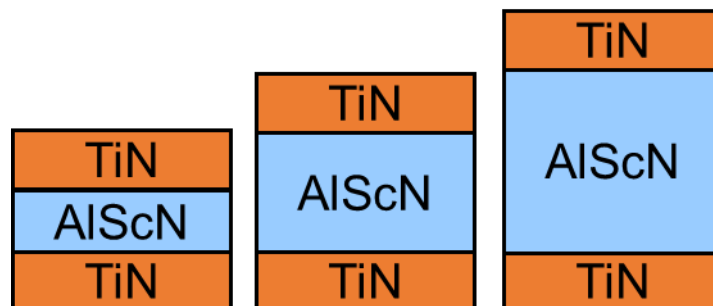


Figure 5.4 Schematic illustrations of the fabricated AlScN MIM capacitor.

5.3 Experiment results of AlScN capacitors with thickness

Scaling

Figure 5.5 shows the out-of-plane XRD curves with different thicknesses of $\text{Al}_{0.8}\text{Sc}_{0.2}\text{N}$ films. All the curves show (002) plane signal of AlScN indicating the film keeps wurtzite crystal structure even with the thickness scaling down to 10 nm.

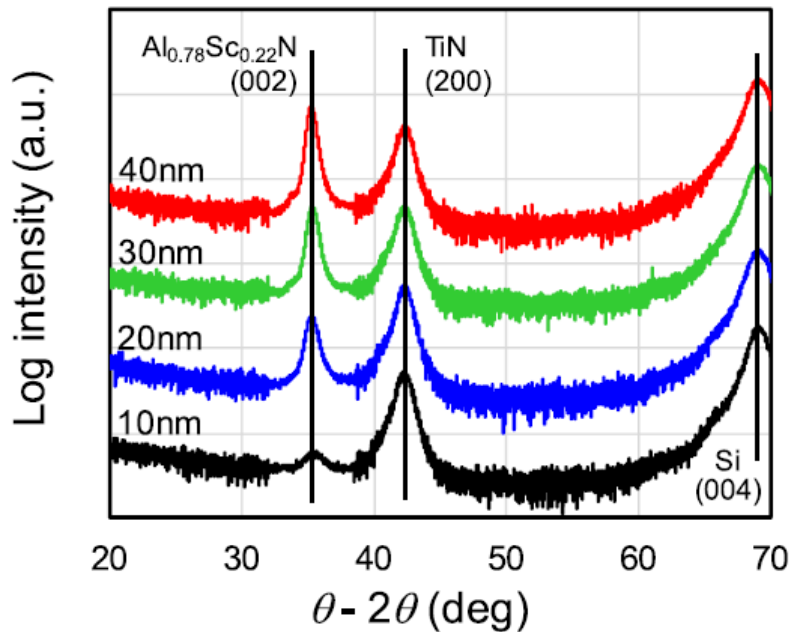


Figure 5.5 Out-of-plane XRD curves with different thicknesses of $\text{Al}_{0.8}\text{Sc}_{0.2}\text{N}$ films.

Figure 5.6 shows the rocking curves of (002) plane with different thicknesses of $\text{Al}_{0.8}\text{Sc}_{0.2}\text{N}$ films. The presence of the (002) peak shown in the rocking curve spectra suggests the formation of a c-axis-aligned $\text{Al}_{0.8}\text{Sc}_{0.2}\text{N}$ film. Besides, the (002) oriented films were obtained even with a thickness of 10 nm. The rocking curve analysis results are shown in Figure 5.7. The FWHM increases rapidly with a thickness of 10nm. The results also show that the minimum thickness of an AlScN single crystal is about 6 nm.

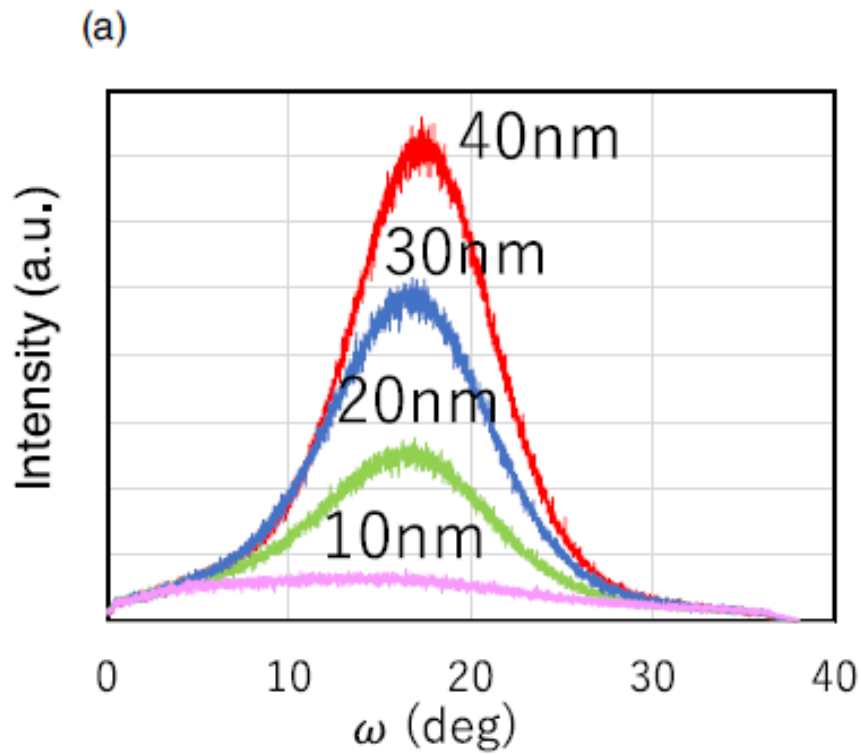


Figure 5.6 Rocking curves of (002) plane with different thicknesses of $\text{Al}_{0.8}\text{Sc}_{0.2}\text{N}$ films.

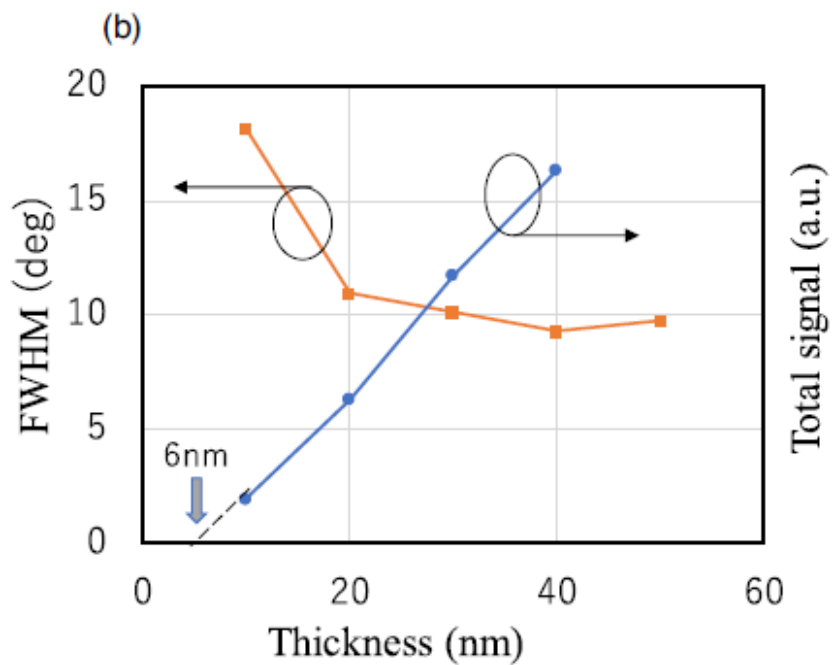


Figure 5.7 Rocking curves analysis results of (002) plane with different thicknesses of $\text{Al}_{0.8}\text{Sc}_{0.2}\text{N}$ films.

The leakage current with different thicknesses is shown in figure 5.8(a). The leakage current show little variation with thickness scaling. Relatively high leakage current is due to a small Schottky barrier height at the TiN/ $\text{Al}_{0.8}\text{Sc}_{0.2}\text{N}$ interface [5.13]. Figure 5.8(b) showed that the breakdown field is independent of thickness scaling. The breakdown field was maintained at about 4.5 MV/cm.

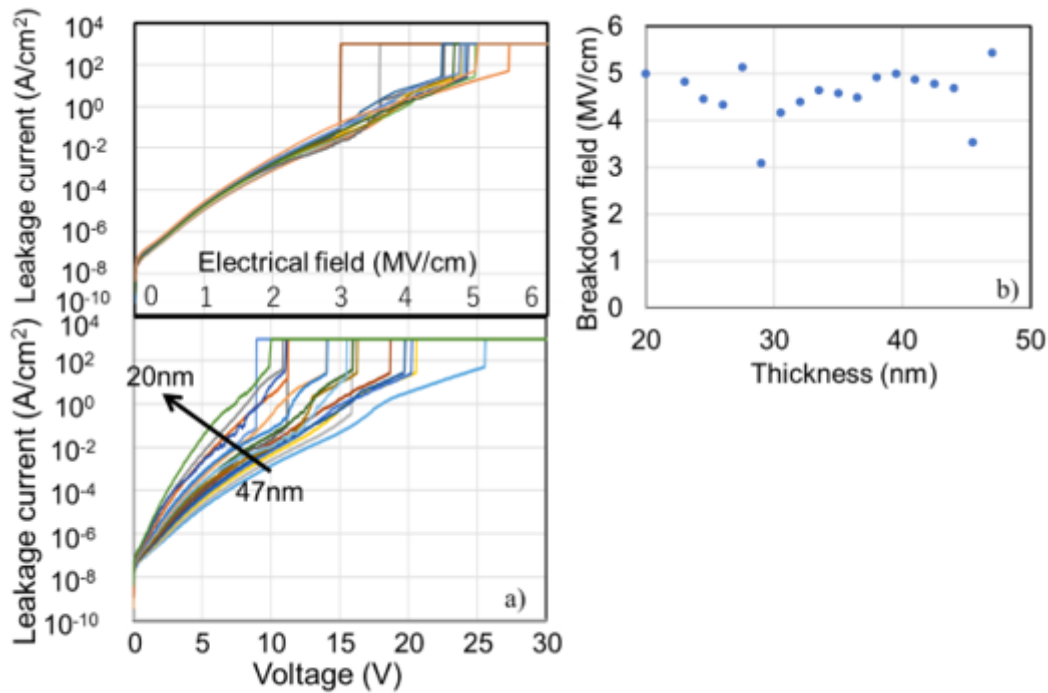


Figure 5.8 Leakage current measurements with different thicknesses of $\text{Al}_{0.8}\text{Sc}_{0.2}\text{N}$ MIM capacitors.

Figure 5.9 shows the capacitance-voltage (CV) curves measured at 100 kHz of the $\text{Al}_{0.8}\text{Sc}_{0.2}\text{N}$ ferroelectric capacitors with various thicknesses. Ferroelectric-type hysteresis is observed from all the CV curves with different thicknesses. The result suggests that $\text{Al}_{0.8}\text{Sc}_{0.2}\text{N}$ films do not lose the ferroelectricity with scaling down to 20 nm.

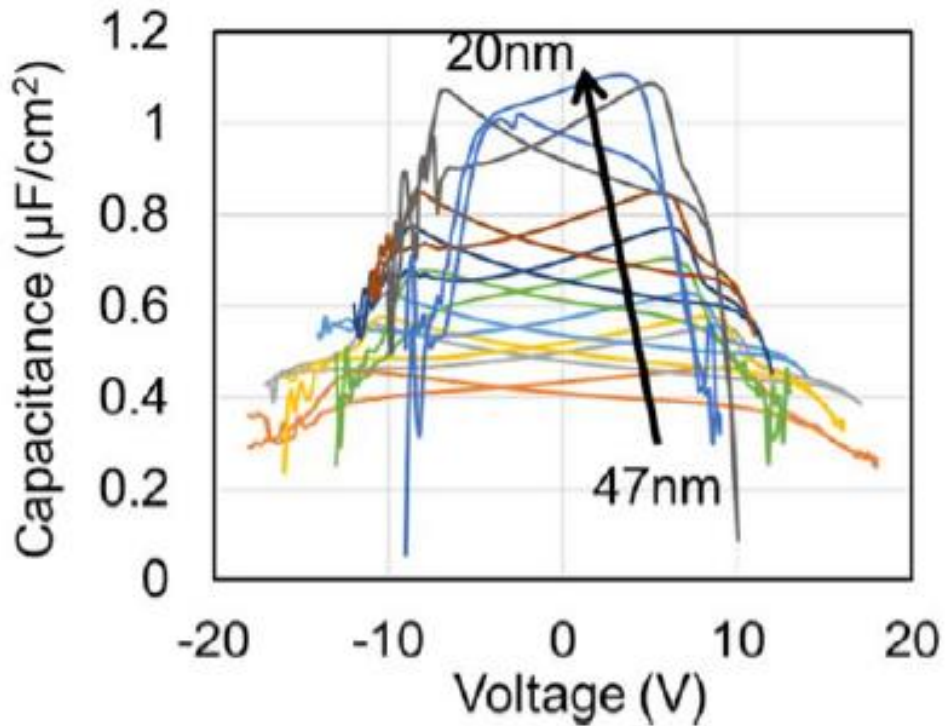


Figure 5.9 CV measurements with different thicknesses of Al_{0.8}Sc_{0.2}N MIM capacitors.

The tri-PUND polarization-voltage (PV) measurement results measured at 10kHz with an electrical field of 6.4MV/cm are shown in figure 5.10. The remanent polarization started to decrease from the film thickness of 30 nm. The reason is considered to be stress in AlScN films which makes the coercive field increase with the thickness decrease.

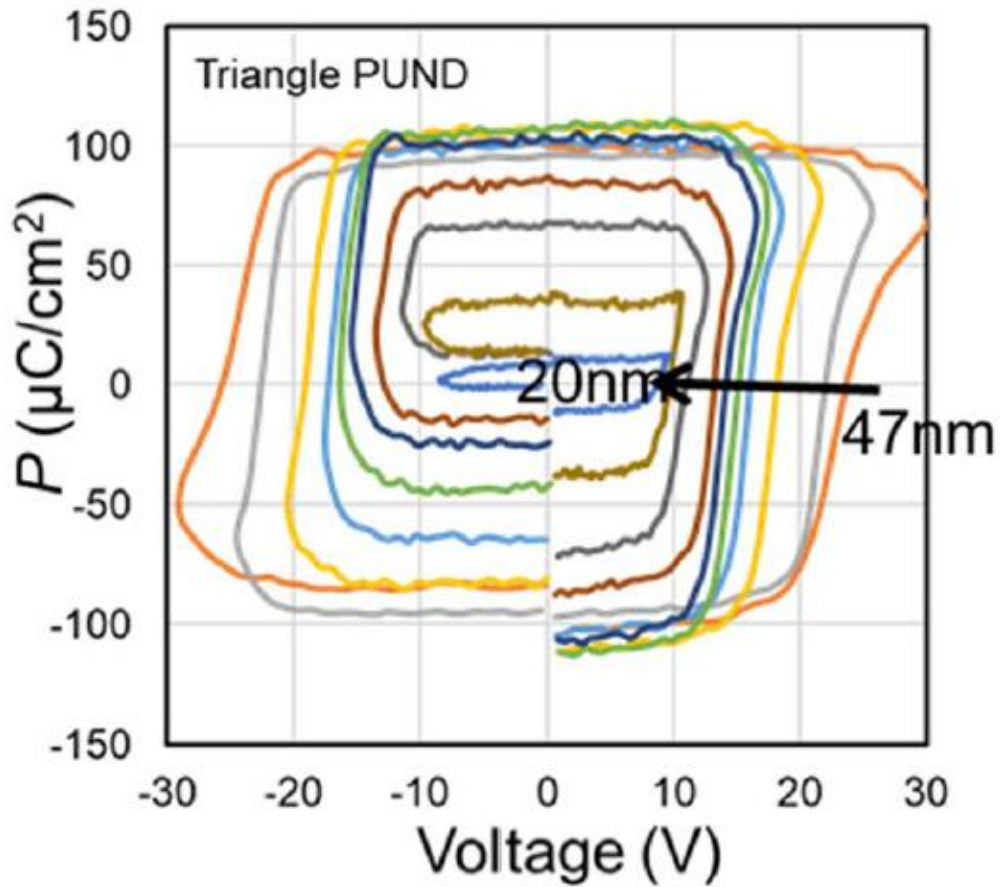


Figure 5.10 Tri-PUND measurements with different thicknesses of $\text{Al}_{0.8}\text{Sc}_{0.2}\text{N}$ MIM capacitors.

The remanent polarization was measured by square PUND measurements with different thicknesses as shown in figure 5.11. The magnitude of 5 MV/cm electric field and the pulse width of $5\mu\text{s}$ were applied to different thicknesses. We can see a reduction in remanent polarization below 35nm. This result agreed with the X-ray rocking curves analysis which shows an obvious reduction in FWHM under 30 nm. The reason may be worse oriented-growth in AlScN.

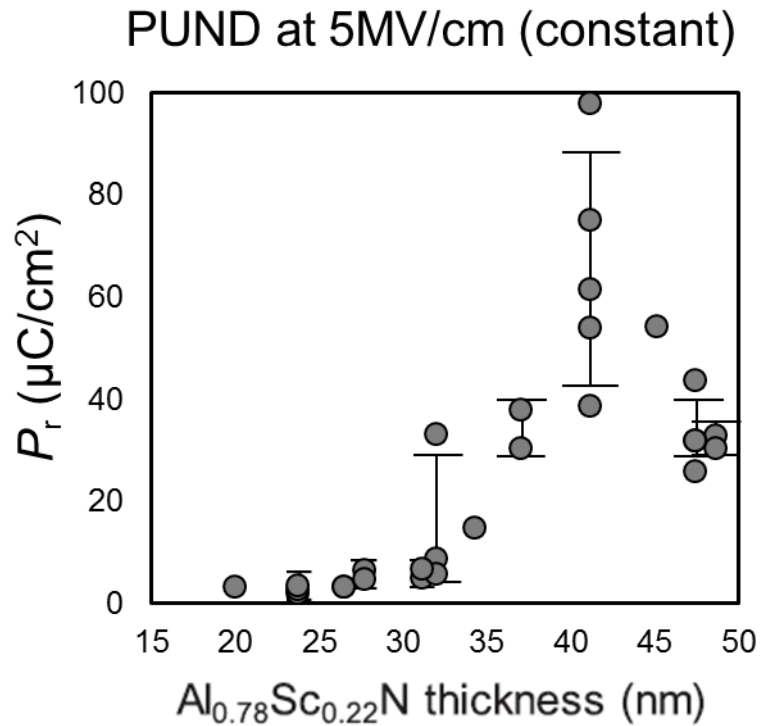


Figure 5.11 PUND measurements with different thicknesses of Al_{0.8}Sc_{0.2}N MIM capacitors.

The CV measurements in figures 5.12 and 5.13 showed the poling-free behavior with different thicknesses. If we apply the positive voltage at first, Al_{0.8}Sc_{0.2}N will maintain at the same polar until applying the negative voltage. On the contrary, if we apply the negative voltage first, Al_{0.8}Sc_{0.2}N will switch the polar at the beginning. The poling-free behavior means the device doesn't need to be poled thousand times to show hysteresis. It possesses the polar as it was deposited. The poling-free behavior was obtained even at the thickness of 20 nm.

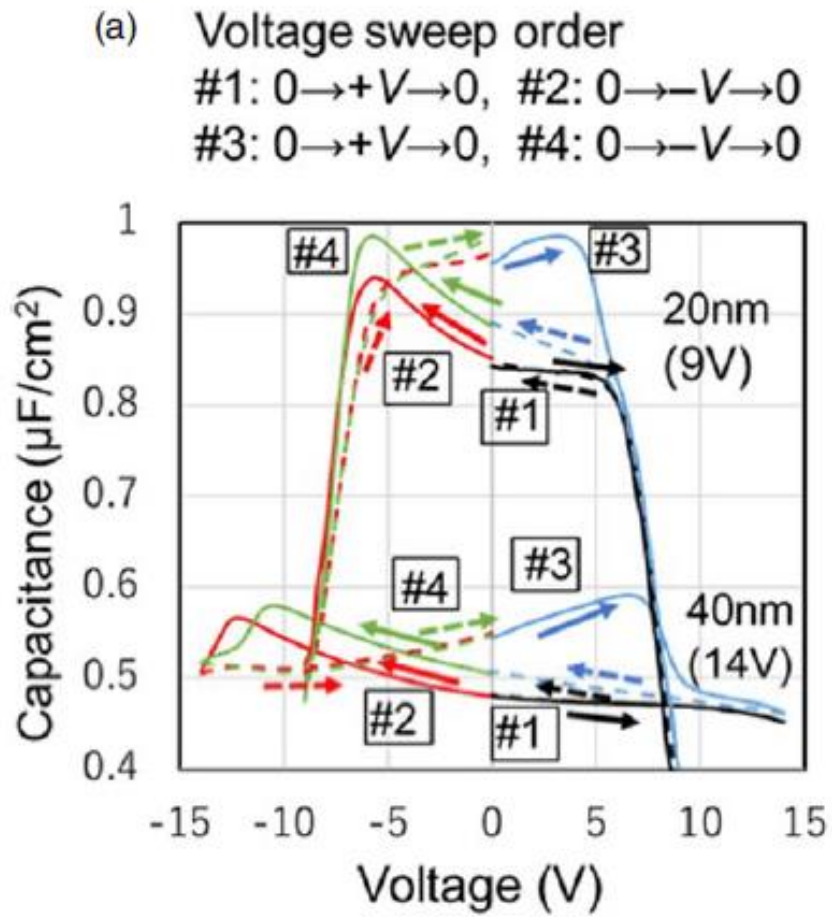


Figure 5.12 CV measurements of applying positive voltage first with different thicknesses of $\text{Al}_{0.8}\text{Sc}_{0.2}\text{N}$ MIM capacitors.

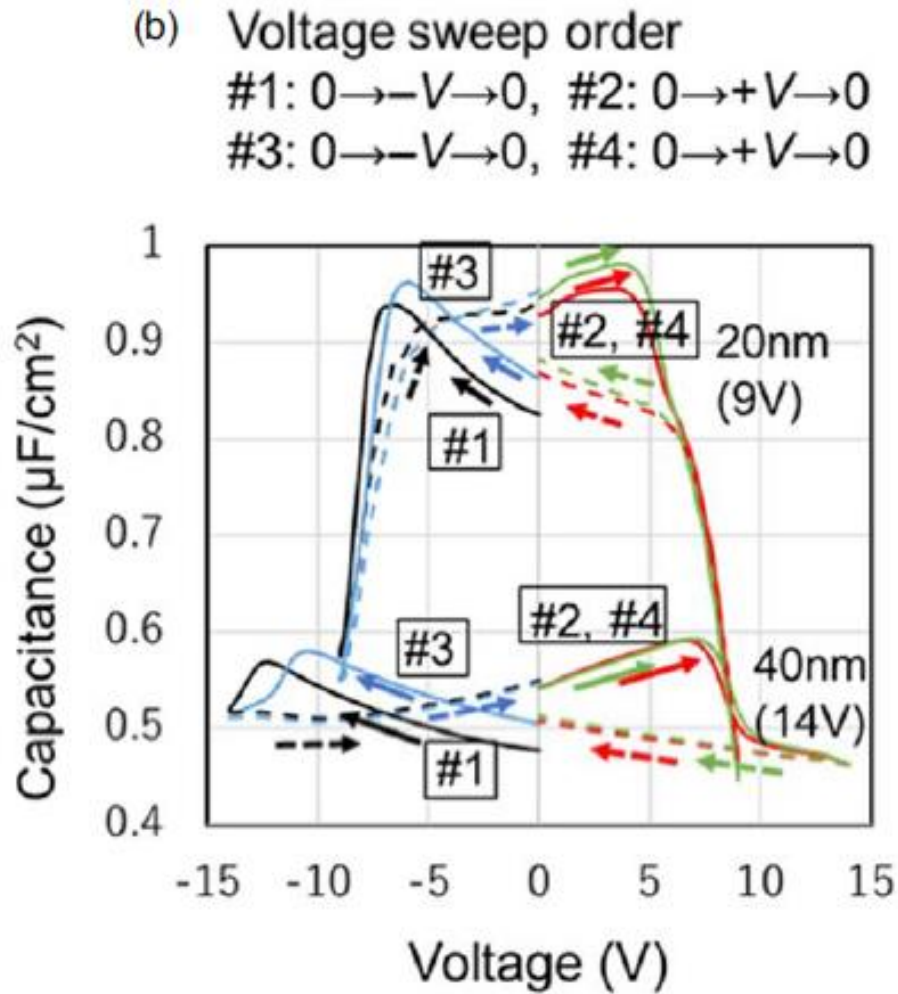


Figure 5.13 CV measurements of applying negative voltage first with different thicknesses of $\text{Al}_{0.8}\text{Sc}_{0.2}\text{N}$ MIM capacitors.

The endurance tests are measured with the pulses of 4.5 MV cm^{-1} at 100 kHz in different thicknesses as shown in figure 5.14. The wake-up effect is observed for all AlScN films. The wake-up effect becomes weaker for the thinner films. The mechanism of the ferroelectric switching in AlScN film is the movement of N atoms. As chapter 4 described, the nitrogen vacancies increase during the switching. The movement of N atoms becomes easier due to the increasing nitrogen vacancies. Thus, the remanent polarization becomes higher simultaneously. Furthermore, the switching cycles are no

longer than 10^5 times with a thickness thicker than 30 nm. The switching cycles increase at the cost of the remanent polarization.

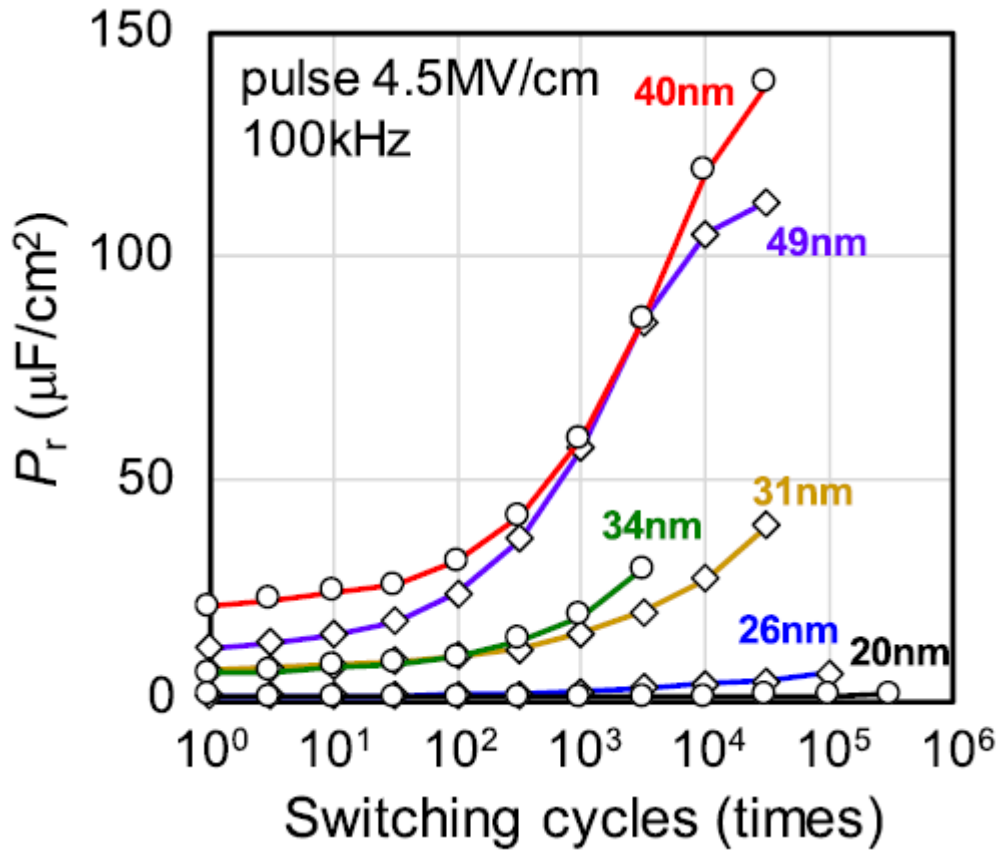


Figure 5.14 Fatigue tests of AlScN MIM capacitor in various thicknesses for remanent polarization.

Figure 5.15 show the current measured from PUND measurements with different switching cycles. The thick lines represent the current of the switching signal and the thin lines represent the current of the non-switching signal. The current increase with the switching cycles increases. We can also see the current accompanied by some delay signals which means the non-switched parts of AlScN begin to switch.

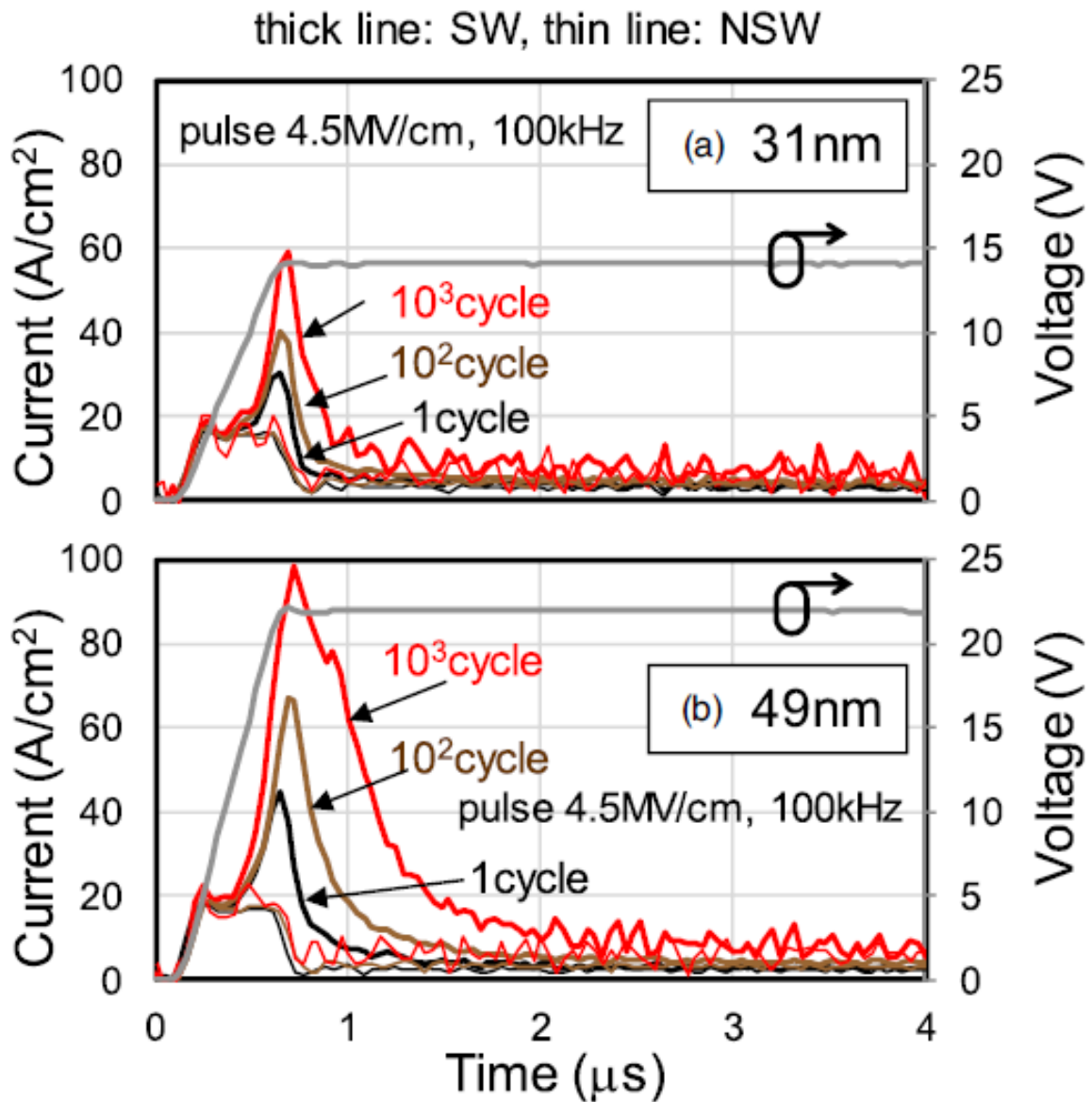


Figure 5.15 Fatigue tests of AlScN MIM capacitor in various thicknesses for remanent polarization.

Figure 5.16 shows a thickness scaling model to explain why E_c increases with thickness scaling down [5.14]. There are mismatches at the beginning of AlScN formation and strain remains at this region with a high c/a ratio and high E_c . With the columnar growth, AlScN relaxes. Strain exists at AlScN/bottom electrode has been reported. Also,

the non-switching region has been confirmed by TEM [5.15]. A layer with strain between AlScN and the bottom electrode induces high E_c . The influence of the layer with strain (high E_c) can be neglected for thick AlScN films. However, with thickness scaling down, the influence of the high E_c layer with strain start to appear which increases E_c .

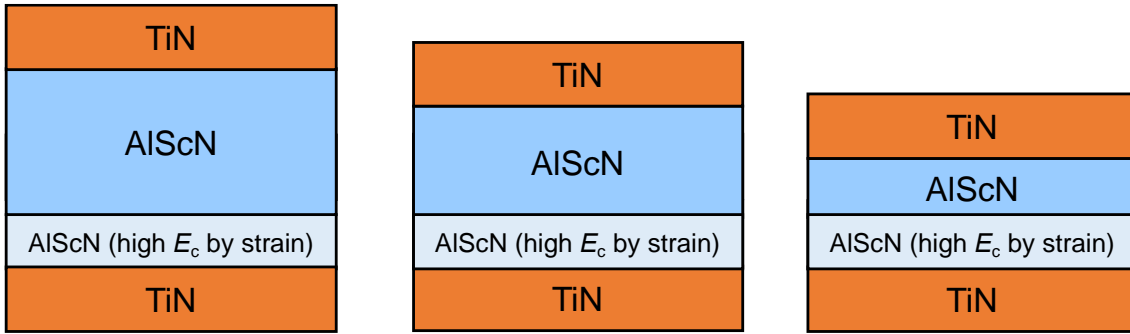


Figure 5.16 A thickness scaling model.

5.4 Summary of this chapter

The purpose of this chapter is to create a model to explain the change in P_r upon thickness scaling

The c-axis oriented growth of $Al_{0.8}Sc_{0.2}N$ was confirmed even with a thickness of 10 nm. Although the PV curves show degradation when the thickness is less than 30 nm, hysteresis-like CV curves were obtained with all the film thickness. Reduction in P_r measured at 5 MV/cm for thin layers was observed, suggesting the increase in E_c . The poling-free behavior was even obtained with a thickness of 20 nm. The endurance test showed the switching cycles increase at the cost of the remanent polarization. The current increase with the switching cycles increases which is agreed with chapter 4.

References

- [5.1] J. F. Ihlefeld, D. T. Harris, R. Keech, J. L. Jones, J. P. Maria, and S. Trolier-McKinstry, "Scaling effects in perovskite ferroelectrics: fundamental limits and process-structure-property relations," *J. Am. Ceram. Soc.* 99, 2537 (2016).
- [5.2] F. Chu, G. Fox, and T. Davenport, "High endurance scaled plzt thin films for FRAM applications," *Integr. Ferroelectr.* 36, 43 (2001).
- [5.3] K. Kim and S. Lee, "Integration of lead zirconium titanate thin films for high density ferroelectric random-access memory," *J. Appl. Phys.* 100, 051604 (2006).
- [5.4] F. P. G. Fengler et al., "Comparison of hafnia and PZT based ferroelectrics for future nonvolatile FRAM applications," 2016 46th European Solid-State Device Research Conf. (ESSDERC), 2016 (Lausanne), p. 369.
- [5.5] T. S. Boscke, J. Muller, D. Brauhaus, U. Schroder, and U. Bottger, "Ferroelectricity in hafnium oxide thin films," *Appl. Phys. Lett.* 99, 102903 (2011).
- [5.6] X. Tian, S. Shibayama, T. Nishimura, T. Yajima, S. Migita, and A. Toriumi, "Evolution of ferroelectric HfO₂ in ultrathin region down to 3 nm," *Appl. Phys. Lett.* 112, 102902 (2018).
- [5.7] S. Fichtner, N. Wolff, F. Lofink, L. Kienle, and B. Wagner, "AlScN: A III–V semiconductor-based ferroelectric," *J. Appl. Phys.* 125, 114103 (2019).
- [5.8] S. Fichtner, N. Wolff, G. Krishnamurthy, A. Petraru, S. Bohse, F. Lofink, S. Chemnitz, H. Kohlstedt, L. Kienle, and B. Wagner, "Identifying and overcoming the interface originating c-axis instability in highly Sc enhanced AlN for piezoelectric microelectromechanical systems," *J. Appl. Phys.* 122, 35301 (2017).
- [5.9] S. Yasuoka, R. Mizutani, R. Ota, T. Shiraishi, T. Shimizu, S. Yasui, Y. Ehara, K. Nishida, M. Uehara, H. Yamada, M. Akiyama, Y. Imai, O. Sakata, H. Funakubo,

- “Enhancement of crystal anisotropy and ferroelectricity by decreasing thickness in (Al,Sc)N films,” *J. Cera. Soc. Jpn*, 130, 436 (2022)
- [5.10] S. Yasuoka, *J. Appl. Phys.*, 128, 114103 (2020)
- [5.11] S.-L. Tsai, T. Hoshii, H. Wakabayashi, K. Tsutsui, and K. Kakushima, “Thickness scaling on ferroelectric Al_{0.8}Sc_{0.2}N Films,” *Ext. Abstr. of the Int. Conf. on Solid State Devices and Materials*, 2020, p. A-1-05.
- [5.12] S. Tsai, T. Hoshii, H. Wakabayashi, K. Tsutsui, T. K. Chung, E. Y. Chang, and K. Kakushima, *Jpn. J. Appl. Phys.* 60, SBBA05 (2021).
- [5.13] J. Katoaka, S.-L. Tsai, T. Hoshii, H. Wakabayashi, K. Tsutsui, and K. Kakushima, “A possible origin of the large leakage current in ferroelectric Al_{1-x}Sc_xN,” *Jpn. J. Appl. Phys.* 60, 03907 (2021).
- [5.14] E. Österlund, *Phys. Rev. Mat.*, 5, 035001 (2021)
- [5.15] N. Wolff et al., “Atomic scale confirmation of ferroelectric polarization inversion in wurtzite-type AlScN,” *J. Appl. Phys.* 129, 034103 (2021).

Chapter 6

Oxygen atoms incorporation for thickness scaling

6.1 Concepts of oxygen atoms incorporation in $\text{Al}_{1-x}\text{Sc}_x(\text{O})\text{N}$

Films

In chapter 5, the reduction of E_c and releasing the strain at the AlScN/bottom electrode is needed to keep scaling down the thickness of AlScN films. In this chapter, oxygen atoms incorporation is evaluated for two targets. One of the targets is to reduce E_c . Figures 6.1 and 6.2 showed switching with or without oxygen bonding. Without oxygen bonding, N atoms need to be displaced to move N atoms for switching. Substitution of N atoms to O atoms can elongate c axis lattice constant and the valence number difference may ease the N atom movement.

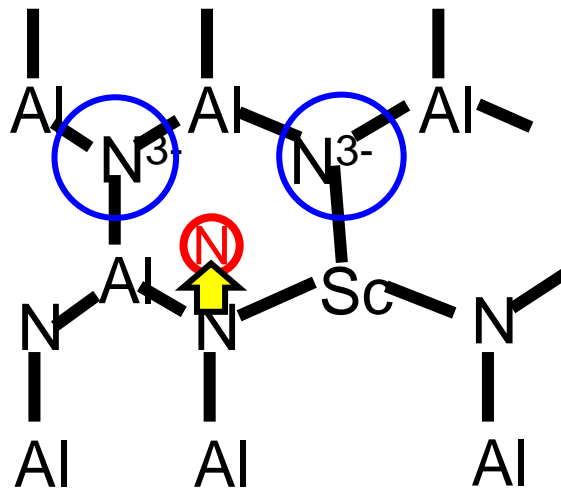


Figure 6.1 Switching without oxygen bonding.

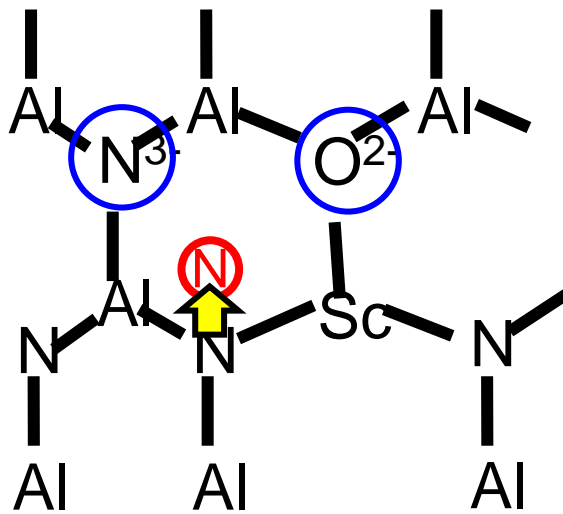


Figure 6.2 Switching with oxygen bonding.

The purpose of this chapter is to show the effect of oxygen atoms incorporation with the ferroelectric characteristics.

6.2 Fabrication process of ferroelectric capacitors

The fabrication process is almost the same as in chapter 1. 50-nm-thick $\text{Al}_{1-x}\text{Sc}_x(\text{O})\text{N}$ film was deposited by DC reactive sputtering from an $\text{Al}_{0.57}\text{Sc}_{0.43}$ target in Ar 5 sccm, N_2 10 sccm, O_2 0~1sccm, ambient at 0.7 Pa chamber pressure. The top TiN layer and Al layer were patterned by RIE dry etching to form electrodes. The fabrication process flow and the schematic illustration of the fabricated MIM capacitor are shown in figures 6.3 and 6.4, respectively.

- n⁺Si substrate cleaning
- Sputter-deposited TiN (10nm) for bottom electrode
- Sputter-deposited Al_{1-x}Sc_xN (50nm) with O₂
- Sputter-deposited TiN (40nm) for top electrode
- Evaporation-deposited Al
- Photolithography
- Etching by RIE dry etching
- Evaporation-deposited Al

Figure 6.3 Fabrication process flow of Al_{1-x}Sc_x(O)N MIM capacitor.

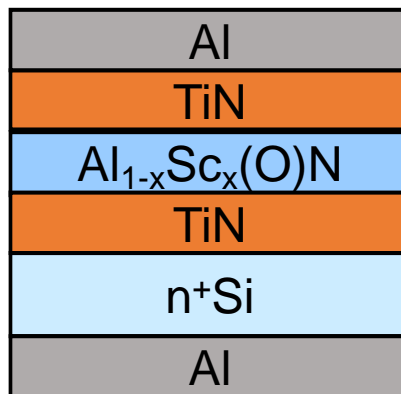


Figure 6.4 A schematic illustration of the fabricated Al_{1-x}Sc_x(O)N MIM capacitor.

6.3 Experiment results of Al_{1-x}Sc_x(O)N Capacitors

Figure 6.5 shows the *CV* measurement results of Al_{1-x}Sc_x(O)N MIM capacitors with different gas flows of oxygen gas. The dielectric constant can be extracted from *CV* curves. The ferroelectricity in *CV* curves starts to diminish for the gas flow of 0.4 sccm O₂ deposited capacitors.

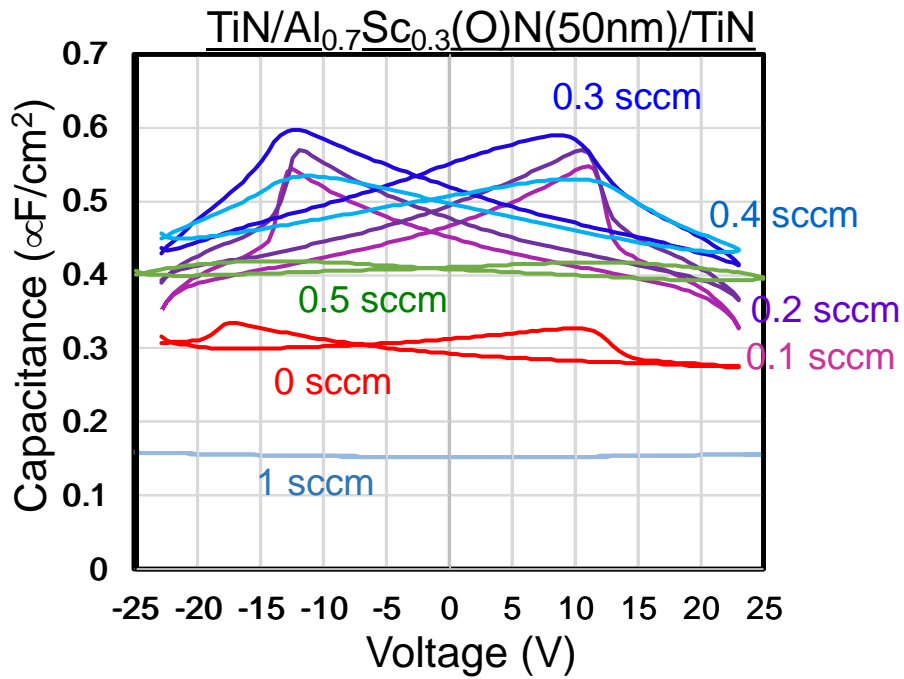


Figure 6.5 CV measurements results of $Al_{1-x}Sc_x(O)N$ MIM capacitors with different gas flows of oxygens.

Figure 6.6 shows the extracted dielectric constant of $Al_{1-x}Sc_x(O)N$. The dielectric constant of about 30 is achieved.

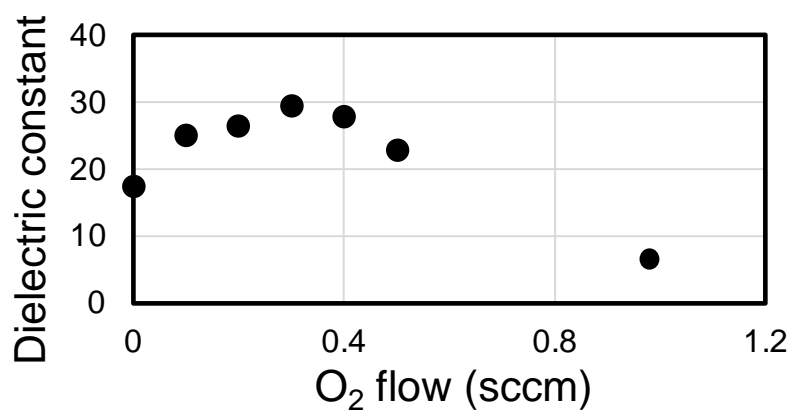


Figure 6.6 Dielectric constant of $Al_{1-x}Sc_x(O)N$ MIM capacitor with different gas flows of oxygen amount.

Figure 6.7 and 6.8 shows JV curves and extracted parameters of $Al_{1-x}Sc_x(O)N$ MIM capacitor with different oxygen amount. E_{BD} reduces with oxygen atoms incorporation. Leakage current tends to increase with oxygen atoms incorporation.

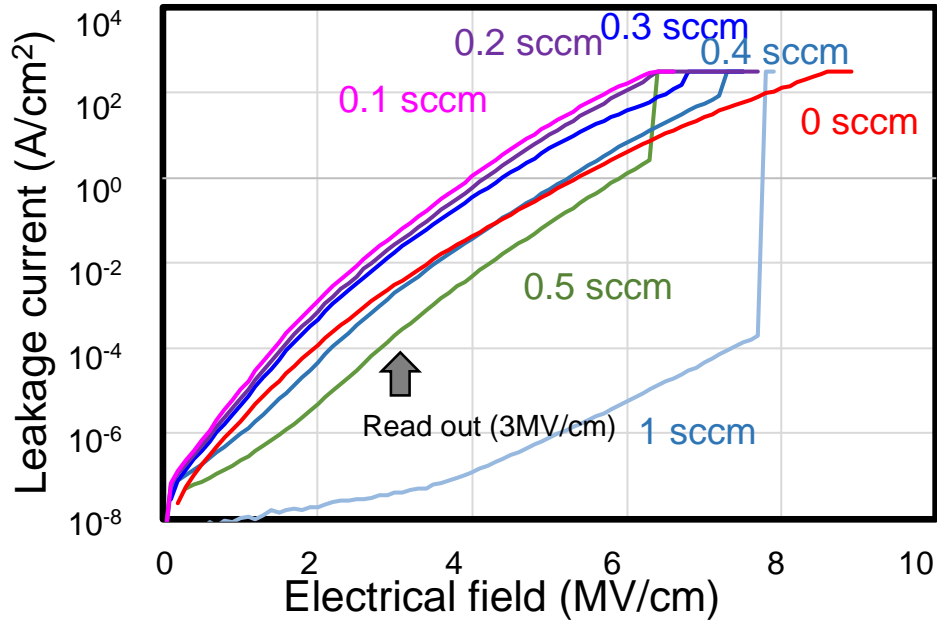


Figure 6.7 JV curves of $Al_{1-x}Sc_x(O)N$ MIM capacitor with different gas flow of oxygen amount.

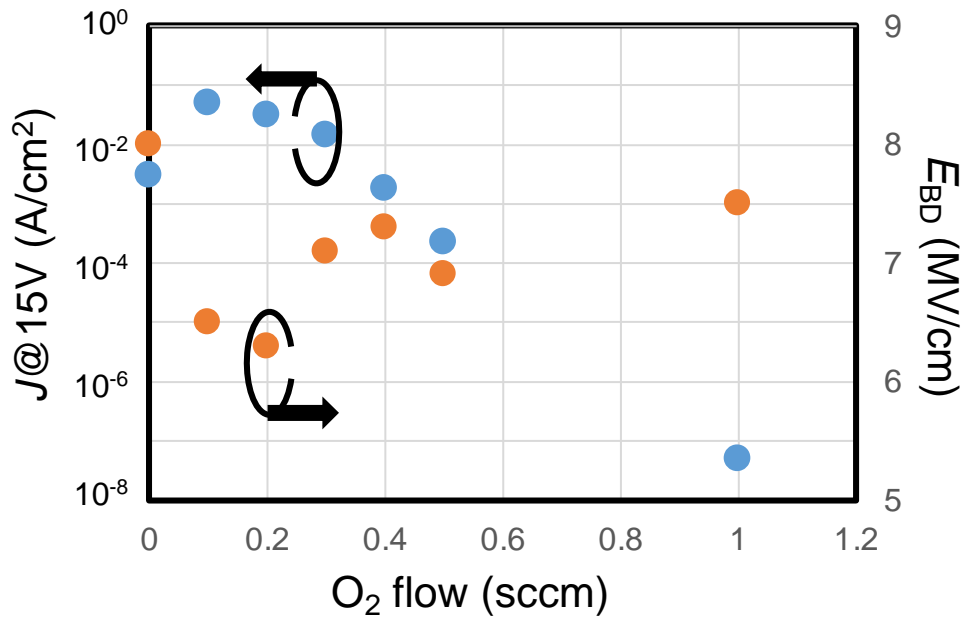


Figure 6.8 Leakage current and breakdown electrical field of $\text{Al}_{1-x}\text{Sc}_x(\text{O})\text{N}$ MIM capacitor with different gas flows of oxygen amount.

Figure 6.9 shows SIMS results of $\text{Al}_{1-x}\text{Sc}_x(\text{O})\text{N}$ MIM capacitor with different oxygen amounts. The uniform distribution of oxygen atoms in AlScN film were confirmed by SIMS. Figure 6.10 shows XPS measurement and analysis of $\text{Al}_{1-x}\text{Sc}_x(\text{O})\text{N}$ MIM capacitor with different oxygen amounts. No composition ratio change for Al:Sc=0.7:0.3. XPS revealed a composition of $\text{Al}_{0.7}\text{Sc}_{0.3}\text{O}_{0.2}\text{N}_{0.8}$ for the gas flow of 0.3 sccm O_2 deposited capacitors and $\text{Al}_{0.7}\text{Sc}_{0.3}\text{O}_{0.3}\text{N}_{0.7}$ for the gas flow of 0.4 sccm O_2 deposited capacitors. 5% O_2 is also found in AlScN without adding O_2 gas flow. Oxygen atoms preferentially bond with Al atoms and were observed by XPS.

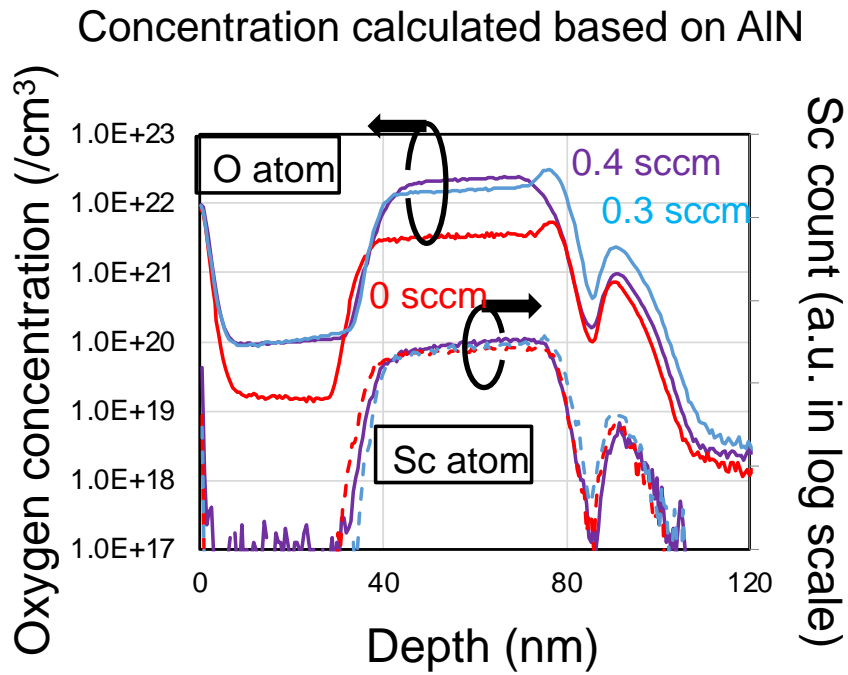


Figure 6.9 SIMS results of $\text{Al}_{1-x}\text{Sc}_x(\text{O})\text{N}$ MIM capacitor with different gas flows of oxygen amount.

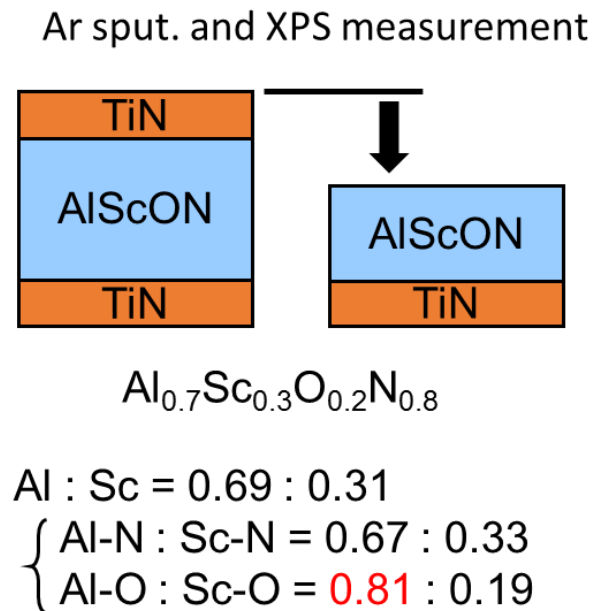


Figure 6.10 XPS measurement and analysis for the gas flow of 0.3 sccm O_2 deposited capacitors.

Figure 6.11 shows Out-of-plane XRD patterns of $\text{Al}_{1-x}\text{Sc}_x(\text{O})\text{N}$ films. Comparing (002) peaks of $\text{Al}_{0.7}\text{Sc}_{0.3}\text{N}$ & $\text{Al}_{0.7}\text{Sc}_{0.3}\text{O}_{0.2}\text{N}_{0.8}$ films, the c lattice constant increases with oxygen atom incorporation. Figure 6.12 shows XRC patterns of $\text{Al}_{1-x}\text{Sc}_x(\text{O})\text{N}$ films. FWHM is almost the same for AlScN & $\text{Al}_{0.7}\text{Sc}_{0.3}\text{O}_{0.2}\text{N}_{0.8}$ samples. Excess oxygen incorporation results in the formation of AlScO_3 . Optimum oxygen content exists.

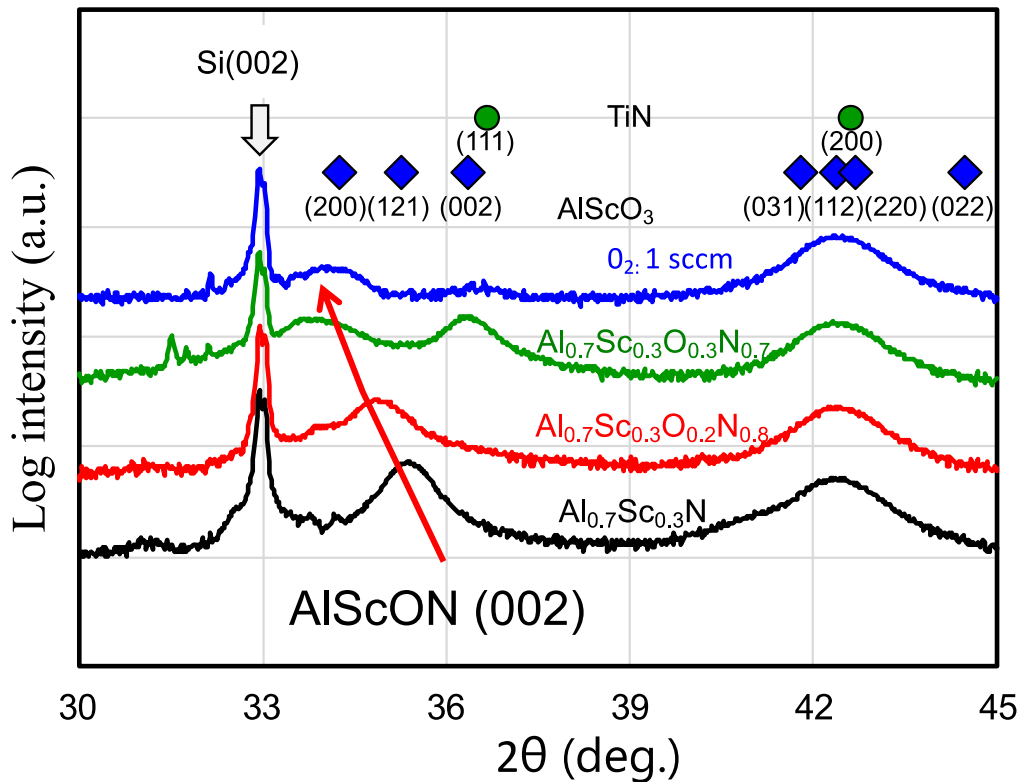


Figure 6.11 Out-of-plane XRD patterns of $\text{Al}_{1-x}\text{Sc}_x(\text{O})\text{N}$ films.

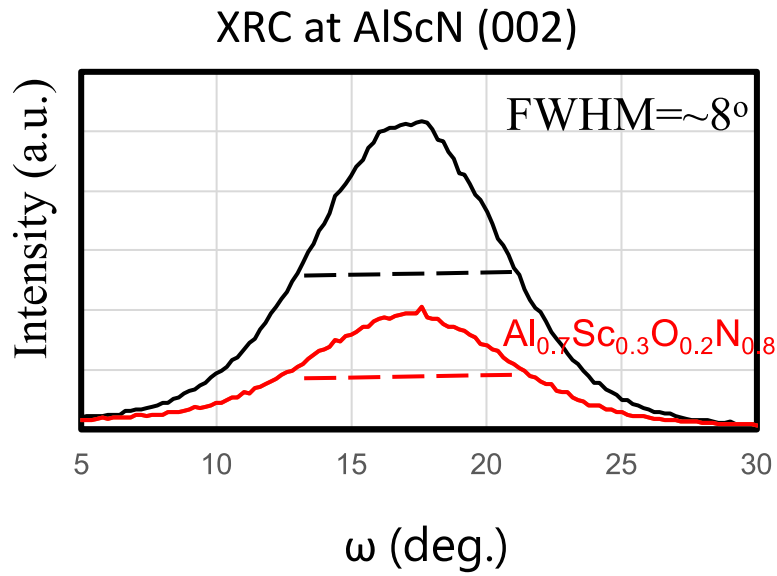


Figure 6.12 XRC patterns of $\text{Al}_{1-x}\text{Sc}_x(\text{O})\text{N}$ films.

Figure 6.13 shows the remanent polarization of $\text{Al}_{1-x}\text{Sc}_x(\text{O})\text{N}$ MIM capacitors. E_c of 2.75 MV/cm for $\text{Al}_{0.7}\text{Sc}_{0.3}\text{O}_{0.2}\text{N}_{0.8}$ films and 3.8 MV/cm for $\text{Al}_{0.7}\text{Sc}_{0.3}\text{N}$ films. E_c increases again with excess oxygen atoms incorporation. Figure 6.14 shows the endurance of $\text{Al}_{1-x}\text{Sc}_x(\text{O})\text{N}$ MIM capacitors. The electrical field applied is selected from figure 6.13 to target $90 \mu\text{C}/\text{cm}^2$. No improvement in switching cycles with oxygen atoms incorporation.

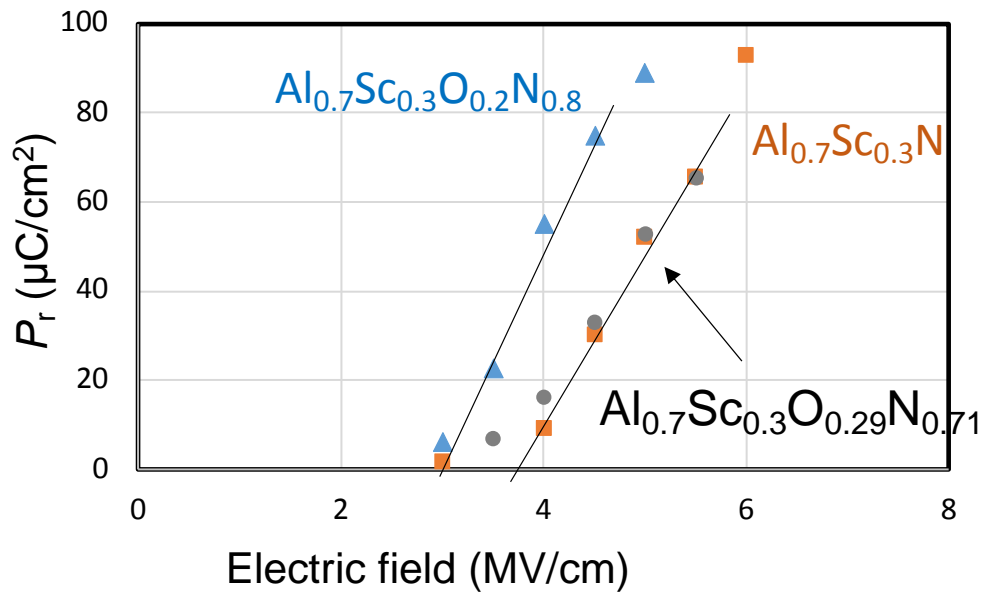


Figure 6.13 Remanent polarization of $\text{Al}_{1-x}\text{Sc}_x(\text{O})\text{N}$ MIM capacitors.

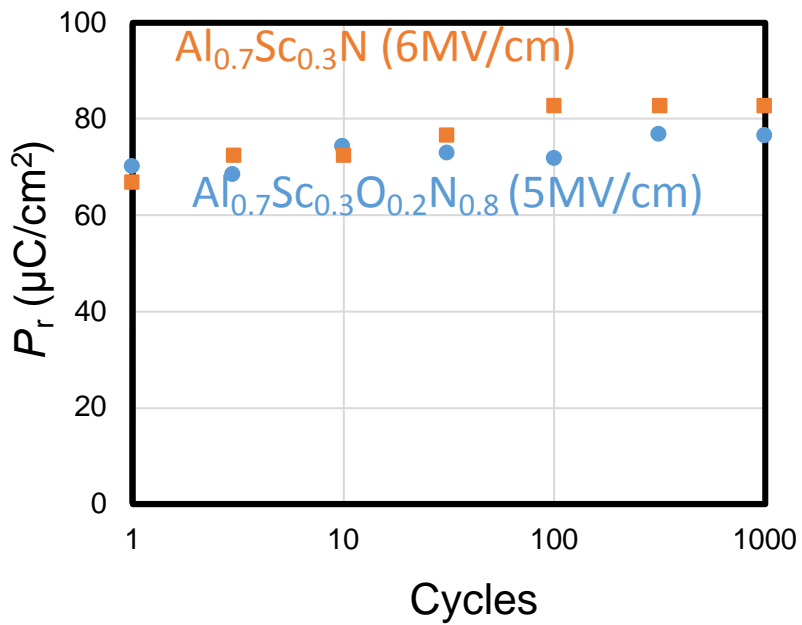


Figure 6.14 Endurance of $\text{Al}_{1-x}\text{Sc}_x(\text{O})\text{N}$ MIM capacitors.

Figures 6.15 and 6.16 shows the *CV* measurements of $\text{Al}_{0.7}\text{Sc}_{0.3}\text{N}$ and $\text{Al}_{0.7}\text{Sc}_{0.3}\text{O}_{0.2}\text{N}_{0.8}$ MIM capacitors with thicknesses of 50nm to 7nm. It still showed the hysteresis *CV* for a thickness of 7nm. Dielectric constants are kept at ~ 30 with scaling down to 7 nm. <5 V switching operation is confirmed.

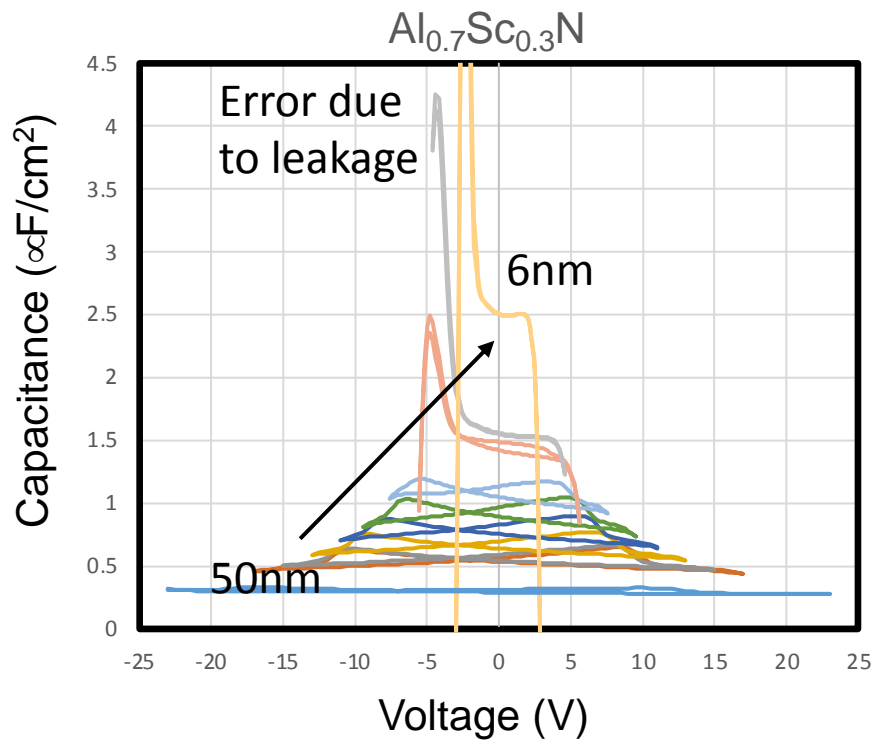


Figure 6.15 Thickness scaling of $\text{Al}_{0.7}\text{Sc}_{0.3}\text{N}$ MIM capacitor in *CV* curves.

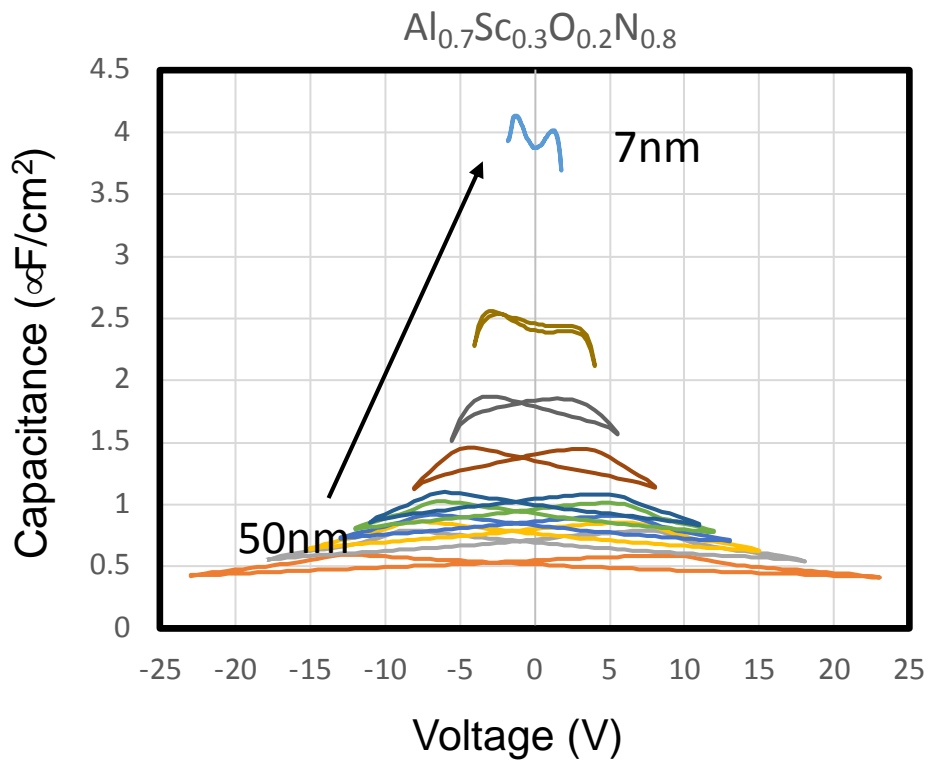


Figure 6.16 Thickness scaling of $\text{Al}_{0.7}\text{Sc}_{0.3}\text{O}_{0.2}\text{N}_{0.8}$ MIM capacitor in *CV* curves.

Figures 6.17 and 6.18 show the thickness scaling of $\text{Al}_{0.7}\text{Sc}_{0.3}\text{N}$ and $\text{Al}_{0.7}\text{Sc}_{0.3}\text{O}_{0.2}\text{N}_{0.8}$ MIM capacitor in *PV* curves. Figures 6.19 and 6.20 show extracted E_c and $P_{r,\text{max}}$. E_c reduction with oxygen incorporation is preserved on thickness scaling. Still, P_r decreases with thickness scaling (excess leakage).

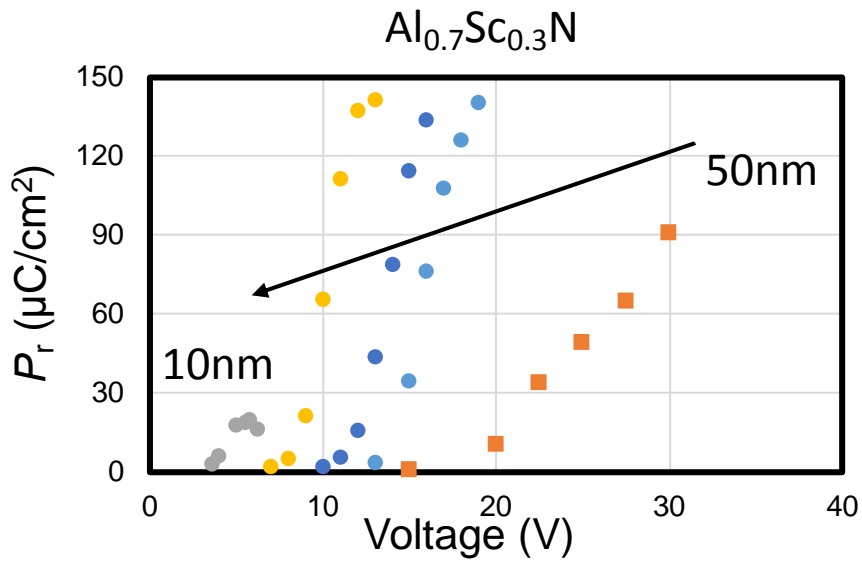
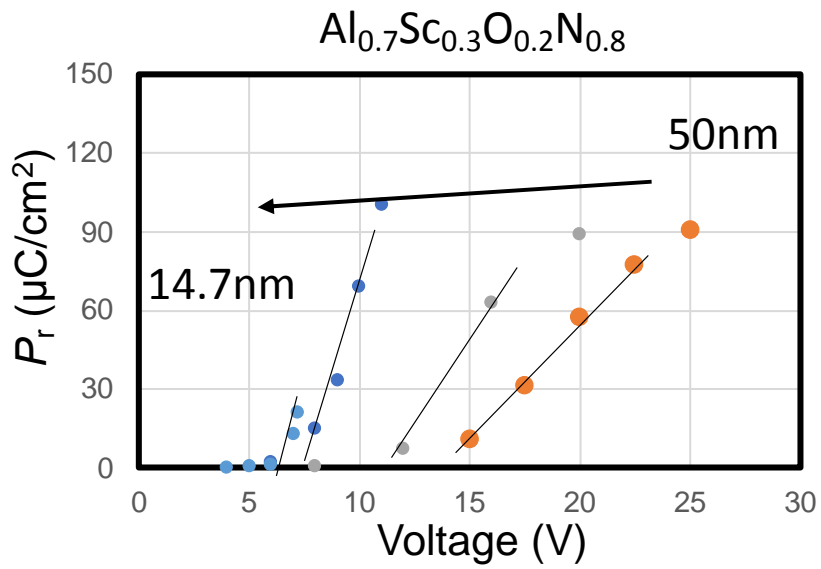


Figure 6.17 Thickness scaling of $\text{Al}_{0.7}\text{Sc}_{0.3}\text{N}$ MIM capacitors in PV curves.



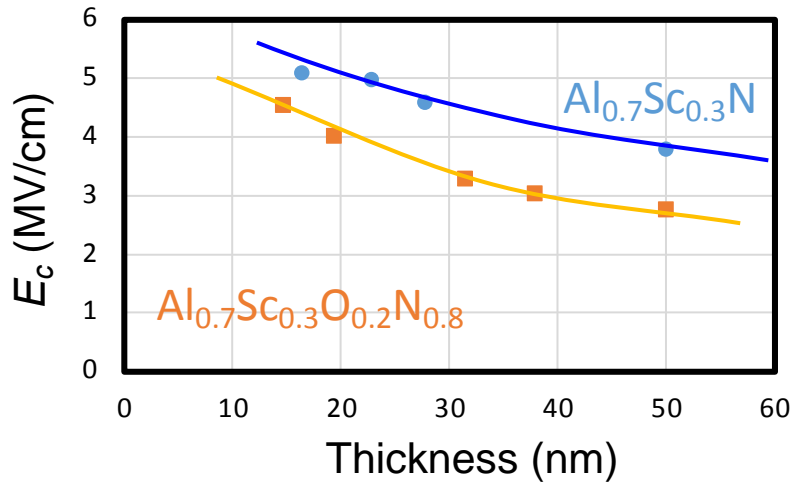


Figure 6.19 Thickness scaling of $Al_{0.7}Sc_{0.3}N$ MIM capacitors in E_c .

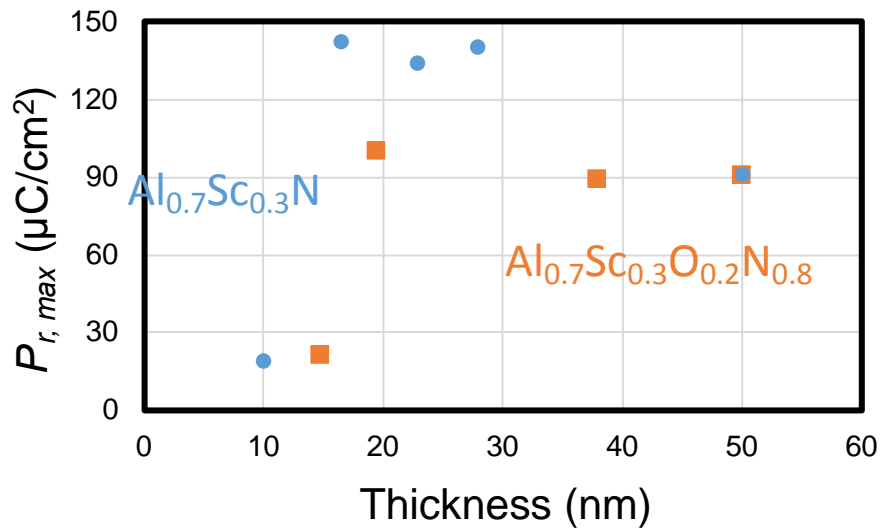


Figure 6.20 Thickness scaling of $Al_{0.7}Sc_{0.3}O_{0.2}N_{0.8}$ MIM capacitors in $P_{r,max}$.

Figure 6.21 show the thickness scaling model with oxygen atoms incorporation. The layer with strain also occurs in the AlScON layer. The influence of the layer with strain also appears with thickness scaling down. The high leakage current between AlScON and the bottom electrode needs to be solved.

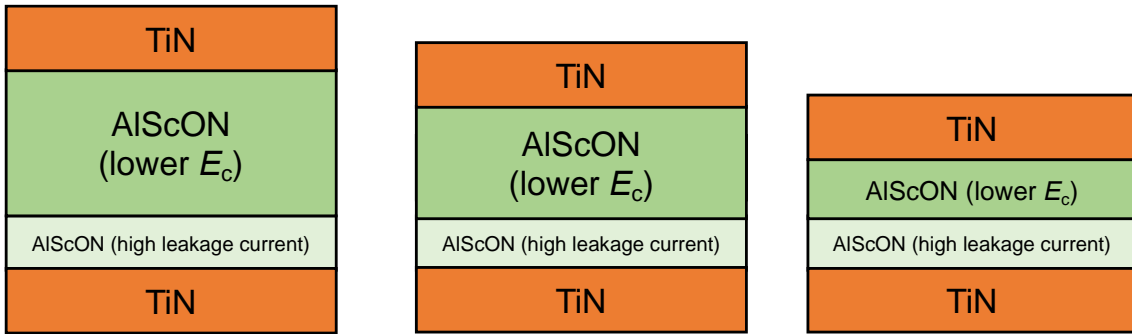


Figure 6.21 Thickness scaling model with oxygen atoms incorporation.

Figures 6.22 and 6.23 show the benchmark of the obtained ferroelectric properties [6.1, 6.2]. The thickness of Yasuoka's group in figure 6.22 is about 140 nm which is thicker than our device. Obtained P_r of $\text{Al}_{0.7}\text{Sc}_{0.3}\text{O}_{0.2}\text{N}_{0.8}$ layer is slightly lower than literature. E_c of $\text{Al}_{0.7}\text{Sc}_{0.3}\text{O}_{0.2}\text{N}_{0.8}$ is lower than the literature. Better thickness scaling by lower E_c is obtained. Figure 6.24 shows the benchmark of the obtained E_c with the c/a ratio. Researchers can only adjust E_c by controlling the composition of Sc before. These results give researchers another method to design E_c by different amounts of oxygen incorporation.

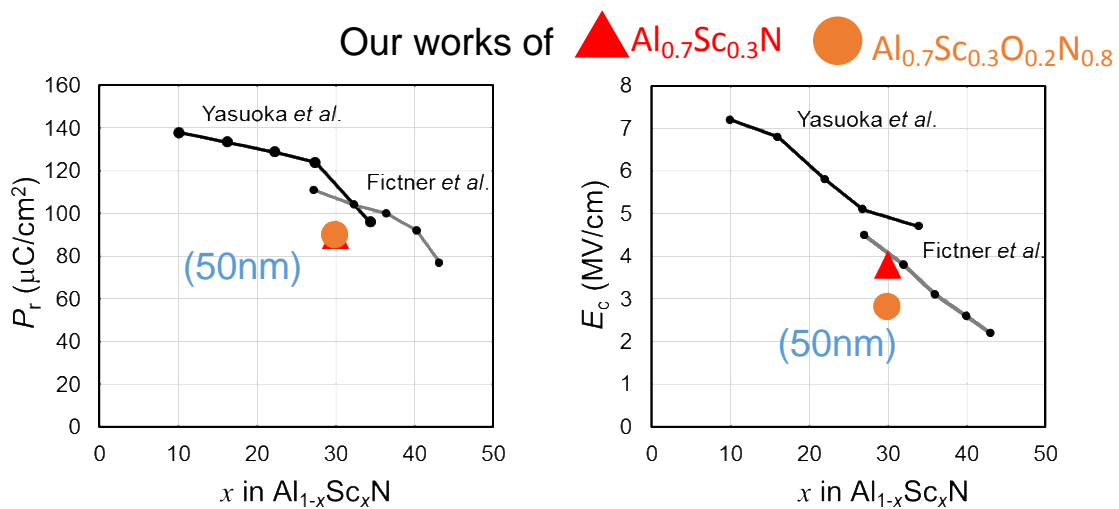


Figure 6.22 Benchmark of the obtained ferroelectric properties.

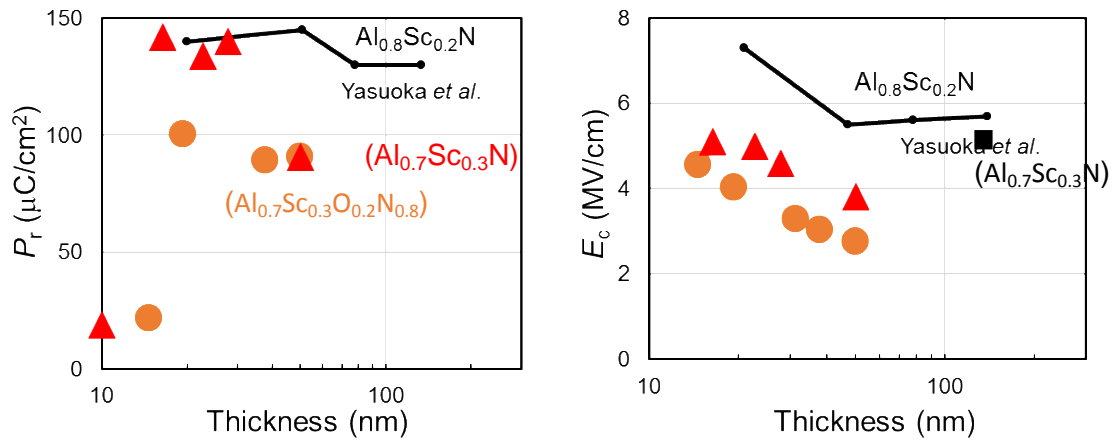


Figure 6.23 Benchmark of the obtained ferroelectric properties with thickness scaling.

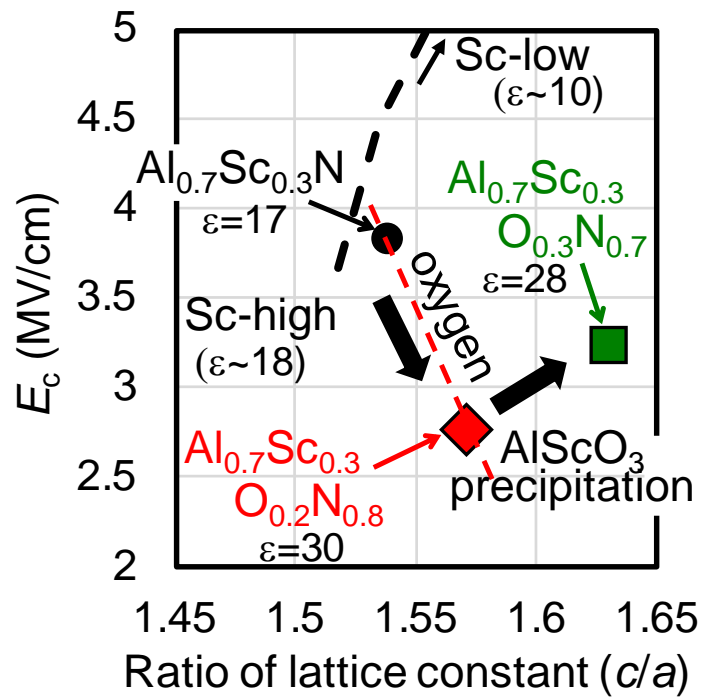


Figure 6.24 Benchmark of the obtained E_c with c/a ratio.

6.4 Summary of this chapter

The purpose of this chapter is to show the effect of oxygen atoms incorporation with the ferroelectric characteristics

Oxygen atoms distort the wurtzite structure to ease the N displacement; lower E_c can be obtained. Leakage current tends to increase with oxygen incorporation. Excess oxygen incorporation results in oxide formation and degrades the ferroelectricity. Better thickness scaling by lower E_c , but still, E_c increases with a thinner layer. Oxygen atoms incorporation cannot release the strain near AlScON/bottom electrode; need more material research

References

[6.1] S. Yasuoka, J. Appl. Phys., 128, 114103 (2020)

[6.2] S. Fichtner, N. Wolff, F. Lofink, L. Kienle, and B. Wagner, "AlScN: A III-V semiconductor based Ferroelectric," J. Appl. Phys. 125, 114103 (2019).

Chapter 7

AlScON/AlScN stacking for reliable ferroelectric films

7.1 Concepts of AlScON/AlScN stacking

In the previous chapter's conclusions, the high leakage current between AlScON and the bottom electrode needs to be solved. Low E_c is still needed for thickness scaling. Stacking of AlScON/AlScN for low E_c with low leakage is proposed. Leakage current can be suppressed with the $\text{Al}_{0.7}\text{Sc}_{0.3}\text{N}$ barrier layer. Low E_c can still maintain the same bulk $\text{Al}_{0.7}\text{Sc}_{0.3}\text{O}_{0.2}\text{N}_{0.8}$ films. Figure 7.1 shows a schematic illustration of the AlScON/AlScN stacking capacitor.

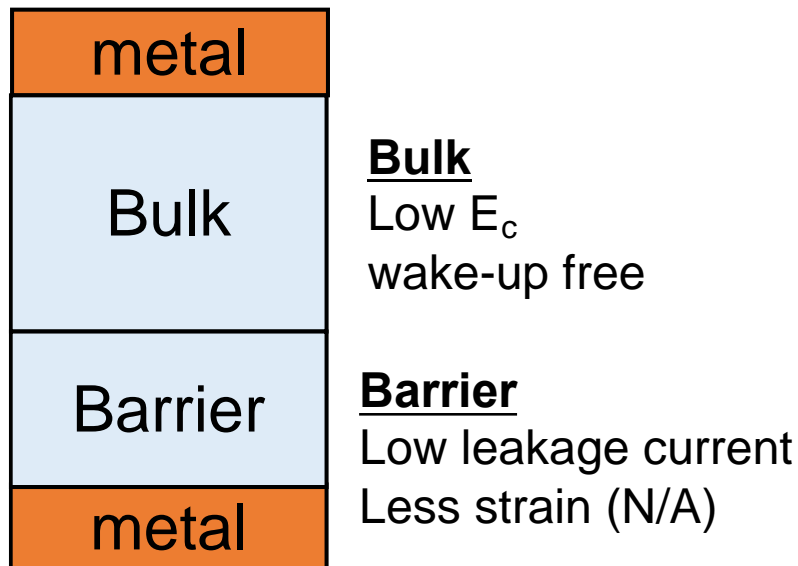


Figure 7.1 A schematic illustration of the AlScON/AlScN stacking capacitor.

Figure 7.2 shows schematic illustrations of the fabricated AlScON/AlScN stacking capacitor. The barrier layer is low leakage current $\text{Al}_{0.7}\text{Sc}_{0.3}\text{N}$ layer which was set at 5-nm-thick. The bulk layer is $\text{Al}_{0.7}\text{Sc}_{0.3}\text{O}_{0.2}\text{N}_{0.8}$ films for low E_c . Figure 7.3 shows the JV curves of the AlScON/AlScN stacking capacitor. Leakage current suppression with $\text{Al}_{0.7}\text{Sc}_{0.3}\text{N}$ barrier layer. Slight increase in the breakdown field compared to $\text{Al}_{0.7}\text{Sc}_{0.3}\text{O}_{0.2}\text{N}_{0.8}$ films.

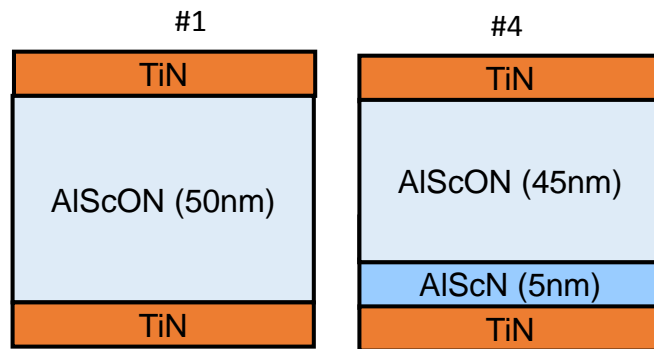


Figure 7.2 Schematic illustrations of the fabricated AlScON/AlScN stacking capacitor.

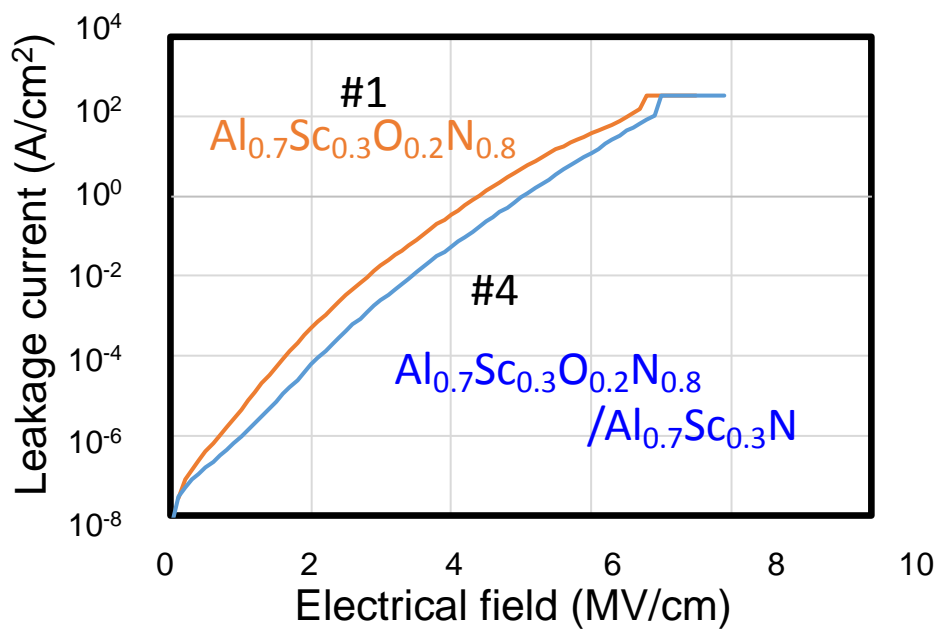


Figure 7.3 *JV* curves of AlScON/AlScN stacking capacitor.

The purpose of the chapter is to find reliable ferroelectric films with better reliability and scalability

7.2 Experiment results of AlScON/AlScN stacking Capacitors

Figure 7.4 shows illustrations of the fabricated AlSc(O)N/AlSc(O)N stacking capacitors. Figure 7.5 shows *CV* measurement results of fabricated AlSc(O)N/AlSc(O)N stacking capacitors. Low switching voltage with bulk-AlScON layer is confirmed. Barrier-AlScON does not lower the E_c . The results show that E_c is determined by the bulk layer.

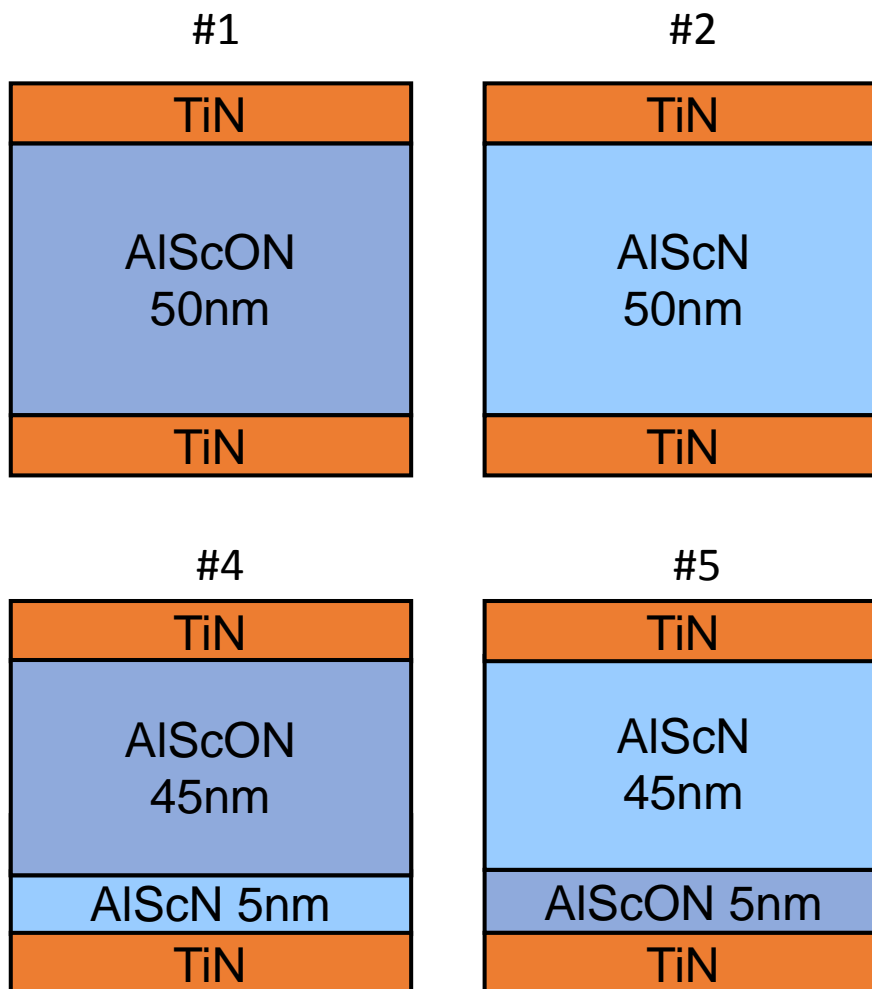


Figure 7.4 Illustrations of the fabricated AlSc(O)N/AlSc(O)N stacking capacitors.

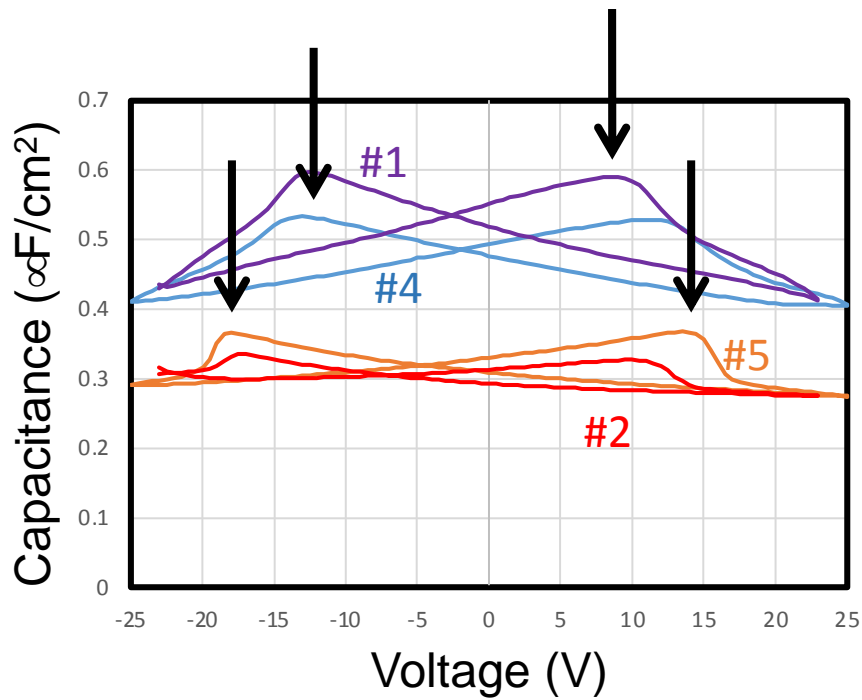


Figure 7.5 CV measurements results of fabricated AlSc(O)N/AlSc(O)N stacking capacitors.

Figures 7.6 and 7.7 show the ferroelectric properties of the AlScON/AlScN stacking capacitor. E_c of 3.1 MV/cm comparable to a single AlScON layer of 2.8 MV/cm. The electrical field applied in figure 7.7 is selected from figure 7.6 to target $90 \mu\text{C}/\text{cm}^2$. The wake-up effect observed due to AlScN barrier layer. Switching cycle endurance improved with the AlScN barrier layer.

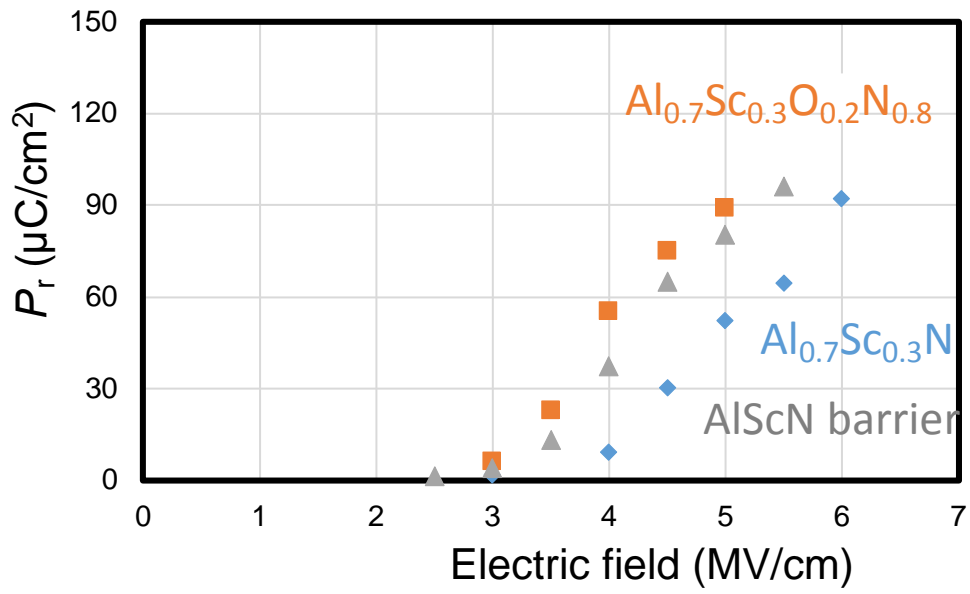


Figure 7.6 Remanent polarization of AlScON/AiScN stacking capacitors.

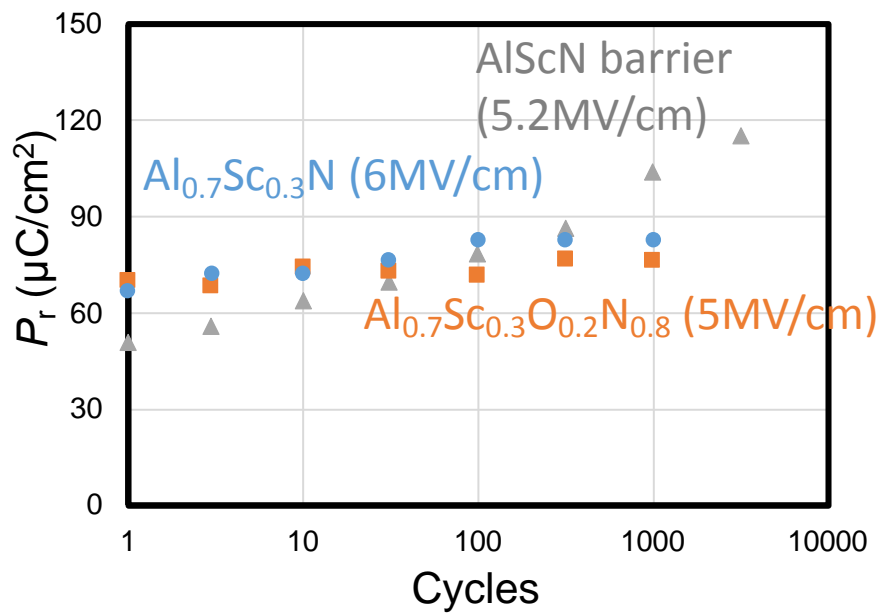


Figure 7.7 Endurance of AlScON/AiScN stacking capacitors.

Figure 7.8 shows the thickness scaling of the AlScON/AlScN stacking capacitor in CV curves. Ferroelectric-type hysteresis was observed with 6.7nm devices. <5 V switching operation is confirmed.

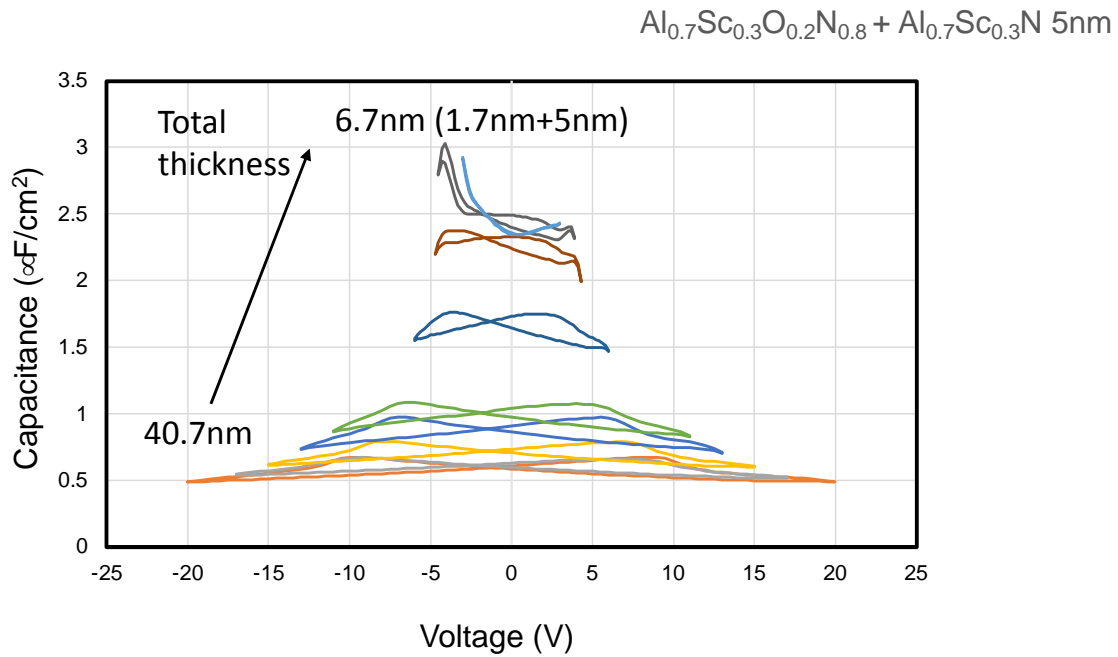


Figure 7.8 Thickness scaling of AlScON/AlScN stacking capacitor in CV curves.

Figure 7.9 shows the thickness scaling of the AlScON/AlScN stacking capacitor in E_c . Figure 7.10 shows the thickness scaling of the AlScON/AlScN stacking capacitor in $P_{r,max}$. E_c has the same trend with $\text{Al}_{0.7}\text{Sc}_{0.3}\text{O}_{0.2}\text{N}_{0.8}$ during the thickness scaling also indicating that E_c is decided by bulk layer. Thickness scaling improved slightly with an AlScN barrier layer.

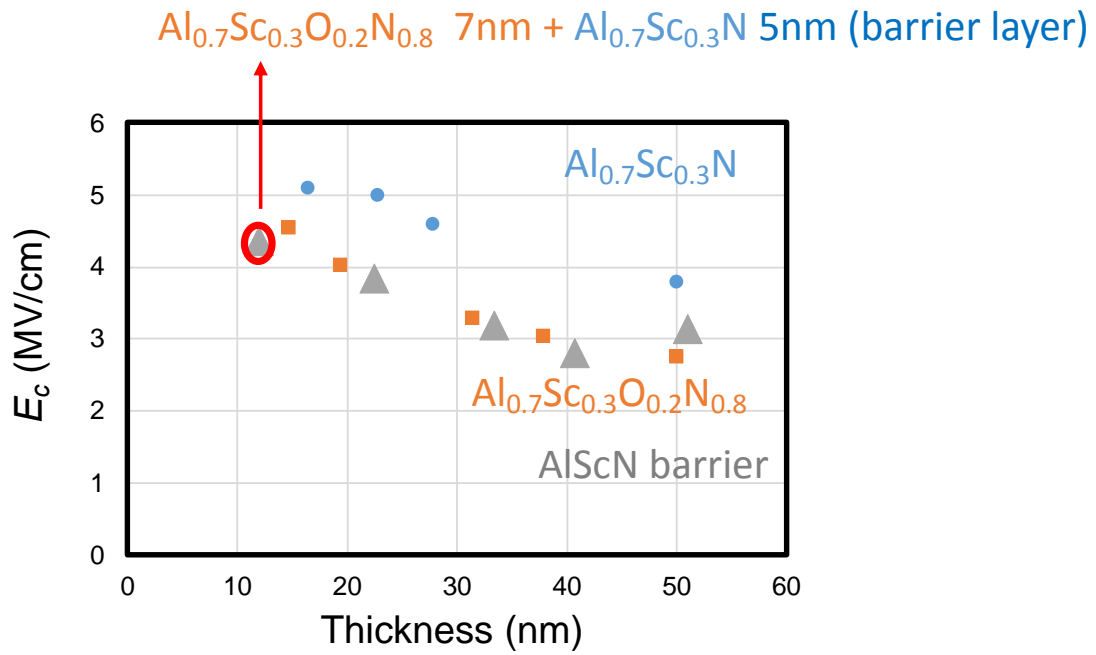


Figure 7.9 Thickness scaling of AlScON/AIScN stacking capacitor in E_c .

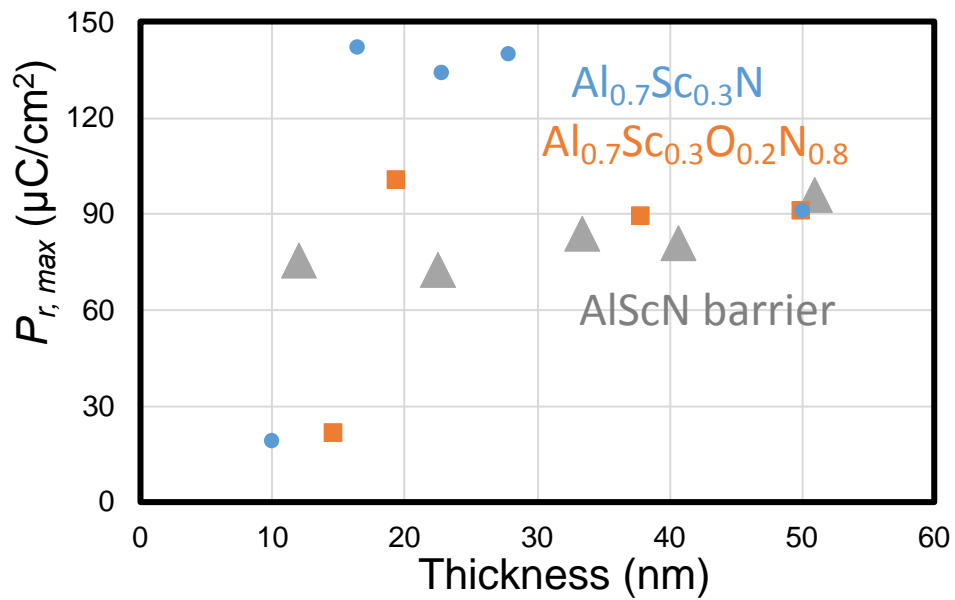


Figure 7.10 Thickness scaling of AlScON/AIScN stacking capacitor in $P_{r,max}$.

Figure 7.11 shows the benchmark of the obtained ferroelectric properties with thickness scaling. P_r improved to 12 nm with AlScON/AlScN stacked films. The trend of E_c is close to the $\text{Al}_{0.7}\text{Sc}_{0.3}\text{O}_{0.2}\text{N}_{0.8}$ layer, which is dependent on the bulk AlScN layer. Better thickness scaling by lower E_c is obtained.

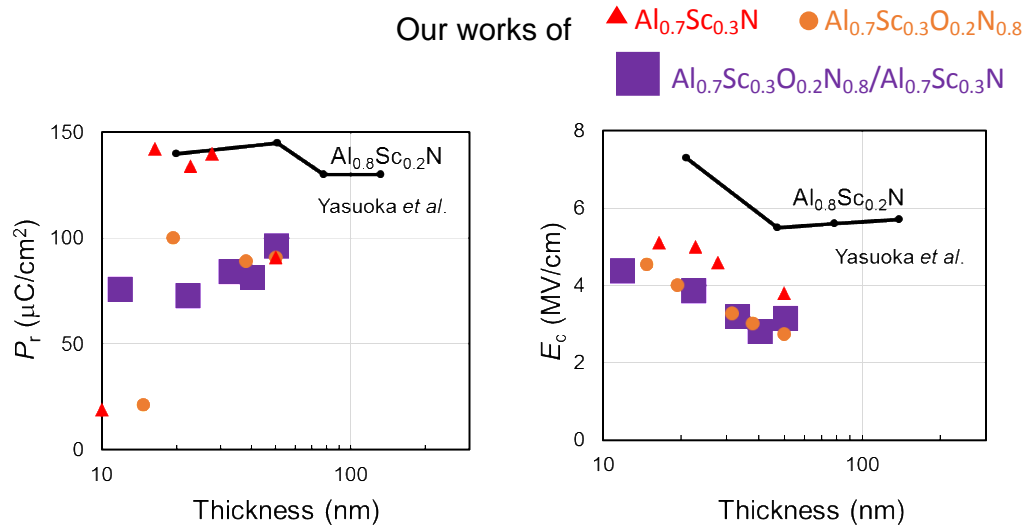


Figure 7.11 Benchmark of the obtained ferroelectric properties with thickness scaling.

7.3 Summary of this chapter

The purpose of the chapter is to find reliable ferroelectric films with better reliability and scalability.

E_c is determined by the bulk layer. Longer switching cycle endurance with AlScN barrier layer. Ferroelectric-type hysteresis was observed with 6.7nm devices. <5 V switching operation confirmed. Better thickness scaling with P_r and lower E_c .

Chapter 8

Conclusions

With the slowing of Moore's law, 3DIC is considered to be the next future for progressing. In this thesis, although post-annealing to the AlScN capacitors has been evaluated, it showed little change in crystallinity and ferroelectric properties which means initial deposition temperature is the key to improving properties. Low-temperature deposited 50-nm-thick AlScN MIM capacitors with CMOS-compatible metal electrode has been demonstrated. It is compatible with memory and with plastic or resin substrates that used for 3DIC. 400°C deposited AlScN is also demonstrated and is compatible with the BEOL process.

Then, reliability and breakdown mechanism has been evaluated by analyzing leakage current with cycling tests. Leakage current before and after switching cycles followed the Schottky emission model. It showed local conduction path was hardly formed, which is different from oxide-based ferroelectric films. The evaluation with AFM also indicated that a local conduction path is not found. A breakdown mechanism model has been proposed. These results give researchers a guideline to know the breakdown mechanism and to elongate the endurance. Either to deal with nitrogen vacancies at the AlScN/metal interface or bulk AlScN.

After knowing the reliability of AlScN, thickness scaling for AlScN has been conducted. A model is created to explain the change in P_r upon thickness scaling. The (002) oriented films were confirmed even with a thickness of 10 nm by XRC analysis. Reduction in P_r measured at 5 MV/cm for thin layers was observed, suggesting the increase in E_c . The increase in E_c is suggested to be the strain at AlScN/bottom electrode. The results showed that AlScN grew column well at AlScN/top electrode. These results give researchers guidelines for further scaling AlScN. Researchers must solve the increased leakage current and increasing E_c for further scaling down for AlScN.

Oxygen atoms incorporation in AlScN films has been evaluated for the purpose of lower E_c and releasing the stress at AlScN/bottom electrode. Although Oxygen atoms incorporation cannot release the strain near AlScON/bottom electrode and more material research is needed to reduce the leakage current and to release the strain near AlScON/bottom electrode, E_c has succeeded to reduce to 2.8 MV/cm. Researchers can only adjust E_c by controlling the composition of Sc before. These results give researchers another method to design E_c by different amounts of oxygen incorporation.

A concept of stacking of AlScON/AlScN is evaluated for the purpose of low leakage current with low E_c . The way of releasing the strain at the AlScN/bottom electrode has not been found yet. More barrier layer research may find out the optimization of the barrier layer. Such as setting $\text{Al}_{0.7}\text{Sc}_{0.3}\text{O}_{0.3}\text{N}_{0.7}$ as a barrier layer for the purpose of further reducing leakage current. However, E_c is high for $\text{Al}_{0.7}\text{Sc}_{0.3}\text{O}_{0.3}\text{N}_{0.7}$. The optimization may be found with more experiments. $\text{Al}_{0.7}\text{Sc}_{0.3}\text{O}_{0.2}\text{N}_{0.8}$ / $\text{Al}_{0.7}\text{Sc}_{0.3}\text{N}$ stacking capacitors showed improved thickness scaling to 7 nm (2nm+5nm) at operation voltage below 5 V. This concept gives researchers a prototype to design E_c and leakage current for thickness scaling. And $\text{Al}_{0.7}\text{Sc}_{0.3}\text{O}_{0.2}\text{N}_{0.8}$ / $\text{Al}_{0.7}\text{Sc}_{0.3}\text{N}$ stacking capacitors reach the milestone of operating below 5 V.

In conclusion, AlSc(O)N showed high potential as a ferroelectric material. Although considering the strong switching of AlScN (box profile), it may be hard for AlScN to elongate endurance to 10^{12} cycles. Nevertheless, AlSc(O)N still maintains lots of possibility with its ferroelectricity. Such as applying to GaN HEMT to shift threshold voltage. Besides, AlScN also showed good performance in piezoelectricity, or also it is possible to be used as a semiconductor material. To sum up, AlScN still has lots of possibilities worth researchers pursuing.

List of Publications

1. Chin-Chung Chen, Ching-Kai Lin, Chen-Wei Chang, Yun-Chien Cheng, **Sung-Lin Tsai**, Jia-En Chen, Tien-Kan Chung, “Passive Magnetic-Flux-Concentrator Based Electromagnetic Targeting System for Endobronchoscopy”, *Sensors* 19, no.23 , 5105, 2019.
2. **Sung-Lin Tsai**, Kazuki Kusafuka, Takuya Hoshii, Hitoshi Wakabayashi, Kazuo Tsutsui, Kuniyuki Kakushima, “Electrical Characterization of Sputter Deposited $\text{Al}_x\text{Sc}_{1-x}\text{N}$ Thin Films”, *ECS Transactions*, Vol.97, No.3, pp45-48, 2020.
3. **Sung-Lin Tsai**, Takuya Hoshii, Hitoshi Wakabayashi, Kazuo Tsutsui, Kuniyuki Kakushima, “Highly Oriented Growth of $\text{Al}_x\text{Sc}_{1-x}\text{N}$ Ferroelectric Film on W Bottom Electrodes”, *ECS Transactions*, Vol.98, No.3, pp57-61, 2020.
4. Junji Kataoka, **Sung-Lin Tsai**, Takuya Hoshii, Hitoshi Wakabayashi, Kazuo Tsutsui, Kuniyuki Kakushima, “N-type conduction of sputter-deposited polycrystalline $\text{Al}_{0.78}\text{Sc}_{0.22}\text{N}$ films by Si ion implantation”, *Applied Physics Express*, Vol.14, 021002, 2021
5. **Sung-Lin Tsai**, Takuya Hoshii, Hitoshi Wakabayashi, Kazuo Tsutsui, Tien-Kan Chung, Edward Yi Chang, Kuniyuki Kakushima, “On the thickness scaling of ferroelectricity in $\text{Al}_{0.78}\text{Sc}_{0.22}\text{N}$ films”, *Japanese Journal of Applied Physics*, Vol.60, SBBA05, 2021
6. **Sung-Lin Tsai**, Takuya Hoshii, Hitoshi Wakabayashi, Kazuo Tsutsui, Tien-Kan Chung, Edward Yi Chang, Kuniyuki Kakushima, “Room-temperature deposition of a

highly-oriented poling-free ferroelectric AlScN film by reactive sputtering”, Applied Physics Letters, Vol.118, 082902, 2021

7. Junji Kataoka, **Sung-Lin Tsai**, Takuya Hoshii, Hitoshi Wakabayashi, Kazuo Tsutsui, Kuniyuki Kakushima, “A possible origin of the large leakage current in ferroelectric $Al_{1-x}Sc_xN$ films”, Japanese Journal of Applied Physics, Vol. 60, 030907, 2021

8. **Sung-Lin Tsai**, Takuya Hoshii, Hitoshi Wakabayashi, Kazuo Tsutsui, Tien-Kan Chung, Edward Yi Chang, Kuniyuki Kakushima, “Field cycling behavior and breakdown mechanism of ferroelectric $Al_{0.78}Sc_{0.22}N$ films”, Japanese Journal of Applied Physics, Vol. 61, SJ1005, 2022

9. Chen Si-Meng, **Tsai Sung-Lin**, Mizutani Kazuto, HOSHII Takuya, WAKABAYASHI Hitoshi, TSUTSUI Kazuo, Chang Edward Yi, Kakushima Kuniyuki, "GaN high electron mobility transistors (HEMTs) with self-upward-polarized AlScN gate dielectrics toward enhancement-mode operation", JJAP, S1102745.R1, 2022

10. Ryota Shibukawa, **Sung-Lin Tsai**, Takuya Hoshii, Hitoshi Wakabayashi, Kazuo Tsutsui, and Kuniyuki Kakushima, “Influence of sputtering power on the switching and reliability of ferroelectric $Al_{0.7}Sc_{0.3}N$ films”, Jpn. J. Appl. Phys. 61 SH1003, 2022

List of Conferences

1. **Sung-Lin Tsai**, Kazuki Kusafuka, Takuya Hoshii, Hitoshi Wakabayashi, Kazuo Tsutsui, Kuniyuki Kakushima, “スパッタリングを用いた AlScN 膜の形成”, 2019 年第 80 回応用物理学会秋季学術講演会, 北海道大学札幌キャンパス, 20p-E303-4, Sep. 18-21, 2019
2. **Sung-Lin Tsai**, Kazuki Kusafuka, Takuya Hoshii, Hitoshi Wakabayashi, Kazuo Tsutsui, Kuniyuki Kakushima, “Polarization Measurement of Sputter-Deposited AlScN Ferroelectric Capacitors”, 「電子デバイス界面テクノロジー研究会 —材料・プロセス・デバイス特性の物理—」(第 25 回研究会), 東レ総合研修センター, Jan. 31-Feb. 1, 2020 (Poster)
3. **Sung-Lin Tsai**, Kazuki Kusafuka, Takuya Hoshii, Hitoshi Wakabayashi, Kazuo Tsutsui, Kuniyuki Kakushima, “Electrical Characterization of Sputter Deposited $\text{Al}_x\text{Sc}_{1-x}\text{N}$ Thin Films”, 237th ECS Meeting, Montréal, Canada, May 10-14, 2020
4. **Sung-Lin Tsai**, T. Hoshii, H. Wakabayashi, K. Tsutsui, K. Kakushima, “Thickness Scaling on Ferroelectric $\text{Al}_{0.8}\text{Sc}_{0.2}\text{N}$ Films”, International Conference on Solid State Devices and Materials, Sep. 27-30, 2020
5. **Sung-Lin Tsai**, Takuya Hoshii, Hitoshi Wakabayashi, Kazuo Tsutsui, Kuniyuki Kakushima, “Highly Oriented Growth of $\text{Al}_x\text{Sc}_{1-x}\text{N}$ Ferroelectric Film on W Bottom Electrodes”, PRiME 2020, Honolulu, HI, Oct. 4-9, 2020
6. **Sung-Lin Tsai**, Takuya Hoshii, Hitoshi Wakabayashi, Kazuo Tsutsui, Tien-Kan Chung, Edward Yi Chang, Kuniyuki Kakushima, “Breakdown mechanism of

ferroelectric $\text{Al}_{0.78}\text{Sc}_{0.22}\text{N}$ films: A continuous reduction in Schottky barrier height upon switching cycles,” Int. Conf. on Advanced Metallization Conference, Oct. 14-15, 2021

7. **Sung-Lin Tsai**, Takuya Hoshii, Hitoshi Wakabayashi, Kazuo Tsutsui, Kuniyuki Kakushima, “A Gradual Change in $\text{Al}_x\text{Sc}_{1-x}\text{N}$ Ferroelectric Film upon Switching Reversal”, 242nd ECS Meeting, Vancouver, BC, Canada, May 29- June 2, 2022

8. [Invited speech] **Sung-Lin Tsai**, Takuya Hoshii, Hitoshi Wakabayashi, Kazuo Tsutsui, Tien-Kan Chung, Edward Yi Chang, Kuniyuki Kakushima, “Ferroelectric properties of room-temperature sputter-deposited AlScN films”, The 69th JSAP Spring Meeting 2022, 23p-E307-4, Mar. 23, 2022

List of Award

第 13 回 シリコンテクノロジー分科会研究奨励賞

論文名 : Room-temperature deposition of a poling-free ferroelectric
AlScN film by reactive sputtering

雑誌名 : Appl. Phys. Lett. 118, 082902 (2021/02)

著者名 : Sung-Lin Tsai, Takuya Hoshii, Hitoshi Wakabayashi, Kazuo
Tsutsui, Tien-Kan Chung, Edward Y. Chang, and Kuniyuki Kakushima

Acknowledgements

I express my deep sense of gratitude to my supervisor Assoc. Prof. Kuniyuki Kakushima who gave me the golden opportunity to do this wonderful research on the topic of AIscN, which also helped me in doing a lot of research, and I came to know about so many new things. I am thankful to him.

I would like to express my special thanks to my Taiwanese supervisors Chung Tien-Kan and Chang Edward Yi who gave me the golden opportunity to participate in the dual degree between Tokyo Institute of Technology and National Chiao Tung University and trained me for learning lots of semiconductor processes. I am thankful to them.

I would also like to thank Katou-san, Assist. Prof Takamasa Kawanago, Assist. Prof Takuya Hoshii, Prof. Tsutsui Kazuo, Prof. Hitoshi Wakabayashi, and Assist. Prof Iriya Muneta for giving me precise advice.

I thank all the labmates in Kakushima/Tsutsui/Wakabayashi labs especially Chen Si-Meng and Li An for the discussions.

I thank all my friends Eric, Nora, Patty, Lien Lo for supporting and encouraging me.

I thank Kawasaki Rotary for its financial support and meaningful events.

Finally, I am extremely grateful to my family for their love, carrying, financial support, and sacrifices in educating and preparing me for my future.